

PL-TR-97-2166

GLOBAL GROUND TOMOGRAPHY

**T. Wallace
D. MacEnany
D. Papadopoulos
R. Singerman**

**Advanced Power Technologies, Inc.
1250 24th Street, NW Suite 850
Washington, DC 20037**

11 December 1997

**Scientific Report No. 1
Approved for public release, distribution unlimited**

**AIR FORCE RESEARCH LABORATORY
Space Vehicles Directorate
29 Randolph Road
AIR FORCE MATERIEL COMMAND
HANSCOM AFB, MA 01731-3010**


PROD 4

19990219031

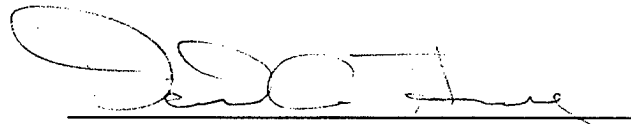
"This technical report has been reviewed and is approved for publication"



JAMES C. BATTIS
Contract Manager



EDWARD J. WEBER, Branch Chief
Ionospheric Hazards Branch



DAVID A. HARDY, Acting Chief
Battlespace Environment Division

This report has been reviewed by the ESC Public Affairs Office (PA) and is releasable to the National Technical Information Service (NTIS)

Qualified requestors may obtain additional copies from the Defense Technical Information Center (DTIC). All others should apply to the National Technical Information Service (NTIS).

If your address has changed, if you wish to be removed from the mailing list, or if the addressee is no longer employed by your organization, please notify AFRL/VSOS-IM, 29 Randolph Road, Hanscom AFB, MA 01731-3010. This will assist us in maintaining a current mailing list.

Do not return copies of this report unless contractual obligations or notices on a specific document require that it be returned.

REPRODUCTION QUALITY NOTICE

This document is the best quality available. The copy furnished to DTIC contained pages that may have the following quality problems:

- **Pages smaller or larger than normal.**
- **Pages with background color or light colored printing.**
- **Pages with small type or poor printing; and or**
- **Pages with continuous tone material or color photographs.**

Due to various output media available these conditions may or may not cause poor legibility in the microfiche or hardcopy output you receive.



If this block is checked, the copy furnished to DTIC contained pages with color printing, that when reproduced in Black and White, may change detail of the original copy.

REPORT DOCUMENTATION PAGEForm Approved
OMB No. 074-0188

Public reporting burden for this collection of information is estimated to average 1 hour per response, including the time for reviewing instructions, searching existing data sources, gathering and maintaining the data needed, and completing and reviewing this collection of information. Send comments regarding this burden estimate or any other aspect of this collection of information, including suggestions for reducing this burden to Washington Headquarters Services, Directorate for Information Operations and Reports, 1215 Jefferson Davis Highway, Suite 1204, Arlington, VA 22202-4302, and to the Office of Management and Budget, Paperwork Reduction Project (0704-0188), Washington, DC 20503

1. AGENCY USE ONLY (Leave blank)**2. REPORT DATE**
11 Dec 1997**3. REPORT TYPE AND DATES COVERED**
Scientific no. 1**4. TITLE AND SUBTITLE**
Global Ground Tomography**5. FUNDING NUMBERS**
F19628-96-C-0145
PE 61102F
PR 4266 TA GH WU AH**6. AUTHOR(S)**
T. Wallace, D. Mac Enany, D. Papadopoulos, R. Singerman**7. PERFORMING ORGANIZATION NAME(S) AND ADDRESS(ES)**Advanced Power Technologies, Inc.
1250 24th St., Suite 850
Washington, DC 20037**8. PERFORMING ORGANIZATION
REPORT NUMBER****9. SPONSORING / MONITORING AGENCY NAME(S) AND ADDRESS(ES)**Air Force Research Laboratory
29 Randolph Road
Hanscom AFB, MA 01731-3010
Contract Manager: James Battis/VSB**10. SPONSORING / MONITORING
AGENCY REPORT NUMBER**
PL-TR-97-2166**11. SUPPLEMENTARY NOTES****12a. DISTRIBUTION / AVAILABILITY STATEMENT**
Approved for public release; distribution unlimited**12b. DISTRIBUTION CODE****13. ABSTRACT (Maximum 200 Words)**

The results of the first year of the Global Ground Tomography program for low frequency electromagnetic imaging and characterization of underground structures are presented.

14. SUBJECT TERMS
magnetotellurics, underground imaging**15. NUMBER OF PAGES****16. PRICE CODE****17. SECURITY CLASSIFICATION
OF REPORT**
unclassified**18. SECURITY CLASSIFICATION
OF THIS PAGE**
unclassified**19. SECURITY CLASSIFICATION
OF ABSTRACT**
unclassified**20. LIMITATION OF ABSTRACT**
SAR

Table of Contents

1. Introduction	1
2. Signal Processing and Imaging.....	3
2.1. Signal Processing	3
2.1.1. Impedance Estimation	3
2.1.2. Power Spectral Estimation	8
2.1.3. Implementation.....	13
2.2. Imaging Algorithms.....	14
2.2.1. Fundamentals of Inverse Imaging	14
2.2.2. Conventional Magnetotelluric Methods and New Approaches.....	16
2.2.3. Spectral Regularization	17
2.2.4. A Physical Interpretation of Spectral Regularization.....	19
2.2.5. Complex Apparent Resistivity	20
2.2.6. Summary of Imaging Method.....	22
3. Electromagnetic Modeling and Inversion.....	24
3.1. Forward Modeling.....	25
3.1.1. Uniform Half-Space	25
3.1.2. Effect of Conducting Surface Layers	36
3.2. Inversion of Modeled Data.....	42
3.2.1. Resolution of RRI Inversions	43
3.2.2. RRI Inversion of Simulated Golden Zone Data	50
3.2.3. Effect of Surface Layers on Tunnel Detection.....	51
4. Experiments.....	55
4.1. Equipment and Measurement Procedures	55
4.1.1. Transmitter	55
4.1.2. Sensors	57
4.1.2.1. Electric Field Sensors.....	58
4.1.2.2. Magnetic Field Sensors	59
4.1.2.3. Analog Front End Amplifier	62
4.1.2.4. Data Recorder.....	63
4.1.2.5. Data Transfer.....	66
4.1.3. Standard Procedures	67
4.1.3.1. Local Source.....	68
4.1.3.2. Ionospheric Source	69
4.1.3.3. Surveying.....	70
4.2. SSC Experiment	70
4.2.1. Description of Experiment	71
4.2.2. Analysis of Results.....	73
4.3. Golden Zone Experiment	75
4.3.2. Analysis of Results.....	83
4.3.3. Final Resistivity Image.....	106
4.3.4. Depth Estimation.....	109
5. Conclusions and Future Plans	111

1. Introduction

This report documents the progress during the first year of the Global Ground Tomography (GGT) contract, a research effort in imaging of underground structures using low frequency electromagnetic (EM) signals. This effort employs theoretical analysis, simulation, and experiments to assess the performance of low frequency EM imaging and develop an understanding of the basic physical relationships that would affect the design of an operational imaging system. This report provides a detailed description of the work performed to date in each of the three major areas included in the contract: signal processing and imaging, electromagnetic simulation, and experiments.

In the signal processing area, the major results to date have been the development and implementation of software for computing impedance estimates from experimental data; this software has been used for processing all of the data acquired under this contract. Work in the imaging area has concentrated on applying APTI's proprietary imaging techniques to both simulated and actual data, and comparing the results to those obtained using conventional imaging algorithms. A detailed discussion of the differences between APTI's method and conventional approaches is given in Section 2.2. Only preliminary results of the comparisons are available, and some of these are shown in Section 3.2; more detailed direct comparisons using both simulated and actual data are underway.

Electromagnetic simulations of targets similar to those employed in the first two field experiments have been computed and analyzed. These two-dimensional simulations model empty (resistive) tunnels in one- or two-layer grounds. Even for this simplified case, several important effects have been observed, these are discussed in Section 3. The results of employing a widely used imaging algorithm to simulated data are also discussed in this section. Future efforts will include modeling of conductive two-dimensional targets and initial examinations of realistic three-dimensional targets such as buried facilities and bunkers.

Progress in the experimental area included the design and integration of a data acquisition system described in Section 4.1, and the use of this system to conduct two field experiments. The first experiment employed a local VLF source, and was conducted at the Superconducting Supercollider site near Waxahatchee, Texas; the second used both a local transmitter and the HAARP ionospheric heater as sources, and was carried out at a mine near Cantwell, Alaska. The results of these experiments are presented and discussed in Section 4.2. Although not all of the data has yet been analyzed, a successful result has been obtained in the Alaskan experiment, locating a mine tunnel at a depth of 29 meters.

The final section summarizes the results and outlines plans for the next year of this effort. Major goals include elimination of the backlog of unprocessed experimental data, improvements in the speed of data processing and imaging, more extensive use of simulations in detailed studies of imaging performance, and execution and analysis of additional field experiments on a wider variety of targets.

2. Signal Processing and Imaging

In the following section, an outline of the signal processing and imaging techniques applied to convert measured data into images of underground conductivity variations is given. This process begins with the processing of the measured data into impedance estimates, and then converts the impedance estimates from several locations into an image of the underground conductivity.

2.1. Signal Processing

The first step in processing measured data is to convert the time series for the electric and magnetic fields measured at a given location into an estimate of the surface impedance at that location. This process is described in the sections below.

2.1.1. Impedance Estimation

From measurements of electric and magnetic fields at a given location, we would like to determine the surface impedance as a function of frequency at that location. The basic equation that defines the surface impedance matrix in terms of the electric and magnetic fields is

$$\begin{bmatrix} E_x(\omega) \\ E_y(\omega) \end{bmatrix} = \begin{bmatrix} Z_{xx}(\omega) & Z_{xy}(\omega) \\ Z_{yx}(\omega) & Z_{yy}(\omega) \end{bmatrix} \begin{bmatrix} H_x(\omega) \\ H_y(\omega) \end{bmatrix}.$$

All of the entries in this matrix equation are functions of frequency, so all of the operations we will describe below must be performed for each frequency of interest. Often, we will drop the explicit dependence on frequency to make the equations more compact.

The matrix equation that defines the impedances is a system of two equations in four unknowns that cannot be solved directly. It is possible to produce a system of four equations in four unknowns by multiplying both sides of the equation on the right by a two-element row vector, and then computing the expected value of the result (an operation indicated by angle brackets). We will assume that the statistical expected value is the same as the value obtained by averaging the quantities over an infinitely long data

record. Our initial analysis will then indicate the results that would be obtained with extremely large amounts of measured data.

If we choose the elements of the row vector to be the complex conjugates of the field values H_x and H_y , for example, we obtain the equation

$$\left\langle \begin{bmatrix} E_x(\omega) \\ E_y(\omega) \end{bmatrix} \begin{bmatrix} H_x^*(\omega) & H_y^*(\omega) \end{bmatrix} \right\rangle = \begin{bmatrix} Z_{xx}(\omega) & Z_{xy}(\omega) \\ Z_{yx}(\omega) & Z_{yy}(\omega) \end{bmatrix} \left\langle \begin{bmatrix} H_x(\omega) \\ H_y(\omega) \end{bmatrix} \begin{bmatrix} H_x^*(\omega) & H_y^*(\omega) \end{bmatrix} \right\rangle.$$

Choosing to make the elements of the row vector complex conjugates of some quantity makes the elements of the resulting matrices auto- or cross-power spectral densities, so that the elements themselves may be easily interpreted. For example, the equation above reduces to

$$\begin{bmatrix} S_{ExHx}(\omega) & S_{ExHy}(\omega) \\ S_{EyHx}(\omega) & S_{EyHy}(\omega) \end{bmatrix} = \begin{bmatrix} Z_{xx}(\omega) & Z_{xy}(\omega) \\ Z_{yx}(\omega) & Z_{yy}(\omega) \end{bmatrix} \begin{bmatrix} S_{HxHx}(\omega) & S_{HxHy}(\omega) \\ S_{HyHx}(\omega) & S_{HyHy}(\omega) \end{bmatrix},$$

where all the elements to be computed from the measured data are power spectral densities.

For the resulting equation to be nontrivial (i.e. not just the matrix equation $\mathbf{0} = \mathbf{0}$), the elements of the row vector should be correlated statistically with the field measurements. This requirement is clearly satisfied by conjugates of the measurements themselves, or of any similar measurement of electric or magnetic fields at nearby locations. The two most common choices are to employ $\begin{bmatrix} H_x^* & H_y^* \end{bmatrix}$, as in the example above, or to use two remote reference signals $\begin{bmatrix} R_a^* & R_b^* \end{bmatrix}$, as components of the row vector. The first approach is called the standard method, and the second, the remote reference method.

Although both of these approaches produce similar results in the absence of noise, when noise is present, the remote reference technique has significant advantages. To see why, let us examine the case where all of the field measurements have measurement noise added to them, for example, the internal noise of the field sensors. This changes the standard method equation above to

$$\left\langle \begin{bmatrix} E_x + N_{Ex} \\ E_y + N_{Ey} \end{bmatrix} \begin{bmatrix} H_x^* + N_{Hx}^* & H_y^* + N_{Hy}^* \end{bmatrix} \right\rangle = \begin{bmatrix} Z_{xx} & Z_{xy} \\ Z_{yx} & Z_{yy} \end{bmatrix} \left\langle \begin{bmatrix} H_x + N_{Hx} \\ H_y + N_{Hy} \end{bmatrix} \begin{bmatrix} H_x^* + N_{Hx}^* & H_y^* + N_{Hy}^* \end{bmatrix} \right\rangle.$$

If we assume that the noise in each measurement is statistically uncorrelated with the noise in all the other measurements, the standard method results in the equation

$$\begin{bmatrix} S_{ExHx} & S_{ExHy} \\ S_{EyHx} & S_{EyHy} \end{bmatrix} = \begin{bmatrix} Z_{xx} & Z_{xy} \\ Z_{yx} & Z_{yy} \end{bmatrix} \begin{bmatrix} S_{HxHx} + W_{HxHx} & S_{HxHy} \\ S_{HyHx} & S_{HyHy} + W_{HyHy} \end{bmatrix},$$

where W_{HxHx} and W_{HyHy} are the power spectral densities of the measurement noise added to H_x and H_y . This is clearly a different equation than the noise-free version, and its solution will be different. To see how the addition of noise affects the solution, let us examine the changes in one component, Z_{xy} . The noise-free equation has the solution

$$Z_{xy} = \frac{S_{ExHy}S_{HxHx} - S_{ExEx}S_{HxHy}}{S_{HxHx}S_{HyHy} - S_{HxHy}S_{HyHx}},$$

while the noisy equation has the different solution

$$\tilde{Z}_{xy} = \frac{S_{ExHy}(S_{HxHx} + W_{HxHx}) - S_{ExEx}S_{HxHy}}{S_{HyHy}(S_{HxHx} + W_{HxHx}) - S_{HxHy}S_{HyHx} + S_{HxHx}W_{HyHy} + W_{HxHx}W_{HyHy}}.$$

To simplify these two equations, assume that the measurements are taken over a one dimensional vertically stratified region with no horizontal variation. This causes several of the crosspower spectral densities to become zero, and the noise-free equation becomes

$$Z_{xy} = \frac{S_{ExHy}}{S_{HyHy}},$$

while the noisy equation in this case is

$$\tilde{Z}_{xy} = \frac{S_{ExHy}}{S_{HyHy} + (S_{HxHx}W_{HyHy} + W_{HxHx}W_{HyHy})/(S_{HxHx} + W_{HxHx})}.$$

We can see that the magnitude of the denominator of the noisy equation is the same or larger, because all of the extra terms are autopower spectral densities, which must be

nonnegative. The magnitude of the answer will therefore be the same or smaller. The results of this particular case also hold in general: the use of the standard method when measurement noise is not negligible results in impedance estimates whose magnitudes are lower than their true values. Note that this is true even in the limit of infinitely long measurement times; this type of error cannot be averaged out.

In contrast, if we use the remote reference method, the equation to be solved is

$$\left\langle \begin{bmatrix} E_x(\omega) \\ E_y(\omega) \end{bmatrix} \begin{bmatrix} R_a^*(\omega) & R_b^*(\omega) \end{bmatrix} \right\rangle = \begin{bmatrix} Z_{xx}(\omega) & Z_{xy}(\omega) \\ Z_{yx}(\omega) & Z_{yy}(\omega) \end{bmatrix} \left\langle \begin{bmatrix} H_x(\omega) \\ H_y(\omega) \end{bmatrix} \begin{bmatrix} R_a^*(\omega) & R_b^*(\omega) \end{bmatrix} \right\rangle,$$

which reduces in the noise-free case to

$$\begin{bmatrix} S_{ExRa}(\omega) & S_{ExRb}(\omega) \\ S_{EyRa}(\omega) & S_{EyRb}(\omega) \end{bmatrix} = \begin{bmatrix} Z_{xx}(\omega) & Z_{xy}(\omega) \\ Z_{yx}(\omega) & Z_{yy}(\omega) \end{bmatrix} \begin{bmatrix} S_{HxRa}(\omega) & S_{HxRb}(\omega) \\ S_{HyRa}(\omega) & S_{HyRb}(\omega) \end{bmatrix}.$$

When noise is added to the measurements, the equation becomes

$$\left\langle \begin{bmatrix} E_x + N_{Ex} \\ E_y + N_{Ey} \end{bmatrix} \begin{bmatrix} R_a^* + N_{Ra}^* & R_b^* + N_{Rb}^* \end{bmatrix} \right\rangle = \begin{bmatrix} Z_{xx} & Z_{xy} \\ Z_{yx} & Z_{yy} \end{bmatrix} \left\langle \begin{bmatrix} H_x + N_{Hx} \\ H_y + N_{Hy} \end{bmatrix} \begin{bmatrix} R_a^* + N_{Ra}^* & R_b^* + N_{Rb}^* \end{bmatrix} \right\rangle,$$

which reduces to the same equation as the noise free case:

$$\begin{bmatrix} S_{ExRa} & S_{ExRb} \\ S_{EyRa} & S_{EyRb} \end{bmatrix} = \begin{bmatrix} Z_{xx} & Z_{xy} \\ Z_{yx} & Z_{yy} \end{bmatrix} \begin{bmatrix} S_{HxRa} & S_{HxRb} \\ S_{HyRa} & S_{HyRb} \end{bmatrix}.$$

The perturbing terms are absent because the noise in each of the remote reference channels R_a and R_b is independent of the noise in H_x and H_y . Thus, even in the case where noise is present, we can obtain accurate estimates of the surface impedances by using the remote reference method, as long as our measurement times are sufficiently long.

The remote reference method would eliminate the bias due to measurement noise even if the sensors providing the remote reference signal were placed at the same location as the E and H sensors. Placing the remote reference sensors at a distance from the other sensors brings an additional advantage by allowing the technique to remove bias due to sources

other than the internal noise of the sensor, such as local electromagnetic interference or vibration-induced signals in magnetic field sensors. As long as the remote reference is placed so that any signal present at both the reference location and the measurement location must be an electromagnetic wave propagating in the Earth-ionosphere waveguide, the results obtained with this technique will not be biased by noise, and in the limit of infinitely long measurement time, will equal the true values of the surface impedances.

In practice, of course, measurement times are not infinitely long. In this case, both the standard and the remote reference techniques will produce estimates of the surface impedances that are different from the true values. As we saw above, the standard method results will tend to be smaller in magnitude than the true values, while the remote reference method results will vary both above and below the true value. The amount of variation from the true value at any given frequency depends on the intensity of the electromagnetic signal at that frequency compared to the noise. As an example, Figure 1 shows the magnitude of the impedance computed from a short data record. The top curve is the remote reference result; the bottom, the standard result.

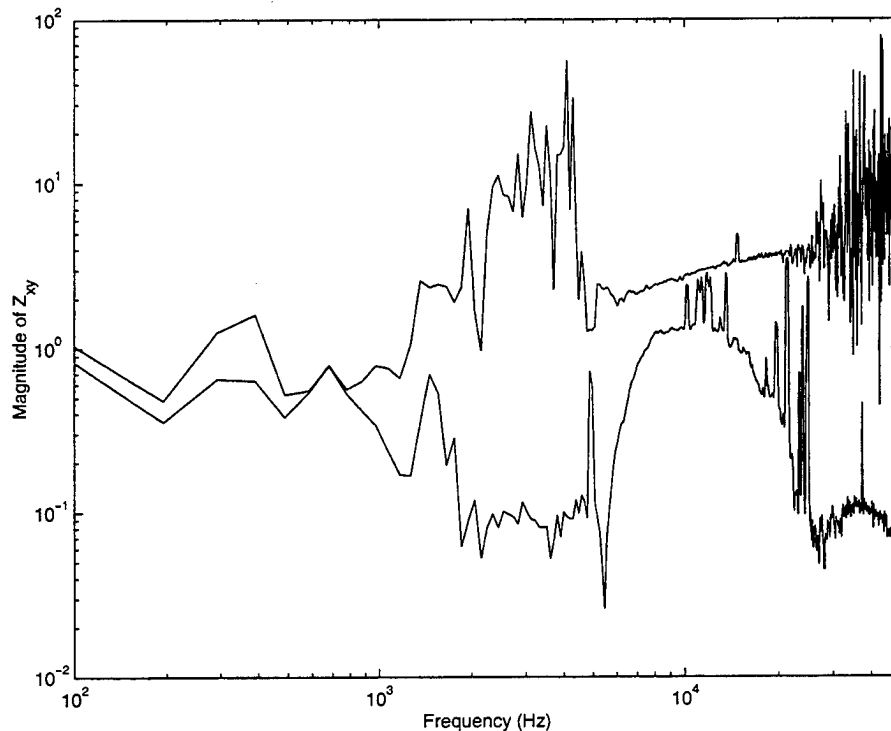


Figure 1. Standard and Remote Reference Impedance Estimates

It is important to understand that, for the purposes of finding the impedance, the “signal” includes all electromagnetic radiation from distant sources, whether they are controlled sources or natural random sources like lightning. Any signal from a distant source, random or controlled, satisfies the assumptions necessary for the impedance to be meaningful. “Noise” means anything that is not a propagating EM wave from a distant source, and so does not satisfy the assumptions needed for the impedance to be meaningful, like the internal noise of the sensors, local electromagnetic interference, or noise due to vibration of magnetic sensors.

In Figure 1, the remote reference and standard method impedances are different from each other in the region between 2 kHz and 5 kHz where little natural background signal is present; above and below this band, the two impedances are closer together because of the presence of signals caused by distant thunderstorm activity. The large difference between the two impedance estimates above in the 30 - 50 kHz region is due to the effects of internal noise in the magnetic field sensors.

2.1.2. Power Spectral Estimation

One of the reasons for formulating the impedance equations as we have above, so that the entries computed from the measured data are auto- or crosspower spectral densities, is to take advantage of the large body of previous work on accurate estimation of spectral densities. The two major categories of power spectral estimation techniques are the classical methods based on the Fourier transform, and the parametric methods, which assume that the signal can be modeled as a particular type of random process, and estimate the model coefficients in order to determine the spectral estimate. The classical methods are the oldest and most widely used, and although parametric techniques have demonstrated advantages in other applications, they have not been widely applied in processing of magnetotelluric data. At present, classical methods are used for the processing of all field data, but an examination of the possible benefits of parametric methods is planned during the next year.

Because classical spectral estimation techniques have been in wide use for more than thirty years, their proper use is very well understood; in fact, a good classical spectral estimate can be computed in almost the manner implied by the equations given in the previous section. As we can see, each entry in the final matrix equation is the product of the Fourier transform of a signal with the conjugate of the Fourier transform of either the

same signal (an autopower spectral density), or a different signal (a crosspower spectral density). If we were to simply take the Fourier transform of the entire input data record, compute its conjugate, and multiply them together, however, we would have a poor spectral estimate for two important reasons: leakage and variability.

Leakage refers to the spreading of the energy from a sharp spectral feature, such as a sinusoidal signal, into adjacent frequencies, where it may obscure other details of the spectrum. This is caused by the fact that a finite data record is in effect the product of multiplying an infinite data record with a rectangular "window" function that is one during the observation time, and zero elsewhere. In the Fourier domain, multiplication of the data by a window is equivalent to the convolution of the Fourier transform of the data with the Fourier transform of the window, and so if the window has a Fourier transform that is spread out across a range of frequencies, any sharp spectral features in the data will also be spread out. A rectangular window is just the result of doing nothing to the input data, but there are many other windows with Fourier transforms that are more compact in the frequency domain and cause much less spreading in the computed spectra. All that is necessary to dramatically reduce leakage is to choose an appropriate window function and multiply the data record by that window before computing the Fourier transform.

To illustrate the importance of windowing to reduce leakage, Figure 2 below compares an estimate computed using a rectangular window with one computed using a low-leakage Hann window, on an actual data record taken with a local source operating at 5 kHz. The figure shows the field spectral density, which is the square root of the power spectral density, as is more common in geophysics. Notice that when the rectangular window is used, the strong 5 kHz signal is spread over a very large range, completely obscuring other spectral features. The Hann window has dramatically lower leakage, providing an accurate estimate of spectral features near the powerful 5 kHz signal.

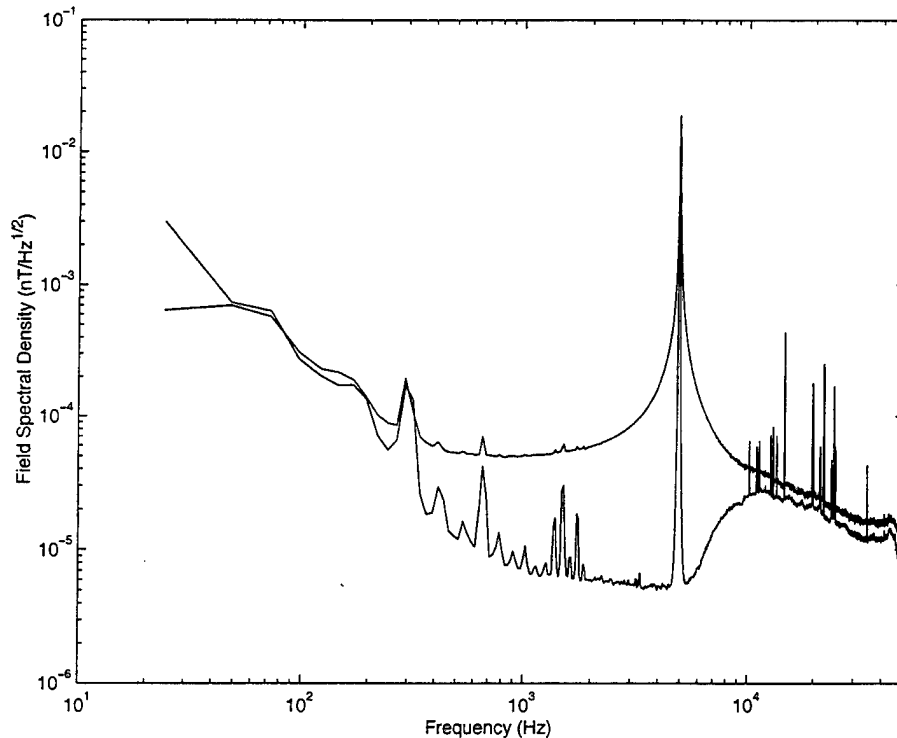


Figure 2. Proper Choice of Window is Essential when
Sharp Spectral Features are Present

The second problem that must be addressed in classical spectral estimation is the variability of the estimate. If we compute the windowed Fourier transform of the entire input data record, we will have a spectral estimate with very high resolution, but also very high variability. The standard deviation of a spectral estimate computed in this way is approximately equal to the true spectral density, so the variability of the estimate is very large. To reduce this variability, we can divide the input data record into shorter segments, window, and compute spectral estimates from each segment, then average the segment estimates together to form the overall spectral estimate. This will reduce the variability at the cost of decreasing resolution. In fact, we can trade off variability and resolution by increasing or decreasing the number of segments.

The combination of windowing and segment averaging produces a classical spectral estimation method with excellent performance. In fact, the procedure we have described above is a very widely used method first developed by Welch. Welch also found that using segments that overlap can further reduce the variability of the spectral estimate; in computation of estimates on our experimental data, we have employed a Hann window to

minimize leakage, and overlapped the data segments by 50% to minimize the variability of the estimate.

As we have seen, the major tradeoff in the computation of power spectral estimates using classical techniques is between the resolution of the spectral estimate and its accuracy. From a given amount of input data, it is possible to compute spectral estimates with higher resolution and higher variability, or lower resolution and lower variability. To illustrate this tradeoff, we have computed power spectral estimates of varying resolutions from the same ten-second data record taken with a local source operating at 5 kHz.

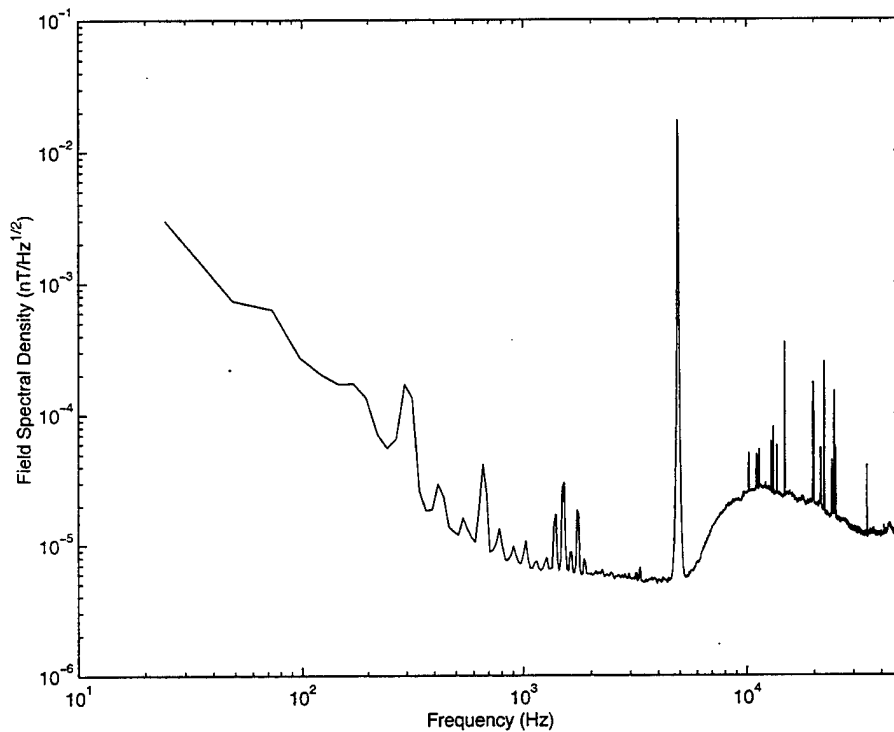


Figure 3. Spectral Estimate for 4096 Point FFT Length

The first estimate, shown in Figure 3, uses a FFT length of 4096 points, resulting in an approximate frequency resolution (spectral bin width) of 24.4 Hz. Although most of the spectral features above 1 kHz are visible in the spectrum, the resolution is too low to show details below a few hundred Hertz. In addition, the strong peak at 5 kHz still shows a small amount of leakage at its base, despite the use of a low leakage window. However, the continuous portions of the spectrum, where no sine waves are present, show very little variability; for example, the shoulder from 6 kHz to 10 kHz is very smooth. This

spectrum is the average of slightly more than 500 overlapping spectra, reducing the variability of the estimated field spectrum to a very low level.

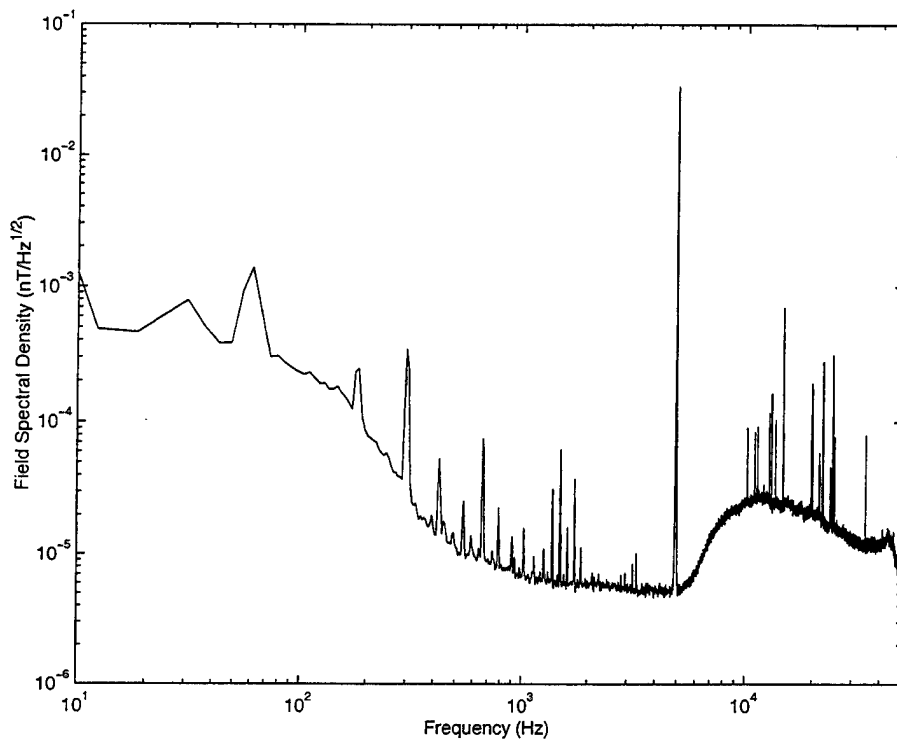


Figure 4. Spectral Estimate for 16384 Point FFT Length

The second estimate (Figure 4) uses a FFT length of 16384, for a frequency resolution of 6.1 Hz. At this higher resolution, spectral detail is now visible down to a few hundred Hertz, and all of the sinusoidal peaks in the spectrum are much better defined. Note that as the resolution increases, the leakage tails around strong signals like the 5 kHz transmitter signal become narrower, and the peaks themselves increase in height. This allows the detection of smaller peaks like the cluster visible at 3 kHz. However, note that the variability of the spectrum has also increased; the shoulder region at 6 - 10 kHz now shows noticeable roughness, even though the true spectrum is smooth in this region. This estimate is the average of approximately 130 overlapped spectra. Each increase by a factor of four in the FFT length reduces the number of spectra averaged by a factor of four, and increases the variance of the field spectral density estimates shown by a factor of 2.

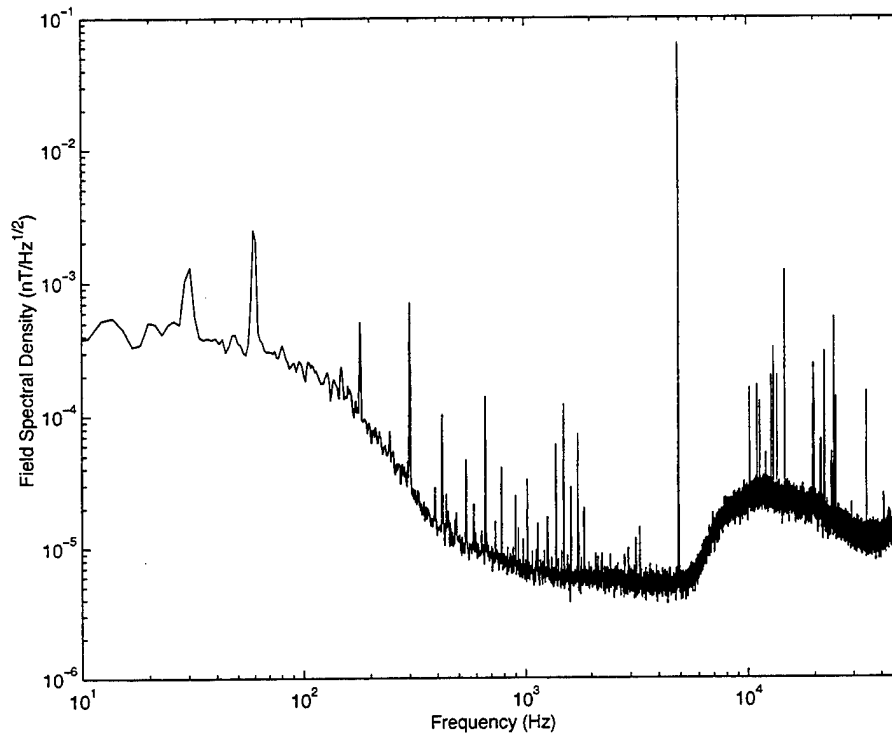


Figure 5. Spectral Estimate for 65536 Point FFT Length

The final example (Figure 5) uses a FFT length of 65536 points, for a frequency resolution of 1.5 Hz. Spectral features are now visible below 100 Hz, and the sinusoidal peaks have continued to increase in height. However, this spectrum is the average of only 31 overlapped spectra, and the variability is becoming quite large.

We have seen that classical power spectral estimation using a fixed amount of input data involves a tradeoff between resolution and variability. In processing the field data for this program, data records from 10 seconds to 100 seconds in length have been employed. Typical FFT lengths have been from 4096 to 16384 points, resulting in power spectral estimates similar to those in Figures 3 and 4. Although these parameters have yielded good results, the interaction between spectral estimate resolution and variability and the performance of the imaging algorithm has not yet been fully explored. A detailed study of these interactions will be conducted during the next year.

2.1.3. Implementation

The spectral estimation algorithms described above have been implemented in a processing program for analysis of field data. The program, written in C, performs power

spectral estimation using the Welch method, applies instrument calibrations, and produces auto- and crosspower spectral estimates. In addition, the program computes the standard error (normalized standard deviation) of each of the autopower spectral estimates, to provide an objective measure of the quality of each spectral estimate. All computations are made in 32-bit floating point to ensure accuracy, and using optimized assembly implementations of the fast Fourier transform specialized for real input data to maximize speed.

2.2. Imaging Algorithms

After the spectral estimates have been computed, and a surface impedance calculated from these spectral estimates, the data are used to produce an image showing the estimated subsurface conductivity as a function of depth. In contrast to the spectral estimation problem, which is very stable, the inverse imaging problem is unstable, and a variety of methods have been employed in the past to achieve stability while still maximizing resolution.

In the following section, a new approach developed by APTI, called spectral regularization, is described and compared with conventional magnetotelluric inversion algorithms. Although the algorithm was not developed under this contract, a basic understanding of its operation and its differences from conventional magnetotelluric inversion algorithms is important for understanding the analysis of experimental data given in Section 4.

2.2.1. Fundamentals of Inverse Imaging

One often has a set of observed data e arrived at as the result of an experiment, that one is attempting to fit with some function f . This fit is defined so as to minimize an associated cost $C[f]$, while also ensuring that a *distortion* function $D[e, f]$, measuring the difference between the observed data and the function f does not exceed some maximum value. In mathematical notation we have

$$\min_{f \in F} C[f] \quad \text{subject to} \quad D[e, f] \leq \bar{D}, \quad \bar{D} > 0 \quad (I)$$

where $f \in F$ defines the class of admissible solutions. It is important to appreciate that problem (I) has a dual that can be written as

$$\min_{f \in F} D[e, f] \quad \text{subject to} \quad C[f] \leq \bar{C}, \quad \bar{C} < \infty, \quad (\text{II})$$

in other words, minimize the distortion while keeping the cost from exceeding a given value. In both cases, critical choices must be made in the specification of F , $C[f]$, and $D[e, f]$. Some choices result in a problem that has no solution; in other cases the solution may not be unique, stable, or computationally feasible to determine.

Analytically, the use of Lagrange multipliers provides us with some basic insight into the connections between (I) and (II). For any $\lambda > 0$, the optimum solution, f_λ^* , for the unconstrained problem defined by the Lagrange objective

$$J_\lambda[f|e] = D[e, f] + \lambda C[f],$$

written in the usual way as

$$f_\lambda^* = \arg \min_{f \in F} J_\lambda[f|e],$$

is also optimal for the constrained problem

$$f_\lambda^* = \arg \min_{f \in F} C[f] \quad \text{subject to} \quad D[e, f] \leq D[e, f_\lambda^*].$$

Hence, $\lambda > 0$ indexes a family of achievable solutions with the property that if $D[e, f_\lambda^*]$ equals \bar{D} , then f_λ^* is an optimal solution to (I). Emphasizing duality, f_λ^* is also optimal for the constrained problem defined according to

$$f_\lambda^* = \arg \min_{f \in F} D[e, f] \quad \text{subject to} \quad C[f] \leq C[f_\lambda^*],$$

and if $C[f_\lambda^*]$ equals \bar{C} , then f_λ^* is an optimum for (II).

In general, there exists a set of pairs, $(C[f_\lambda^*], D[e, f_\lambda^*])$, indexed by λ , that minimize the unconstrained Lagrangian and occupy the space $\mathbf{C} \times \mathbf{D}$, upon which all the extremals are defined.

2.2.2. Conventional Magnetotelluric Methods and New Approaches

The recent literature on MT inversion focuses on a type (I) constrained optimization, defining $D[e, f]$ as a squared error and modeling this error as Gaussian so that χ^2 random variables result. The constraint is expressed as a hard constraint of the form

$$D[e, f] = \bar{D},$$

and the Lagrangian formulation is used sequentially to estimate a limiting operating point, λ^* , that satisfies this constraint while delivering a minimum cost $C[f_\lambda^*]$. In these formulations, the fit is defined as a mapping from spatial coordinates to conductivity values so that $D[e, f_\lambda^*]$ is of the form $D[e, f(\sigma_\lambda^*)]$ where $\sigma_\lambda^* \geq 0$ is the desired conductivity estimate. This reflects the fact that the computation of the distortion entails the forward (numerical) solution of Maxwell's equations. In addition, these inversion methods choose $C[f]$ as a measure of variability or roughness, which is motivated in general by Tikhonov theory as a way to deal with the instability of the inverse problem.

With reference to the preceding discussion, our current approach differs from most MT methods in two key ways. First, we use a type (II) formulation and place the constraint on the cost $C[f]$ while the distortion $D[e, f]$ is minimized. In this way, each potential fit is subjected to the same total cost, while the optimal fit is the one that minimizes the total distortion. Of course, the mathematics are dual and one can pose the optimization in either way, but the physical aspects of the problem suggest that option (II) has some advantages. Second, we divide the problem into two nested optimizations, in which the first obtains an estimate of the resistivity at each surface point as a function of frequency, using the measured field data, and the second addresses the spatial inversion aspect. So, in fact, we employ two type (II) optimizations in order to obtain the final result. Having made this separation, we may then define a cost for the first optimization that follows directly from physical considerations. This is in contrast to the costs used in many MT algorithms that are largely chosen without regard to the physics of the problem.

2.2.3. Spectral Regularization

To be specific, the method employed here differs from earlier methods in that fundamental physical constraints, namely the Kramers-Krönig relations that arise in dispersive wave theory, dictate the form of the $C[f]$ used in the first optimization. This approach is unique in that it employs a filtering of the raw data, referred to as *spectral regularization*, before any inversion is performed. This type of pre-inversion filtering yields estimates that can then be either jointly processed or post-processed using conventional MT inversion techniques to achieve resistivity imaging with higher resolution. Our approach also differs in two other key aspects, but these aspects are better discussed after the basic principles have been explained.

The general form of the optimization employed is most easily expressed in a two-step format. The first step of the optimization involves minimizing, for a given coherence threshold κ , and spectral regularization parameter λ_v , a vertical sounding objective $J_v[\kappa, \lambda_v](\rho_c)$ with respect to ρ_c , where J_v is given as

$$1) \quad J_v[\kappa, \lambda_v | \tilde{\rho}_c](\rho_c) = \int \bar{C}_\kappa(f) \left| \log \frac{\rho_c(f)}{\tilde{\rho}_c(f)} \right|^2 df + \lambda_v \int \left| \frac{d \log \rho_c(f)}{d \log f} \right|^2 df.$$

Here, the input $\tilde{\rho}_c$ is the complex resistivity defined as

$$\tilde{\rho}_c(f; x) = \frac{\tilde{Z}^2(f; x)}{j2\pi f \mu_0},$$

where $\tilde{Z}(f; x)$ is an estimate of the surface impedance $Z(f; x)$ computed from the measured data at each frequency f and position x . Finally, $\bar{C}_\kappa(f; x)$ is the thresholded coherence matrix defined as

$$\bar{C}_\kappa(f; x) = 1 \{ C(f; x) > \kappa \} \quad 0 \leq \kappa \leq 1,$$

where κ is the threshold and $C(f; x)$ is the estimated coherence. The coherence at any given frequency between the measured electric and magnetic field associated with a particular mode is a measure of how consistent the actual measured data are with the underlying assumption of plane wave excitation. Accepting only data with a coherence

above a certain threshold is a simple but effective means of preventing input data severely corrupted by noise from affecting the final solution.

If we define the solution to the first (vertical) optimization as

$$\rho_c^v = \arg \min_{\rho_c} \mathbf{J}_v[\kappa, \lambda_v](\rho_c),$$

then we may define the second (horizontal) optimization objective as

$$2) \quad \mathbf{J}_h[\lambda_h | \rho_c^v](\rho_c) = \int \left| \rho_c(x) - \rho_c^v(x) \right|^2 dx + \lambda_h \int \left| \frac{d\rho_c(x)}{f dx} \right|^2 dx.$$

We have employed the shorthand notations $\rho_c(f)$ and $\rho_c^v(x)$ for $\rho_c(f; x)$ and $\rho_c^v(x; f)$, respectively, to keep the notation simple. If we define the nested objective

$$\mathbf{J}[\kappa, \lambda_v, \lambda_h] \equiv \mathbf{J}_h \left[\lambda_h \left| \arg \min_{\rho_c} \mathbf{J}_v[\kappa, \lambda_v | \tilde{\rho}_c](\rho_c) \right| \right],$$

then the overall optimal solution may be concisely expressed as

$$\rho_c^* = \arg \min_{\rho_c} \mathbf{J}[\kappa, \lambda_v, \lambda_h](\rho_c).$$

We first note that the \mathbf{J}_v (vertical) spectral regularization objective is central to the high performance of this technique. This first optimization process may either be considered as data filtering in preparation for the inversion step, or included in the inversion objective itself.

Here, we may point out the two additional aspects of this approach mentioned above that appear to also differ from current MT algorithms. Referring to \mathbf{J}_v , we see that this objective, both its familiar Hilbert space L^2 error integral and its Sobolev smoothing integral, are defined in terms of the logarithm of the complex resistivity. To simplify further discussion and notation, we will define $\Lambda = \log \rho_c$ which allows us to write the spectral regularization objective in the compact form

$$\mathbf{J}_v[\kappa, \lambda|\tilde{\Lambda}](\Lambda) = \int \bar{C}_\kappa |\Lambda - \tilde{\Lambda}|^2 df + \lambda \int |f \Lambda'|^2 df.$$

Secondly, we note that we have continued to employ the coherence mask \bar{C}_κ in the objective definition even in cases where the input data, $\tilde{\Lambda}$, have been derived using the remote reference technique. We next must turn the discussion to how the spectral regularization objective \mathbf{J}_v derives its form from basic physical principles.

2.2.4. A Physical Interpretation of Spectral Regularization

Consider the estimation of a one-dimensional ground conductivity $\sigma(z)$ ¹ over some range of depth, z , given the impedance $Z_0(f) = E_0(f)/H_0(f)$ measured on the ground surface over some range of frequency. The mapping M_f that takes $\sigma(\cdot)$ into $Z_0(f)$ is strongly smoothing. For example, $Z_0(\cdot)$ is a smooth function of frequency even when $\sigma(\cdot)$ consists of discrete layers of markedly different conductivities. Hence, M_f can be described as a low pass operator, since rapid changes in $\sigma(\cdot)$, those with substantial high spatial frequency content, are smoothed out. This suggests that the inverse operator M_z^{-1} $z \geq 0$, must have the kind of high pass character to produce a $\sigma(\cdot)$ that changes significantly with depth from a relatively smooth $Z_0(\cdot)$. Practically speaking, M_z^{-1} is not a stable inverse in the sense that small changes in $Z_0(\cdot)$ must invert to large changes in $\sigma(\cdot)$. Unfortunately, when $Z_0(\cdot)$ is computed from measured data for E_0 and H_0 , the measured value of $Z_0(\cdot)$ has errors due to noise in the measured fields. As a result, any noise reduction stabilization (NRS) entails the problem of minimizing errors due to noise without removing small changes in $Z_0(\cdot)$ due to fine details in $\sigma(\cdot)$.

NRS may be directly applied to the measured data. Commonly used techniques in magnetotellurics involving NRS on the input data employ coherence relationships and remote reference processing, the use of spectral whitening, and χ^2 filtering constraints. Other techniques are also used to accomplish NRS at the output, for example, by using any known geologic information to help constrain the solution. More general algorithms of this type penalize rapid variations in the estimate of $\sigma(\cdot)$ and require increasing smoothness with increasing depth. These algorithms are based on the difficult to quantify but qualitatively obvious truth that resolution degrades with depth. The difficulty arises

¹ We adopt the convention that σ will refer to conductivities that vary only as a function of space, $\sigma = \sigma(\bar{r})$, while $1/\rho$ will refer only to conductivities that vary with frequency, *i.e.*, apparent resistivities of the form, $\rho = \rho(f)$.

not only because M_z^{-1} is high pass, but also because it is nonlinear, and furthermore nonlocal, involving all of $Z_0(\cdot)$ in principle for each $z \geq 0$.

The NRS approach represented by the spectral regularization objective \mathbf{J}_v penalizes lack of smoothness due to noise at the input. Put simply, we employ a smoothness constraint on an input observable which, in the noise-free case, is known to be very smooth. This is in contrast to applying a direct spatial smoothness constraint on $\sigma(\cdot)$ which may be significantly *non-smooth*. Indeed, when attempting to detect manmade structures, the regions where $\sigma(\cdot)$ is not smooth are of paramount interest. In addition, the input smoothness constraint we describe is derived from the physics of the problem, whereas output smoothness constraints are typically *ad hoc*, given the difficulties in the direct analysis of the nonlinear functional operator M_z^{-1} . Nevertheless, one must still eventually deal with output constraints in order to address the destabilization implicit in the forward smoothing posed by M_f when the data are noisy. The method we discuss may be viewed as taking some of the smoothing responsibility off this last step, and therefore helping to maintain maximum resolution.

2.2.5. Complex Apparent Resistivity

A further difference appears in the choice of the quantity computed by the regularization algorithm. The well known apparent resistivity has the form

$$\rho_a = \frac{|Z|^2}{\omega\mu_0}.$$

This contains no phase information since the absolute value of the impedance has been taken. Often, in standard magnetotelluric analysis, the phase of Z is used in conjunction with ρ_a so that this phase information is not lost. This approach leads to awkward calculations since the ρ_a and phase functions must be manipulated separately. A more practical definition, which allows the field properties of the complex numbers to take care of both the magnitude and phase simultaneously during calculation, is to define

$$\rho_c = \frac{Z^2}{j\omega\mu_0},$$

which we call the complex resistivity. In the noise-free case, the electric field leads the magnetic field by 45° in a resistive half-space so that $\arg Z^2 = \pi/2$ and therefore ρ_c , although defined in terms of complex quantities, delivers a real number as it should in this simple situation.

Use of this complex resistivity makes it straightforward to derive the basic physical relationship that is exploited in spectral regularization. For the one-dimensional problem, the magnitude and phase of the complex resistivity ρ_c are related by the well known Kramers-Krönig dispersion relations. For example, the phase can be expressed in terms of the logarithm of the magnitude of the complex resistivity as

$$\angle \rho_c(f) = \frac{2}{\pi} \int_0^\infty \log |\bar{\sigma} \rho_c(\varphi)| \frac{f d\varphi}{f^2 - \varphi^2},$$

where $\bar{\sigma}$ is taken as the "background" conductivity for which $\bar{\sigma} = \sigma(\infty)$. This relation holds without reference to the good conductor approximation and so is valid at any frequency. In the case of a constant half-space, $\rho_c(f) = 1/\bar{\sigma}$ for all f , not merely in the limit for well defined $\sigma(z)$, and so $\log |\bar{\sigma} \rho_c| = 0$, implying $\angle \rho_c(f) \equiv 0$, i.e., $\rho_c(f)$ is real, as mentioned above.

A logarithmic change of variables converts the above expression into a convolution with an odd kernel. Integration by parts therefore results in an even kernel, one having very rapid decay, which when approximated using a Dirac δ -function results in

$$\angle \rho_c(f) \approx \frac{\pi}{4} \frac{d \log |\rho_c(f)|}{d \log f}.$$

This approximate expression is well known in the magnetotelluric community, and provides a good approximation for cases with one-dimensional conductivity variation. By using this expression, we can write

$$\begin{aligned} \frac{d\Lambda}{d \log f} &= \frac{d}{d \log f} [\text{Log} |\rho_c| + j \angle \rho_c] \\ &\equiv \frac{2}{\pi} \angle \rho_c + j \frac{d \angle \rho_c}{d \log f} \end{aligned}$$

with the result

$$|f\Lambda'|^2 \approx \left(\frac{2}{\pi}\right)^2 |\angle \rho_c|^2 + |f \angle \rho_c'|^2$$

In other words, minimizing the prior component of the \mathbf{J}_v objective, as suggested by the Kramers-Krönig relation, may be viewed as minimizing a weighted sum of the squares of the differences between the observed phase and group phase and those that would be observed for a space with only a one-dimensional conductivity variation.

This approximation can also be expressed in an equivalent form

$$f\Lambda' = f \frac{\rho_c'}{\rho_c}$$

which is particularly convenient when the complex resistivity parameterization is used. Like conventional regularizers based on derivatives of the apparent resistivity, this method stabilizes the initial ill-posed problem. However, unlike conventional regularizers, its form is based on a reasonable physical approximation rather than an *ad hoc* choice made for computational convenience.

2.2.6. Summary of Imaging Method

The expressions derived above are of course approximate, but they can be used to address the input NRS problem in a systematic fashion based on physical principles. The convolution expressions (not shown here) can themselves be employed as constraints without resort to approximation, other than in a modeling sense, but this approach has some difficulties that have yet to be addressed. We have described the reasoning leading to an optimization objective of the form

$$\mathbf{J}_v[\kappa, \lambda](\Lambda) = \int \overline{C}_\kappa |\Lambda - \tilde{\Lambda}|^2 df + \lambda \int |f \Lambda'|^2 df .$$

Minimization of the above form results in an optimal Λ that is conditioned on an approximate half-space model. Hence, solution anomalies may then be interpreted as due to physical departures from this half-space model. Several generalizations of the basic approach follow immediately.

The basic principle is clear: before any inversion proper, it is useful to filter the data so that it more closely respects the Kramers-Krönig relation. This physically justifiable smoothing process is applied to noisy data that is known to be smooth when no noise is present. The form of the filter is simple: more smoothing is applied at the higher frequencies than the lower ones. The above Lagrangian form can of course be posed using different metrics. From the computational point of view each of the above optimizations can be implemented using fast and stable signal processing techniques.

3. Electromagnetic Modeling and Inversion

Previous theoretical and computational investigations of underground conductivity imaging using low frequency methods have been performed mostly for geological structures; there has been very little work performed in modeling underground targets of military interest. Consequently, this contract includes a significant modeling effort specifically aimed at determining the characteristics of man-made targets. The results of this effort are being used to plan experiments, evaluate and improve the performance of signal processing and inversion algorithms, choose source signals, and predict observables associated with complex underground structures.

To perform this work, APTI has employed a set of standard geophysical simulation and inversion programs, with parameter settings properly adapted to the characteristics of man-made targets, to study the response of underground structures of military significance. The results of these efforts to date are described in the following sections.

In Section 3.1, we present the results of two-dimensional forward simulations of an underground tunnel, both in a half-space with uniform conductivity and in the presence of thin conductive surface layers. These forward simulations were performed using the finite element code PW2D, developed by Wannamaker and Stodt¹. Several cases with varying ratios of tunnel depth to tunnel size were investigated. In Section 3.2, we present the results of inverting this simulated data with a standard geophysical inversion code, the Rapid Relaxation Inverse program developed by Smith and Booker², and an analysis of the results.

¹ P.E. Wannamaker and J.A. Stodt, A Stable Finite Element Solution for Two-Dimensional Magnetotelluric Modeling. *Geophys. J.R. Astr. Soc.* **88**, pp. 277-296 (1987).

² J.T. Smith and J.R. Booker, Rapid Inversion of Two- and Three-Dimensional Magnetotelluric Data. *J. Geophys. Res.* **96**, No. B3, pp. 3905-3922 (1991).

3.1. Forward Modeling

An example of the models used in the forward simulations is shown in Figure 6. This model contains a uniform half-space with resistivity 100 Ohm-m, and a 15 × 15 m tunnel at a depth of 50 m. From this base situation variations in tunnel size, as well as the effects of conducting surface layers, were examined. The resistivity of the tunnel interior was taken as 10^4 Ohm-m. In all cases discussed here the TM mode (surface E field in the x -direction) was used; this is the most significant mode for the resistive tunnels considered here. The frequencies used in the simulations spanned the range from 100 Hz to 100 kHz. For forward model creation, the UNIX based graphical user interface MTWorks was used. Further calculations were performed by exporting the results from MTWorks and importing them into Matlab. Computations were performed on a Sun Ultra 140 with 320 Megabytes of RAM; computation time for a typical forward model with 10,000 elements was of the order of two to three hours for 45 frequencies.

3.1.1. Uniform Half Space

The objective of the first set of simulations, whose results are shown in Figures 7-10, was to investigate the effect of the depth-to-size ratio on the field perturbation at the surface, as a function of frequency and horizontal distance from the tunnel center. The response to square tunnels with sizes 5 meters (Figure 7), 10 meters (Figure 8), 15 meters (Figure 9) and 25 meters (Figure 10) was studied. These correspond to depth-to-size ratios of 2, 3.3, 5, and 10. The right-hand sides of Figures 7-10 show the apparent resistivities while the left-hand sides show the phase of the impedances as a function of the frequency and horizontal position. As a benchmark, note that the skin depth at 8 kHz is approximately 56 m, close to the tunnel depth; we would expect the tunnel response to be most evident near that frequency.

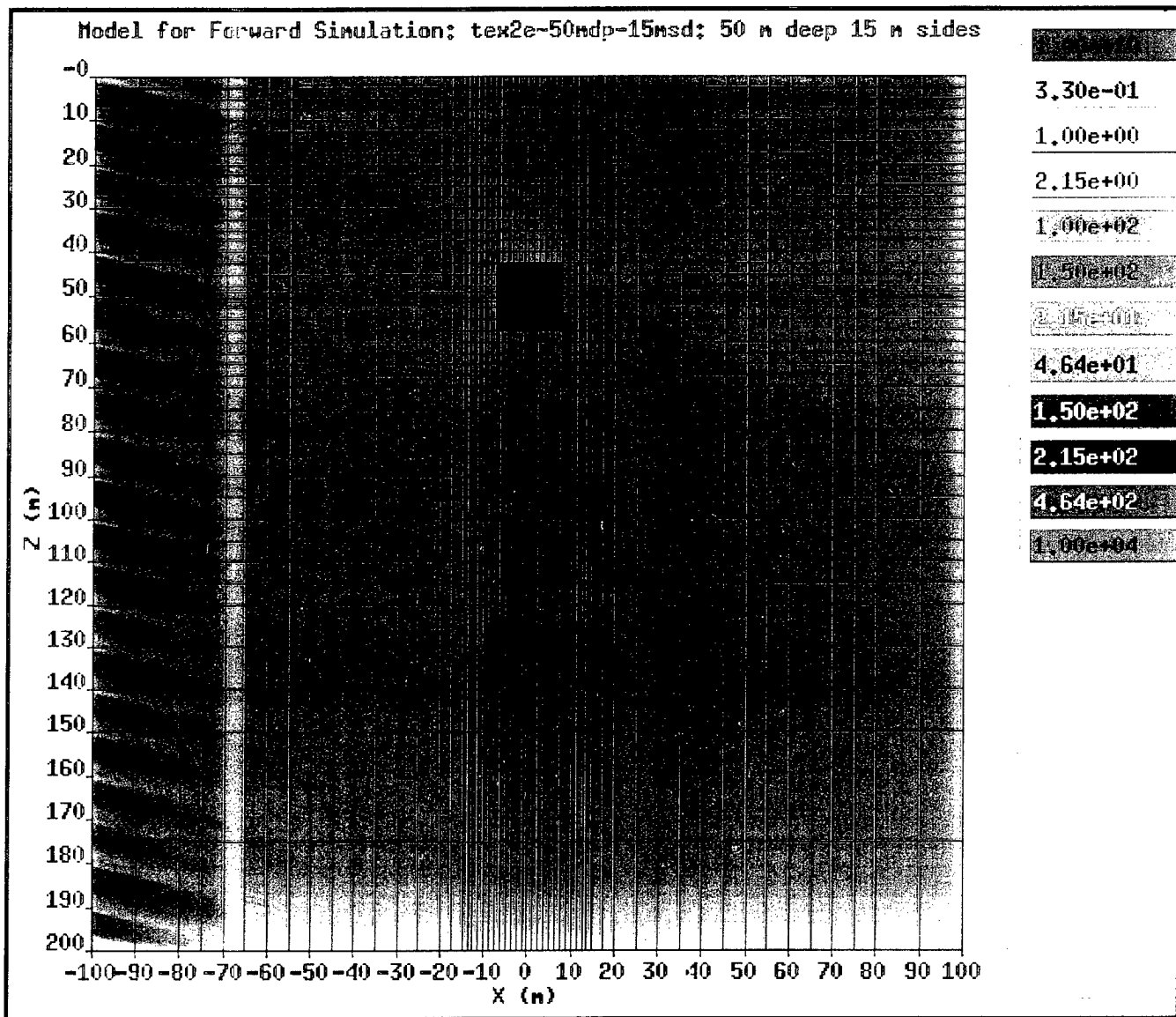


Figure 6. Example Finite Element Model for Forward Simulation.

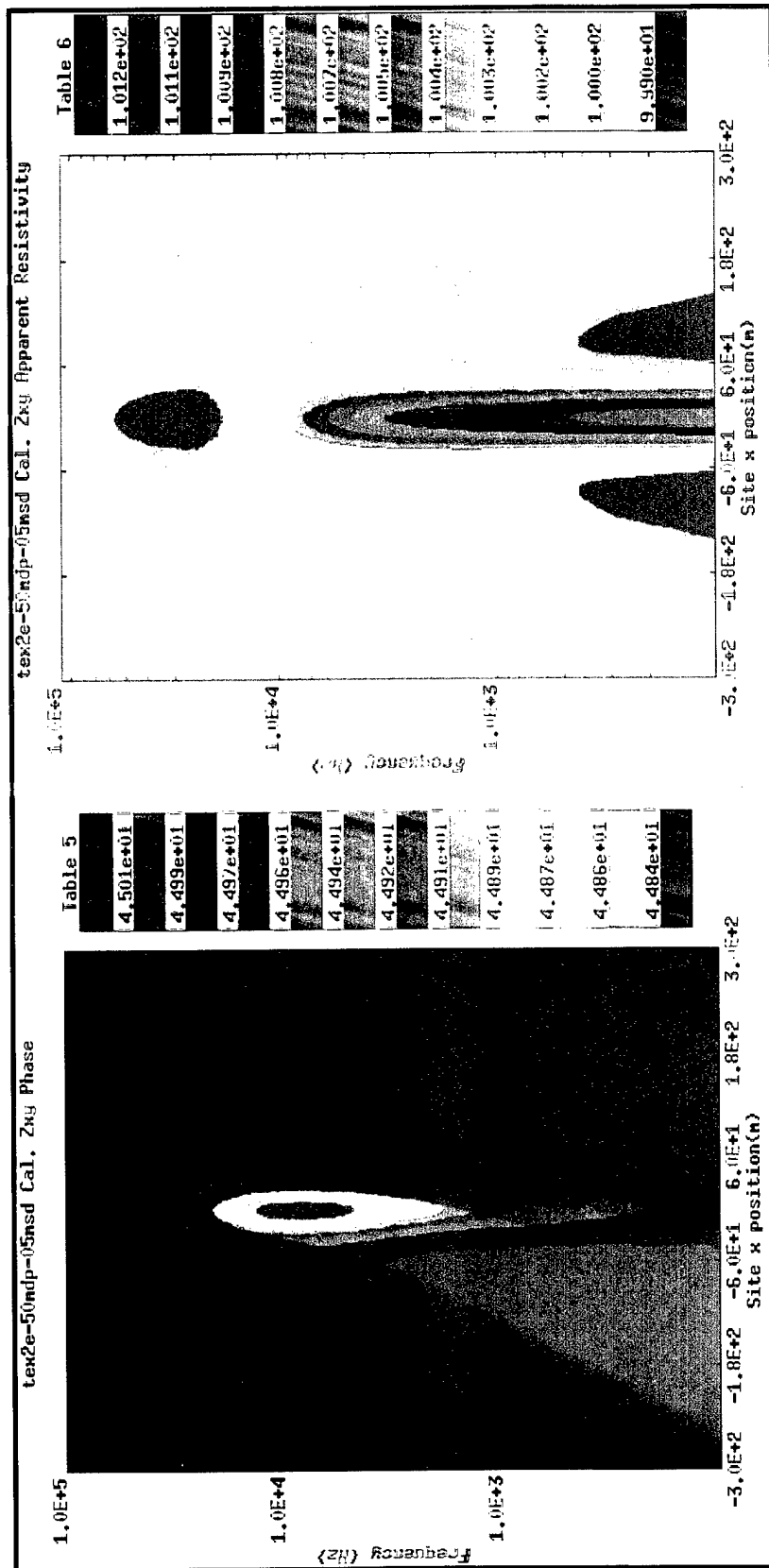


Figure 7. Forward Simulation Results for 5m Tunnel 50m Deep.
Background is 100 ohm-m.

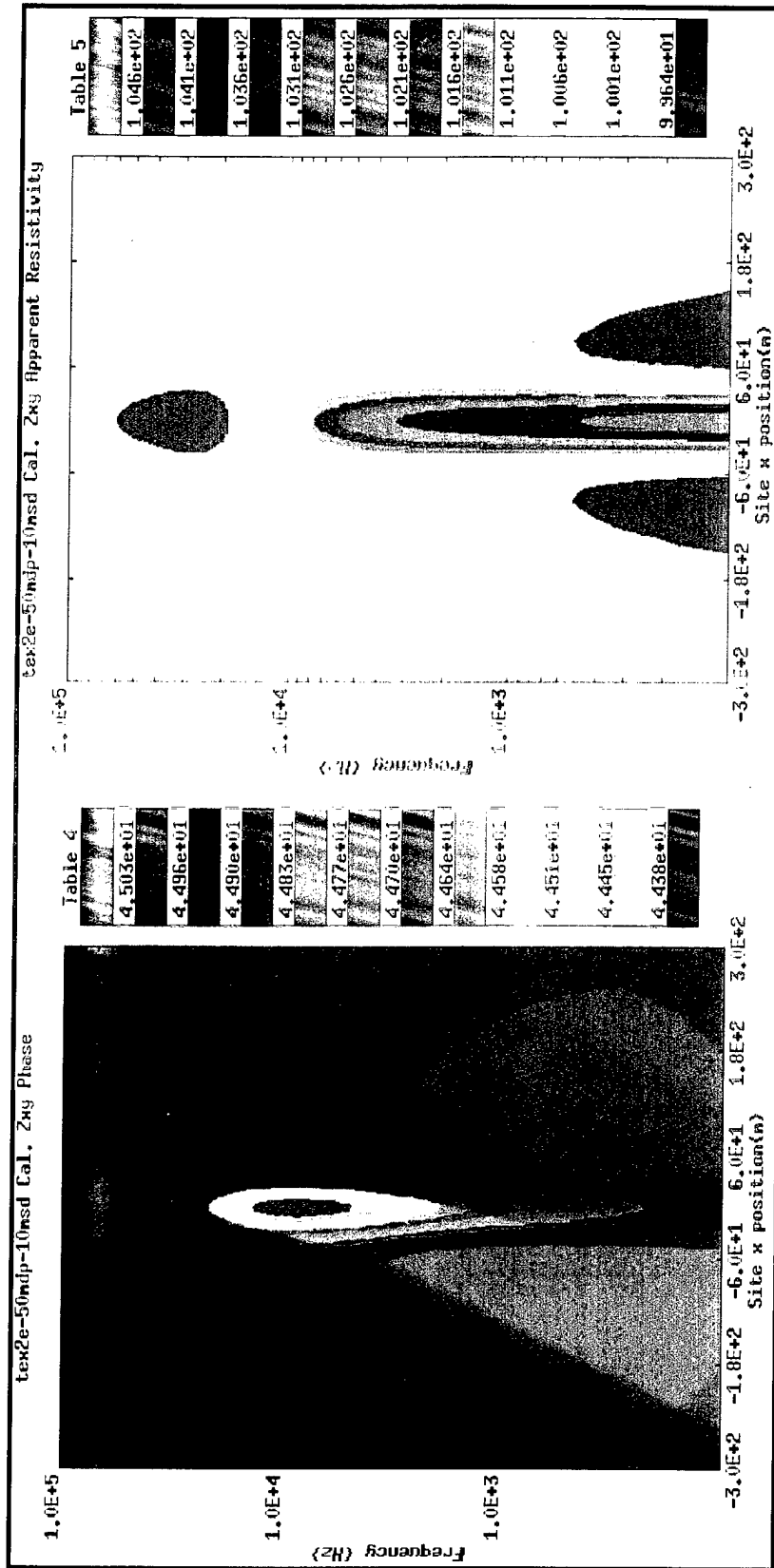


Figure 8. Forward Simulation Results for 10m Tunnel 50m Deep.
Background is 100 ohm-m.

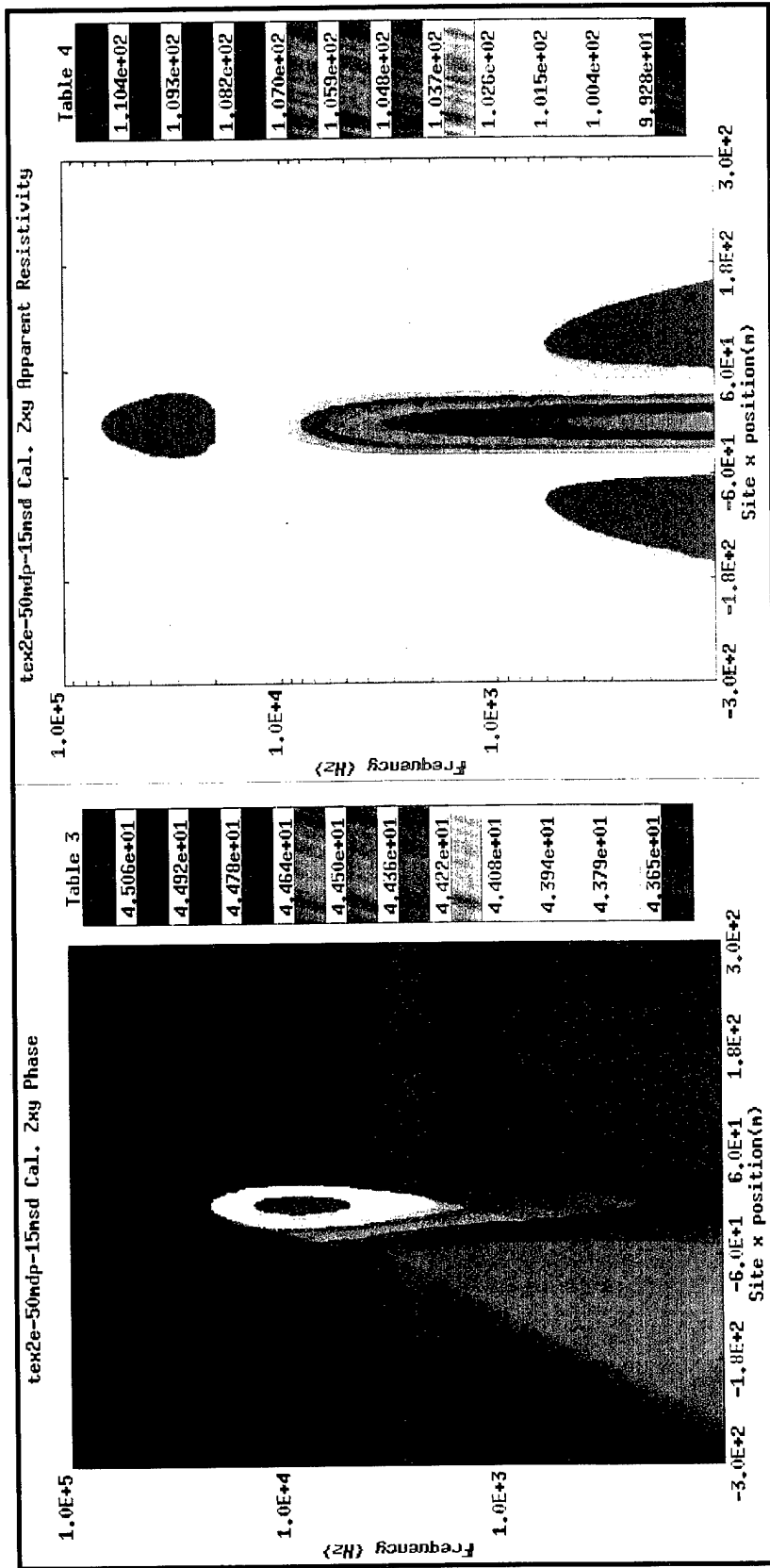


Figure 9. Forward Simulation Results for 15m Tunnel 50m Deep.
Background is 100 ohm-m.

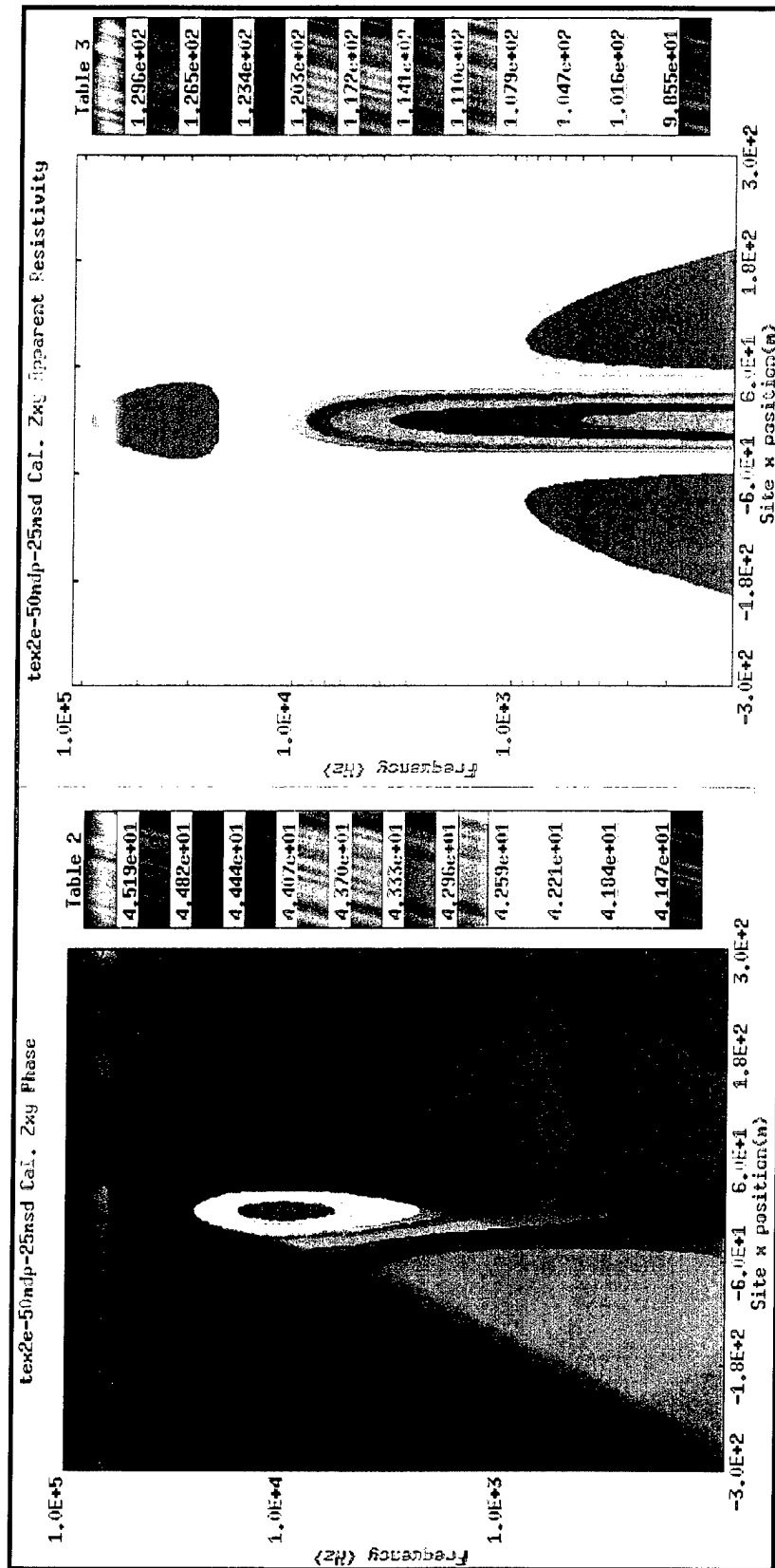


Figure 10. Forward Simulation Results for 25m Tunnel 50m Deep.
Background is 100 ohm-m.

It is apparent that self-similar patterns, whose intensity falls with the area of the tunnel, are present. Concentrating on the features of Figure 7, we note that the maximum phase lag (approximately 4 degrees) occurs at a frequency corresponding to a true depth to skin depth ratio of approximately 0.8, consistent with Bostick's analysis. On the other hand, the maximum of the apparent resistivity (130 Ohm-m) appears at frequencies well below 500 Hz and has the expected form of an electrostatic umbra. The field perturbations due to the presence of the tunnel extend to lateral distances of the order of 100 m. Finally, the sign of the slope in both phase and resistivity changes at lateral distances of the order of 60 m. Of utmost importance to our inversion procedure, to be discussed later, is the correlation of the phase and apparent resistivity data, which under half-space conditions should satisfy the Kramers-Kronig relations. From Figures 7-10 we see that over the entire frequency region below 20 kHz, the relationship between these quantities is different from the constant expected for half-space. This can be used as a robust constraint in inversions involving localized anomalies due to the presence of resistive or conducting tunnels.

The effect of the tunnel size on the measurements becomes clearer by referring to Figures 11 and 12, which show the differences between the apparent resistivity and phase directly above the tunnel and at a horizontal offset of 50 meters. Both quantities scale as the inverse of the area occupied by the tunnel, as expected on the basis of theoretical considerations.

Figures 13 and 14 show the differences of measurements taken between stations located at 25 and 50 meter horizontal offsets. These, in conjunction with the results shown in Figures 11 and 12, allow us to characterize the approach to half-space response with distance from the tunnel. It can be seen that the response is self-similar with respect to frequency, but the amplitude of the deviation scales with the inverse square of the lateral distance.

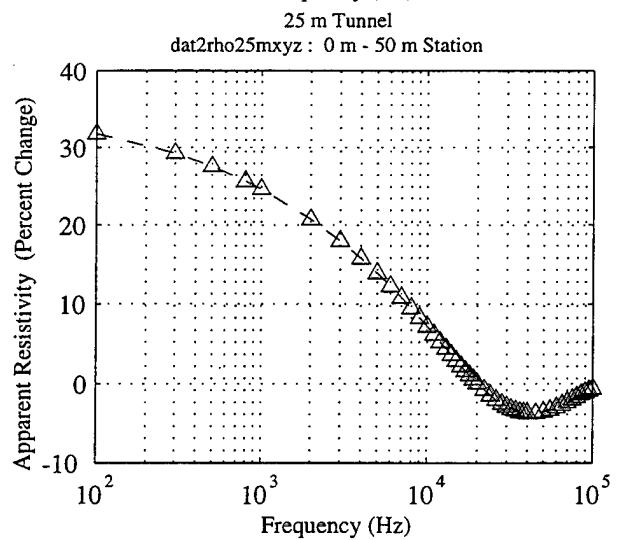
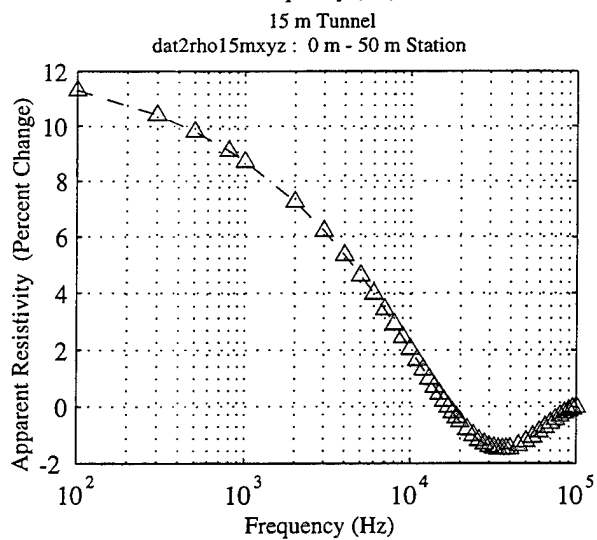
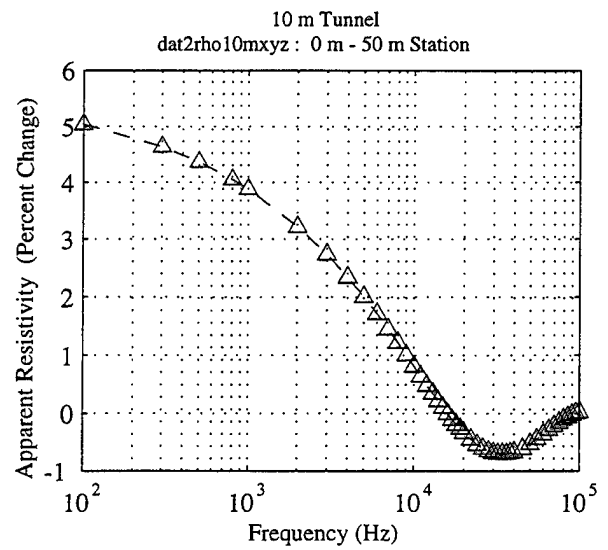
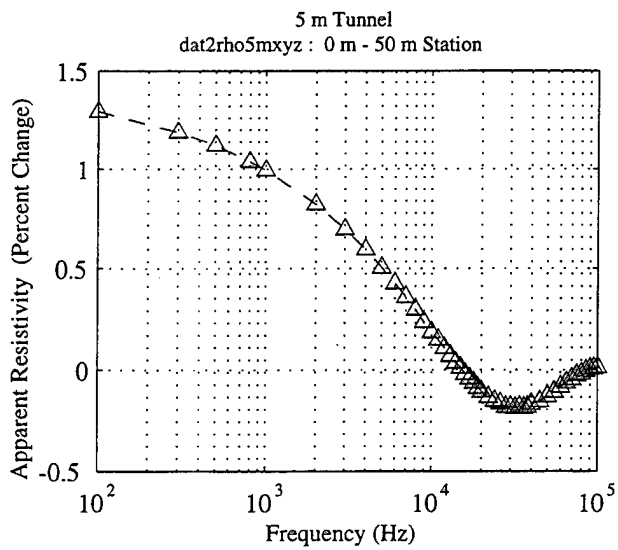


Figure 11. Vertical Cuts of Data in Figures 7 - 10. Change in Apparent Resistivity Directly Above Tunnel vs. 50m Away

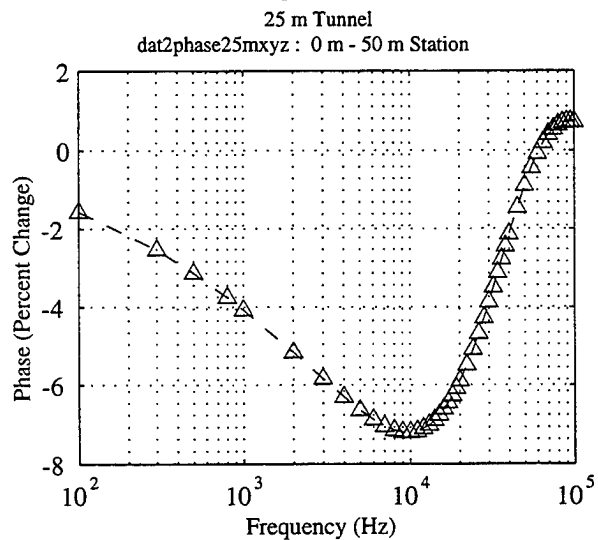
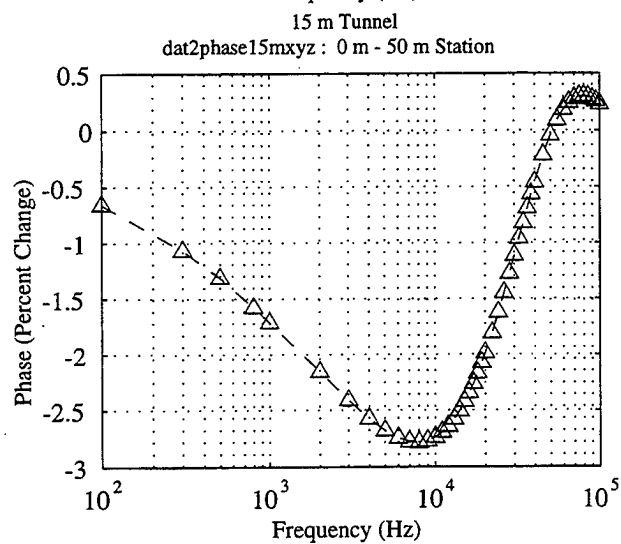
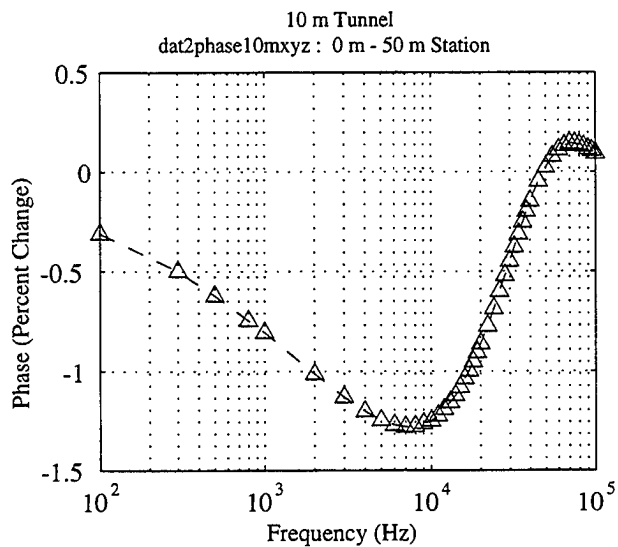
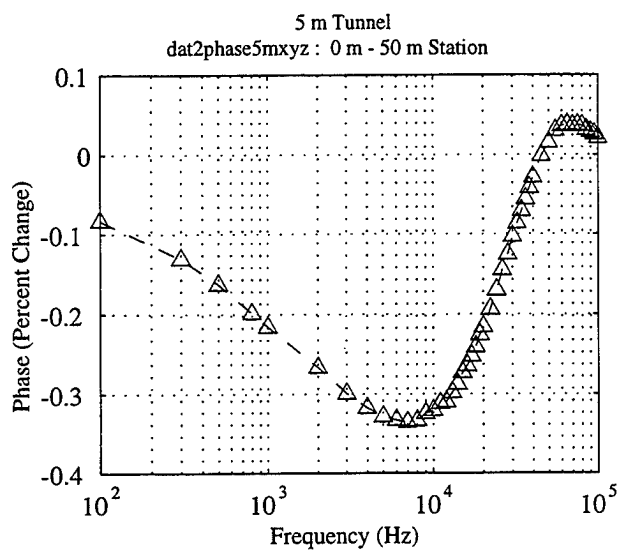


Figure 12. Vertical Cuts of Data in Figures 7 - 10. Change in Phase of Impedance Directly Above Tunnel vs. 50m Away

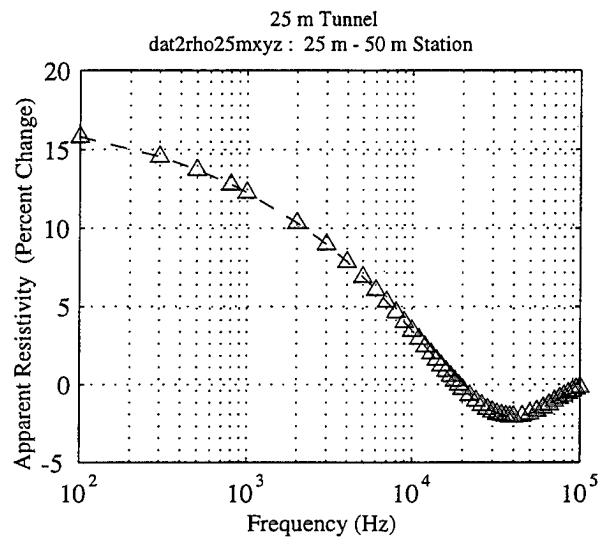
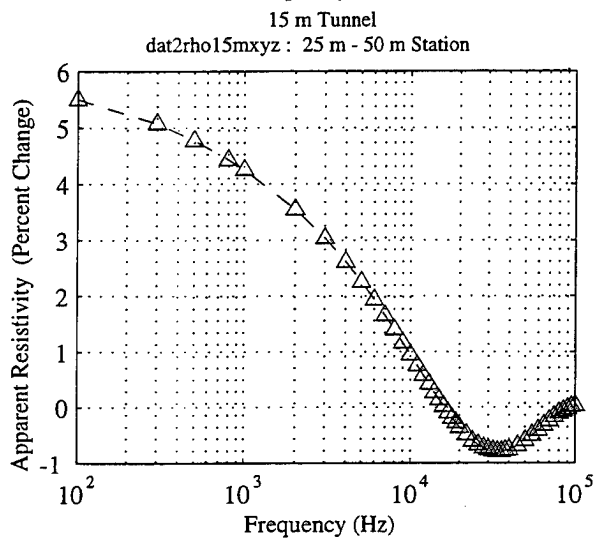
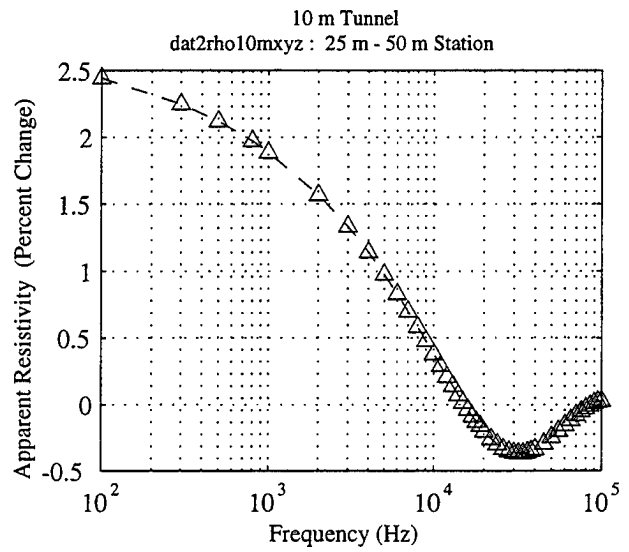
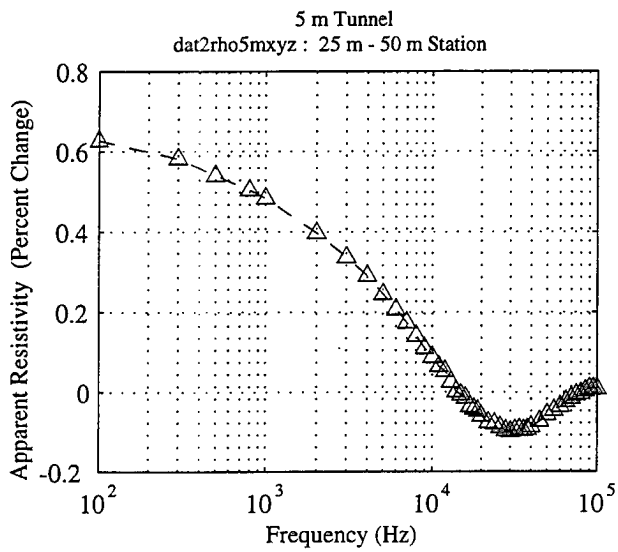


Figure 13. Vertical Cuts of Data in Figures 7 - 10. Change in Apparent Resistivity from 25 - 50m Horizontal Distance from Tunnel.

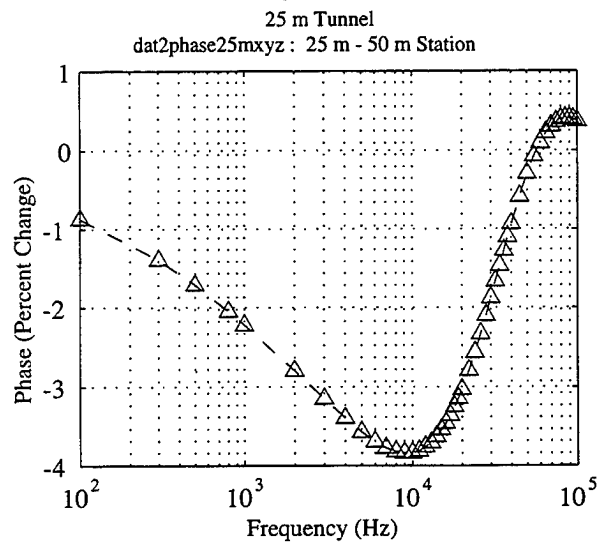
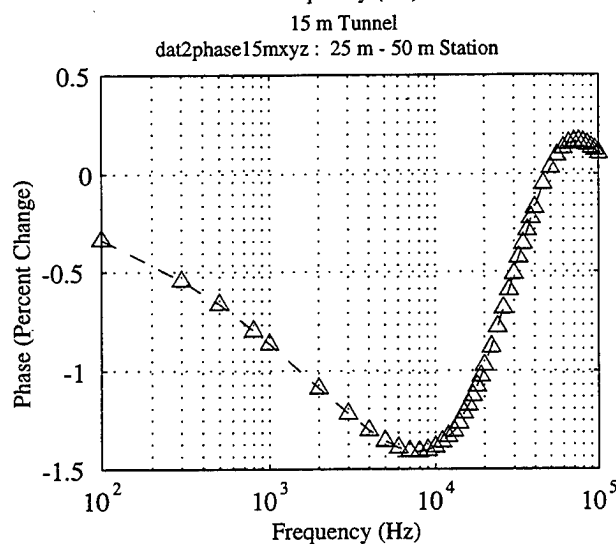
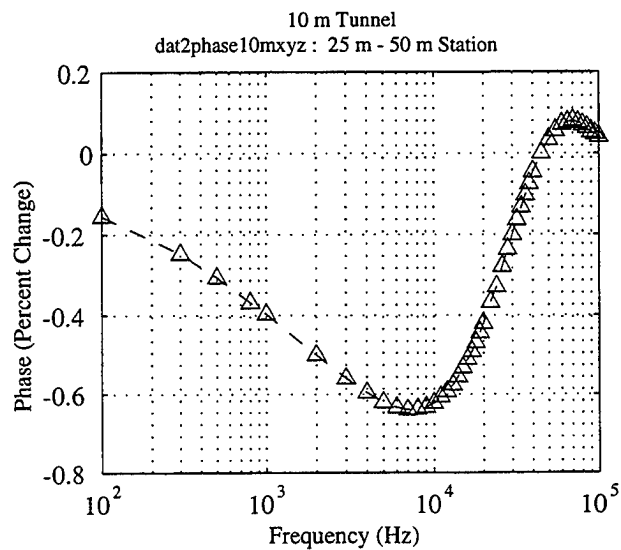
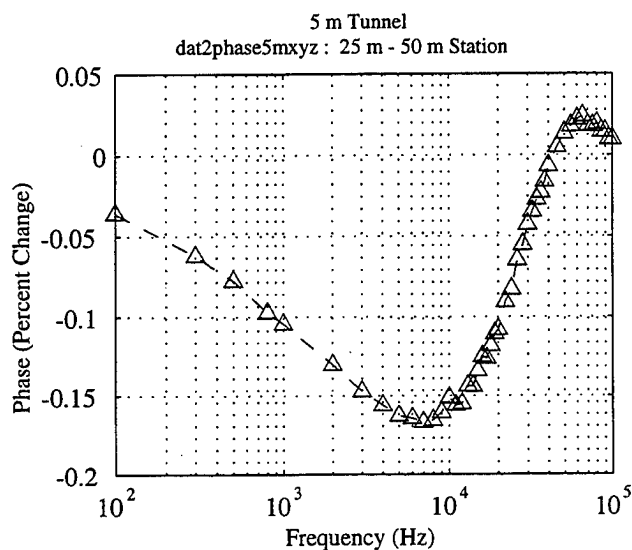


Figure 14. Vertical Cuts of Data in Figures 7 - 10. Change in Phase of Impedance from 25 - 50m Horizontal Distance from Tunnel.

3.1.2. Effect of Conducting Surface Layers

We have found that in all of our experimental studies, including imaging of the Silver Fox and the Golden Zone mines, the effects of surface layers with higher conductivity were important in estimating the tunnel depth. A set of simulations was performed to examine the effect of such layers. The results shown below were conducted for a tunnel and background similar to the actual Golden Zone survey line 1 data, whose imaging is discussed in Section 4 of the report. The tunnel depth in the simulations was 28 m, its size 2.5×3.0 m, and the background conductivity 200 Ohm-m. Three simulated cases are shown here. Figure 15 shows the simulation results in the absence of a conducting layer, while Figures 16 and 17 show results in the presence of a conducting layer with resistivity 20 Ohm-m and thickness one meter, and resistivity 10 Ohm-m and thickness five meters, respectively.

As expected, the benchmark case shown in Figure 15 is essentially similar to the results of Section 3.1.1, once the results have been scaled for the changes in conductivity, depth and size. The maximum phase response is in the vicinity of 20 kHz. Figure 16 shows clearly the presence of a poorly resolved top conducting layer, as expected. However, the large phase shifts induced by the layer obscure the anomalies caused by the presence of the tunnel. In Figure 16, the tunnel appears as a small anomaly near 1 kHz. The conducting top layer acts as a low-pass filter, reducing the high frequency response. Notice, that contrary to the uniform half-space case, when a thin conducting layer is present both the phase and resistivity anomalies have the same frequency dependence. Finally, Figure 17 shows that a conducting layer with 5 m thickness and 10 Ohm-m resistivity completely masks the tunnel, at least within the frequency range used here. It is clear from the above results that surface conducting layers make detection of tunnels more difficult.

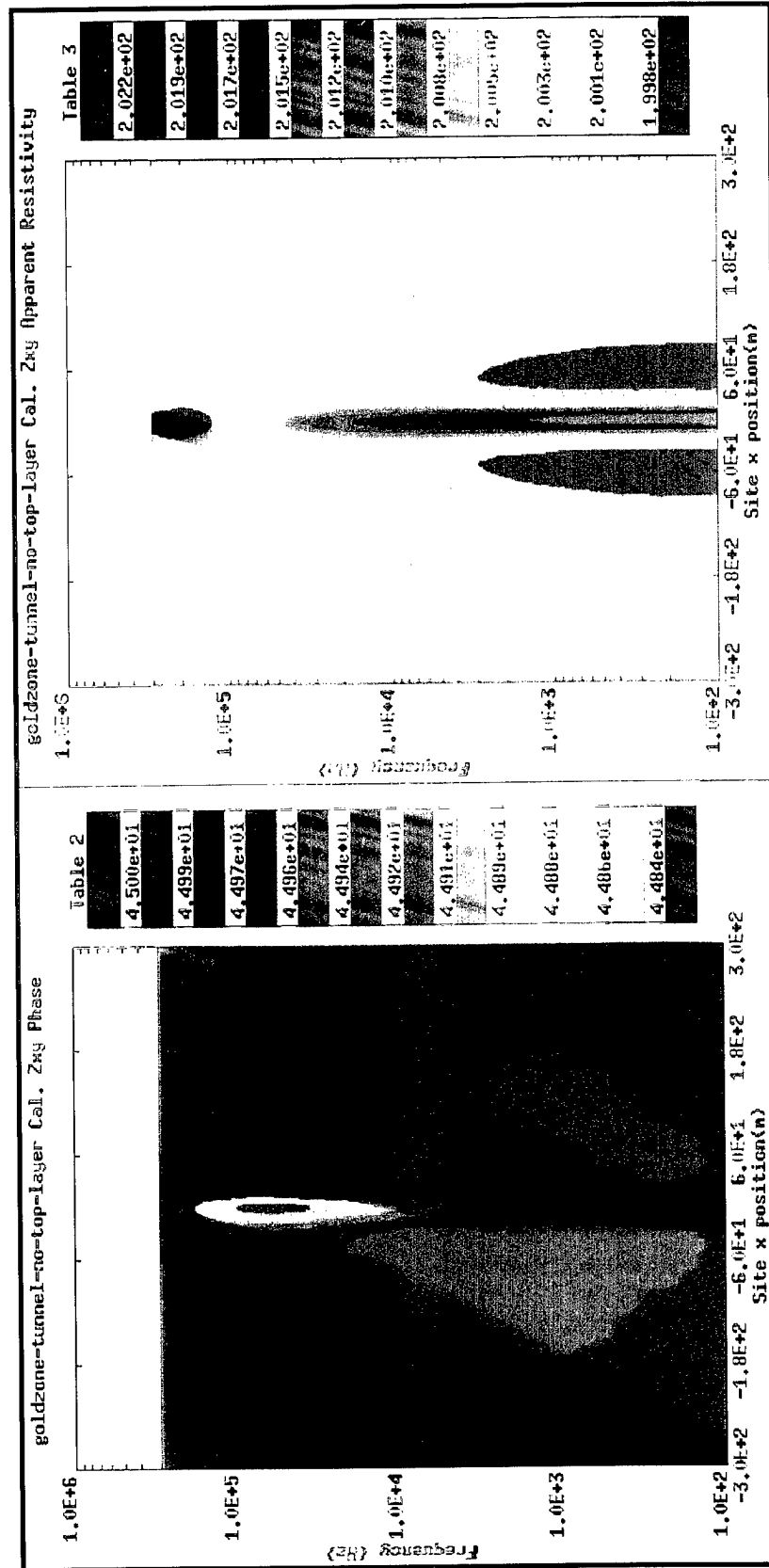


Figure 15. Forward Simulation Results for a Tunnel 2.5m high, 3.0m wide, 28m deep. Background is 200 ohm-m.

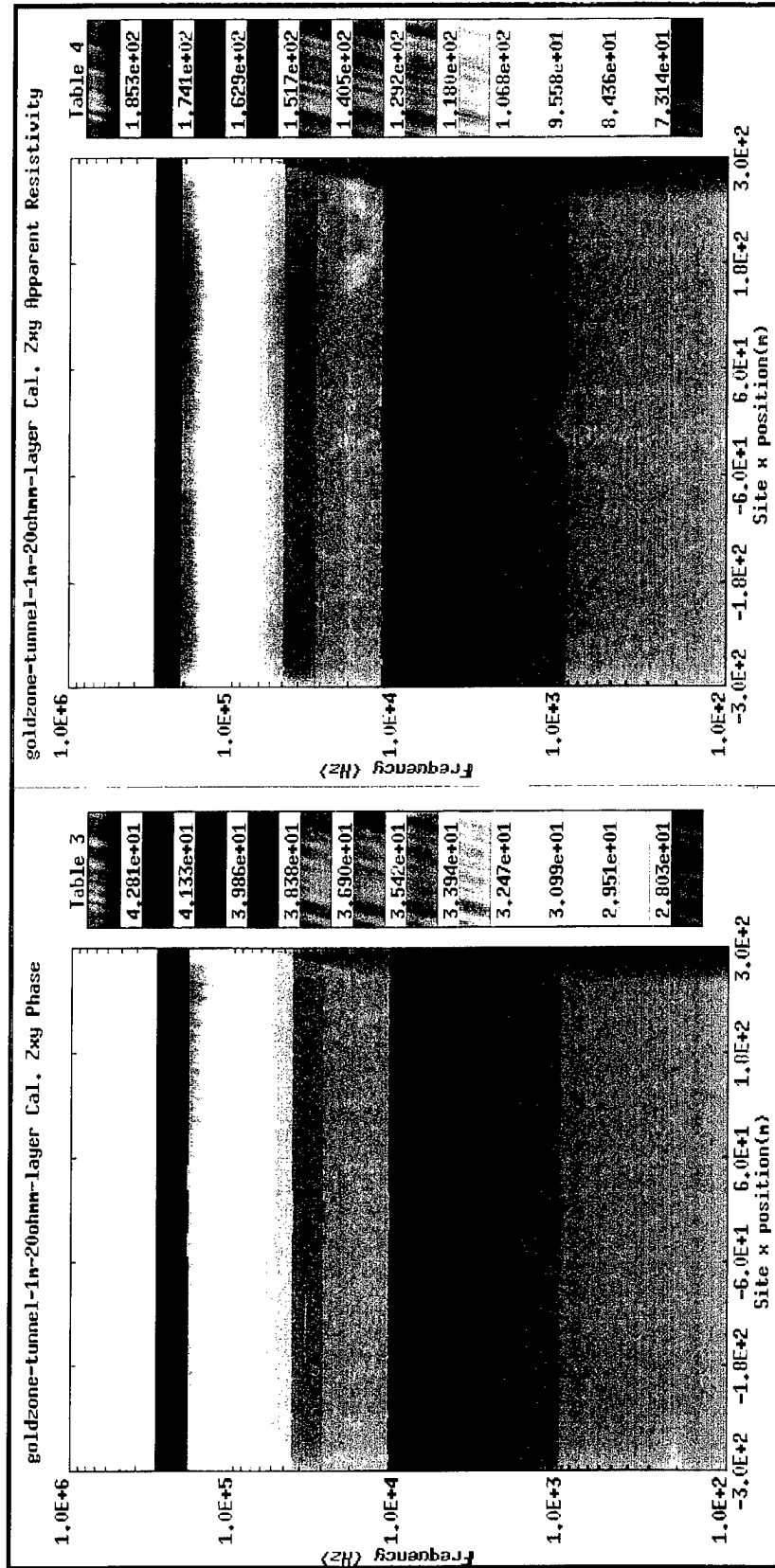


Figure 16. Conducting Top Layer Problem. Forward Simulation Results for a Tunnel 2.5m high, 3.0m wide, 28m deep. Background is 200 ohm-m. Top Layer is 1m thick and 20 ohm-m.

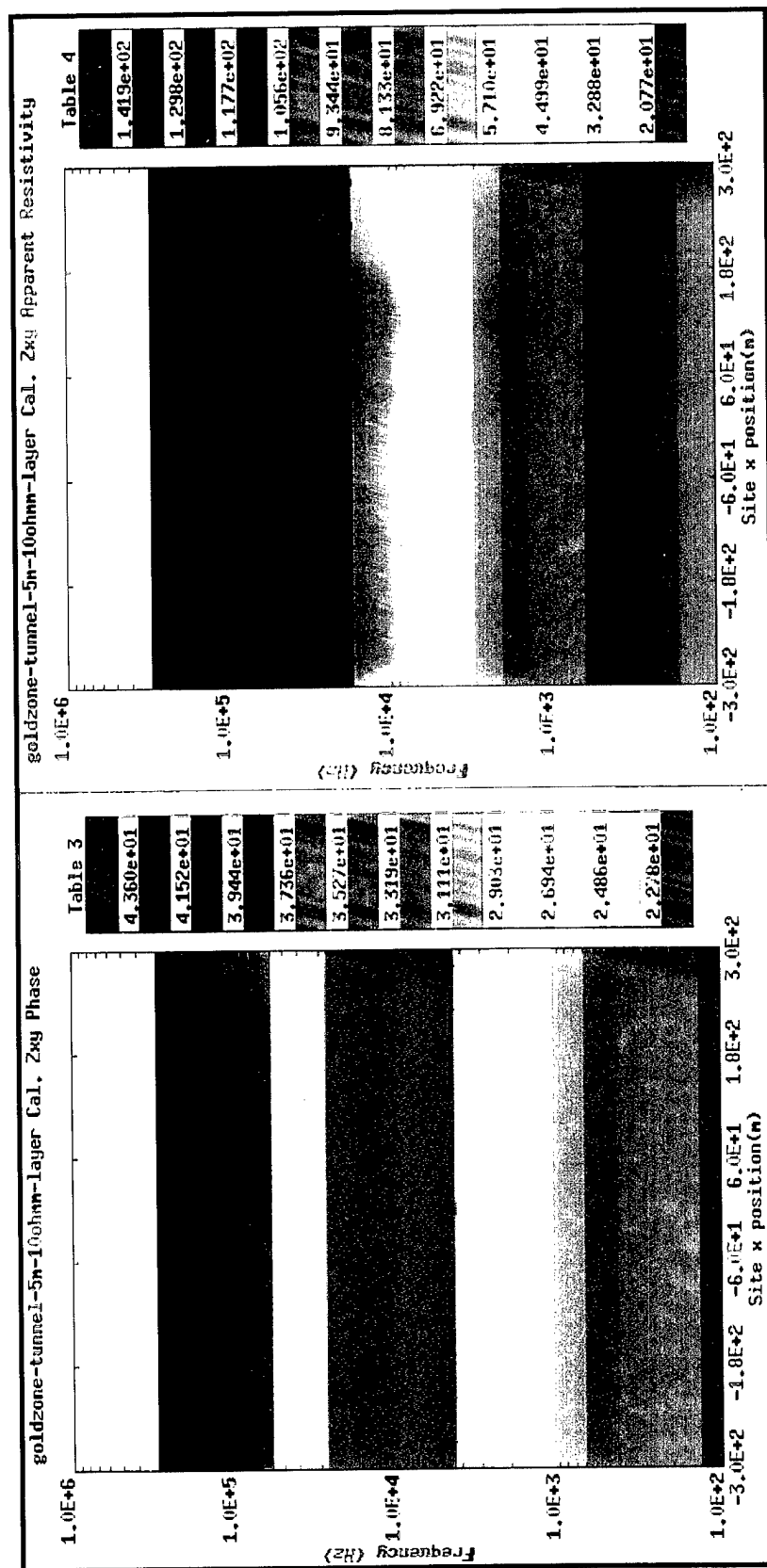


Figure 17. Conducting Top Layer Problem. Forward Simulation Results for a Tunnel 2.5m high, 3.0m wide, 28m deep. Background is 200 ohm-m. Top Layer is 5m thick and 10 ohm-m.

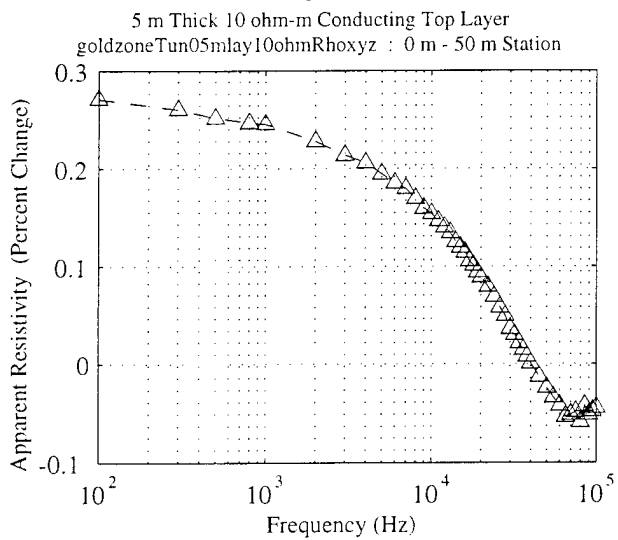
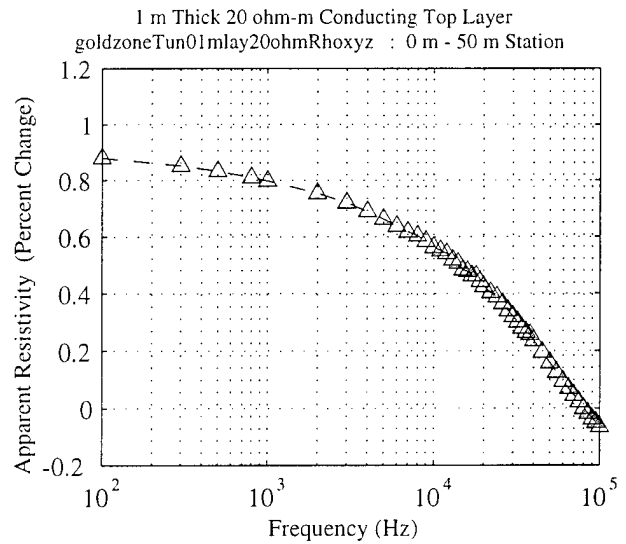
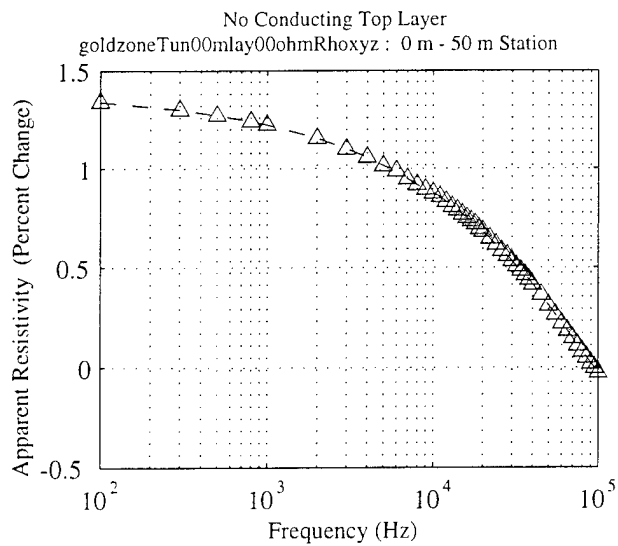


Figure 18. Conducting Top Layer Problem. Vertical Cuts of Data in Figures 15 - 17. Effect of Conducting Layers on Apparent Resistivity.

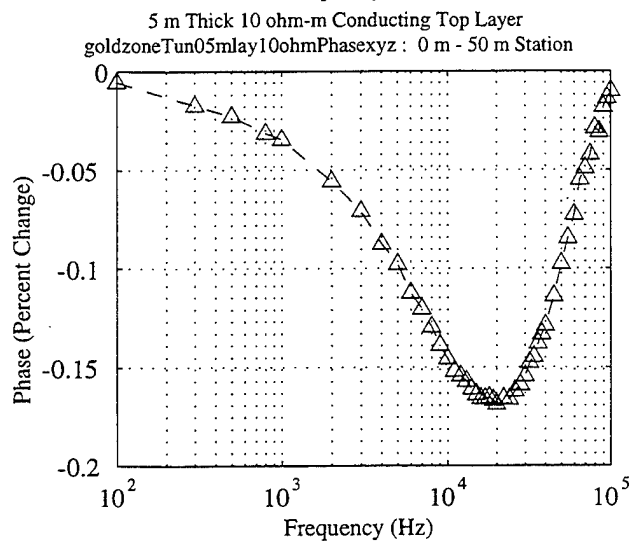
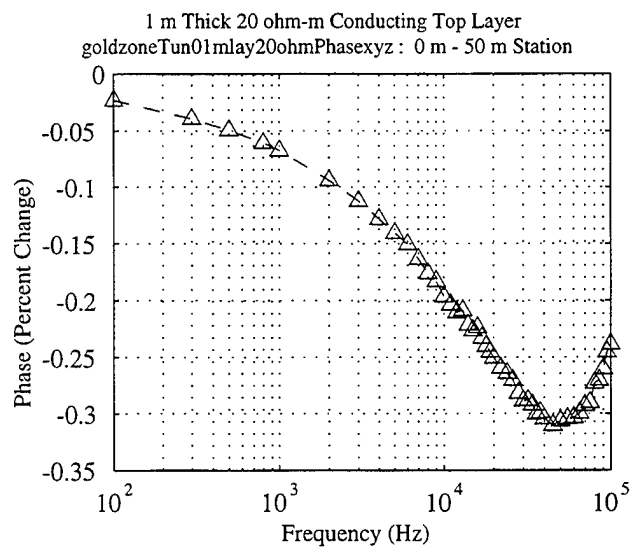
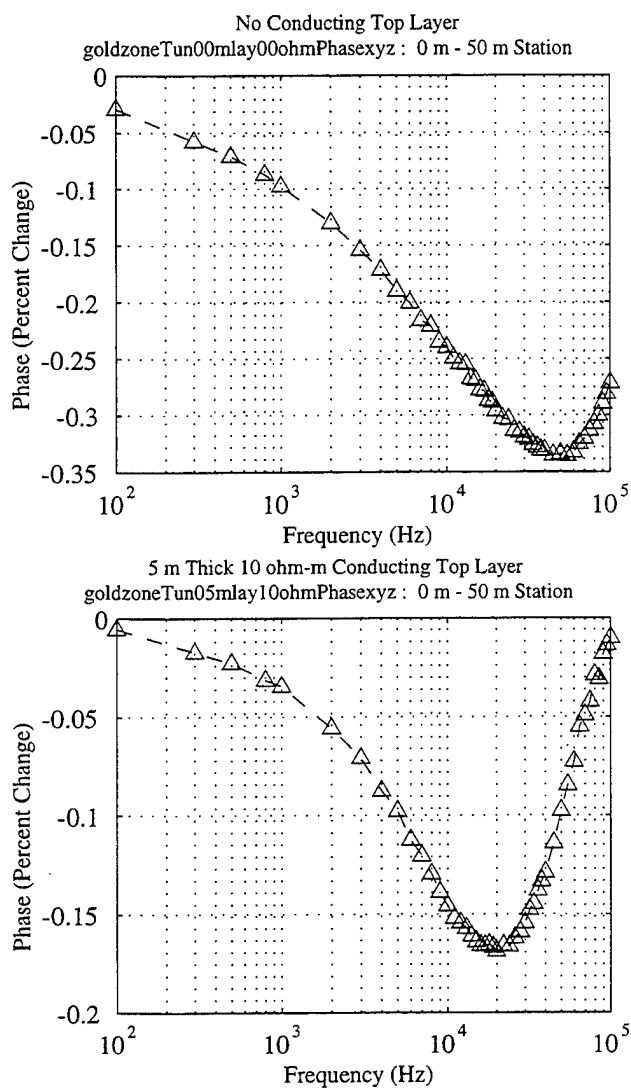


Figure 19. Conducting Top Layer Problem. Vertical Cuts of Data in Figures 15 - 17. Effect of Conducting Layers on Phase of Impedance.

Figures 18 and 19 show the difference in apparent resistivity and phase between measurements directly above the tunnel and 50 m away. It can be seen that the main effect of the conducting layer is to shift the maximum response towards the lower frequencies, while the amplitude of the response is reduced by a small factor. The presence of the tunnel can still be detected in both the apparent resistivity and the phase curves. The results shown above give further credence to inversion techniques using Kramers-Kronig relations as robust indicators of the presence of tunnel induced anomalies, even in the presence of thin conducting layers. They, furthermore, indicate that use of an equivalent half-layer can be useful in inversions. This issue will be addressed in Section 3.3.3.

3.2. Inversion of Modeled Data

To explore the limits of conventional techniques used in magnetotelluric exploration for imaging resistive underground structures of military interest (tunnels several diameters deep), we have performed inversions of the noise-free forward simulations presented above. To establish a benchmark for inversions of such structures, we chose a widely used geophysical inversion code, the RRI inversion code. For the inversions, we used forward simulated data for underground tunnels in uniform backgrounds with depth-to-tunnel size ratios between 3 and 10.

The results discussed below show that with simulated noise-free forward data accurate to 0.1 percent, RRI can produce a discernible image of a tunnel with a depth-to-size ratio of 10. Although the contrast between the image and the background is small, and imaging of a tunnel with this depth-to-size ratio is probably not possible using RRI on actual measured (not simulated) data, this result is itself unexpected. We have also found that the RRI has poor resolution on the small targets used, even when they are large enough to be clearly visible in the inversions.

In addition, we have studied how the sampling density of the surface measurements and the presence of conducting surface layers affect the resolution of the inversion. We found that the top conducting layer introduces a second conductivity contrast scale into the RRI inversion that can mask the presence of tunnels even though the tunnel is still detectable in the forward model data by comparing soundings above the tunnel with those far from the tunnel. To solve this multiple scale problem, we discuss an approach – mapping two layer tunnel inversions into equivalent uniform half-space tunnel inversions – that may improve detection and imaging sensitivity. Selected examples of the RRI inversion studies are presented below.

3.2.1. Resolution of RRI Inversions

We consider first the RRI inversion of a forward simulation for a 15×15 meter tunnel 50 meters deep. The model used as input for the forward simulation is shown in Figure 6, and produces the forward data shown in Figure 8. Figure 20 shows the result of an RRI inversion of these data. For this inversion, the forward data were sampled every 5 m between -80 m to $+80$ m. Data points at -100 m, -90 m, 90 m, and 100 m were also included. The inversion mesh extended horizontally from -100 m to 100 m at 2.5 m intervals and from zero to 100 m in depth at 5.0 m intervals. The initial model for the RRI inversions was a uniform half-space of 100 Ohm-m resistivity.

Three tunnel image distortion effects are apparent in Figure 20. First, the apparent tunnel depth is 90 m rather than 50 m. Second, the horizontal size, as measured by the width of the highest resistivity region of the image, is 25 m – over 60 percent larger than the model tunnel width. Third, the vertical size in the image is almost five times as large as the model tunnel height. On the other hand, we note that while the maximum numerical contrast in the forward model data is a 10 percent increase in apparent resistivity above background at 100 Hz, the inversion produces a peak increase of 19 percent above the background resistivity.

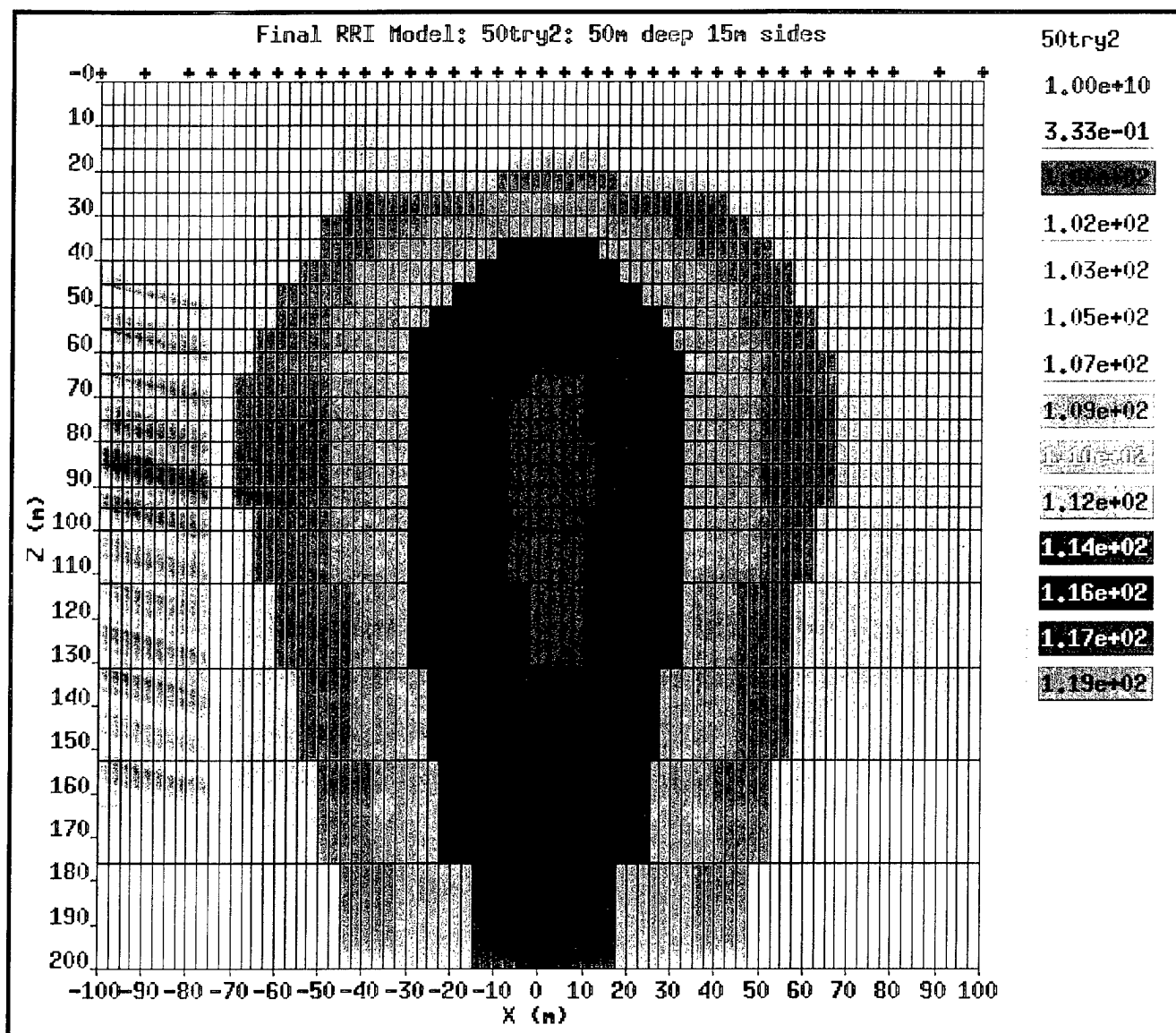


Figure 20. RRI Inversion of Forward Data from Figure 9.

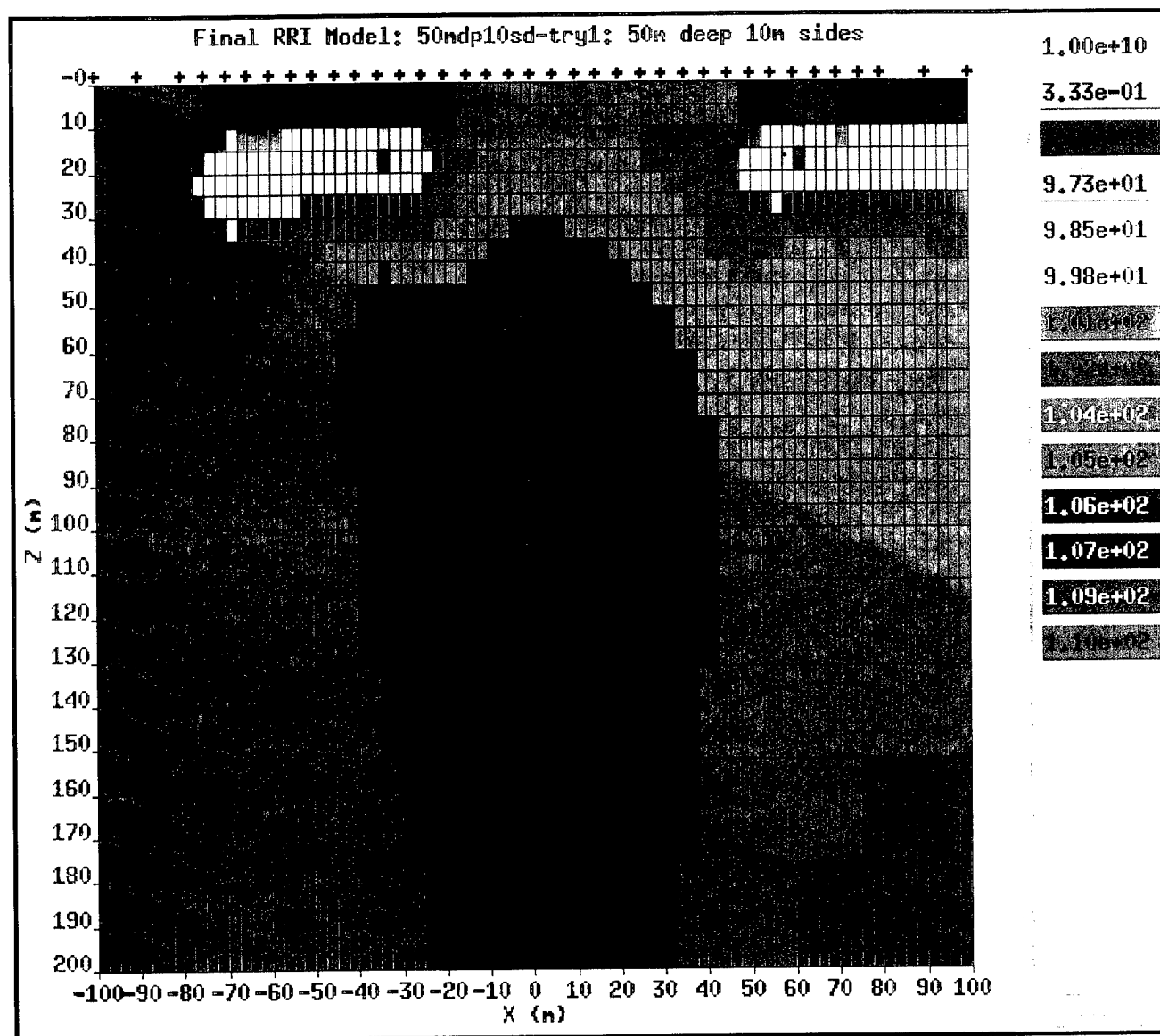


Figure 21. RRI Inversion of Forward Data from Figure 8.

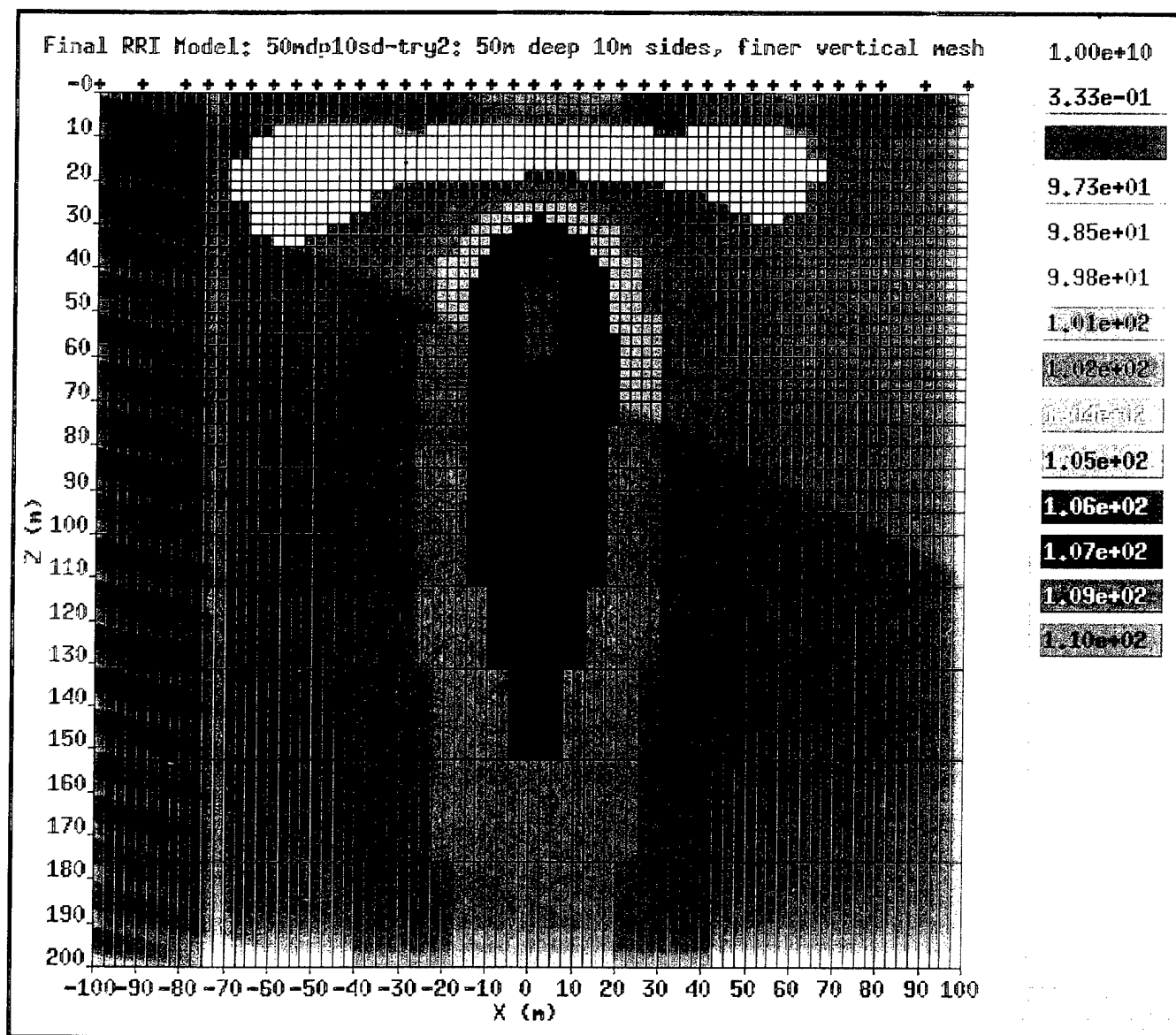


Figure 22. Finer Vertical Mesh (Relative to Figure 21) for RRI Inversion of Forward Data from Figure 8.

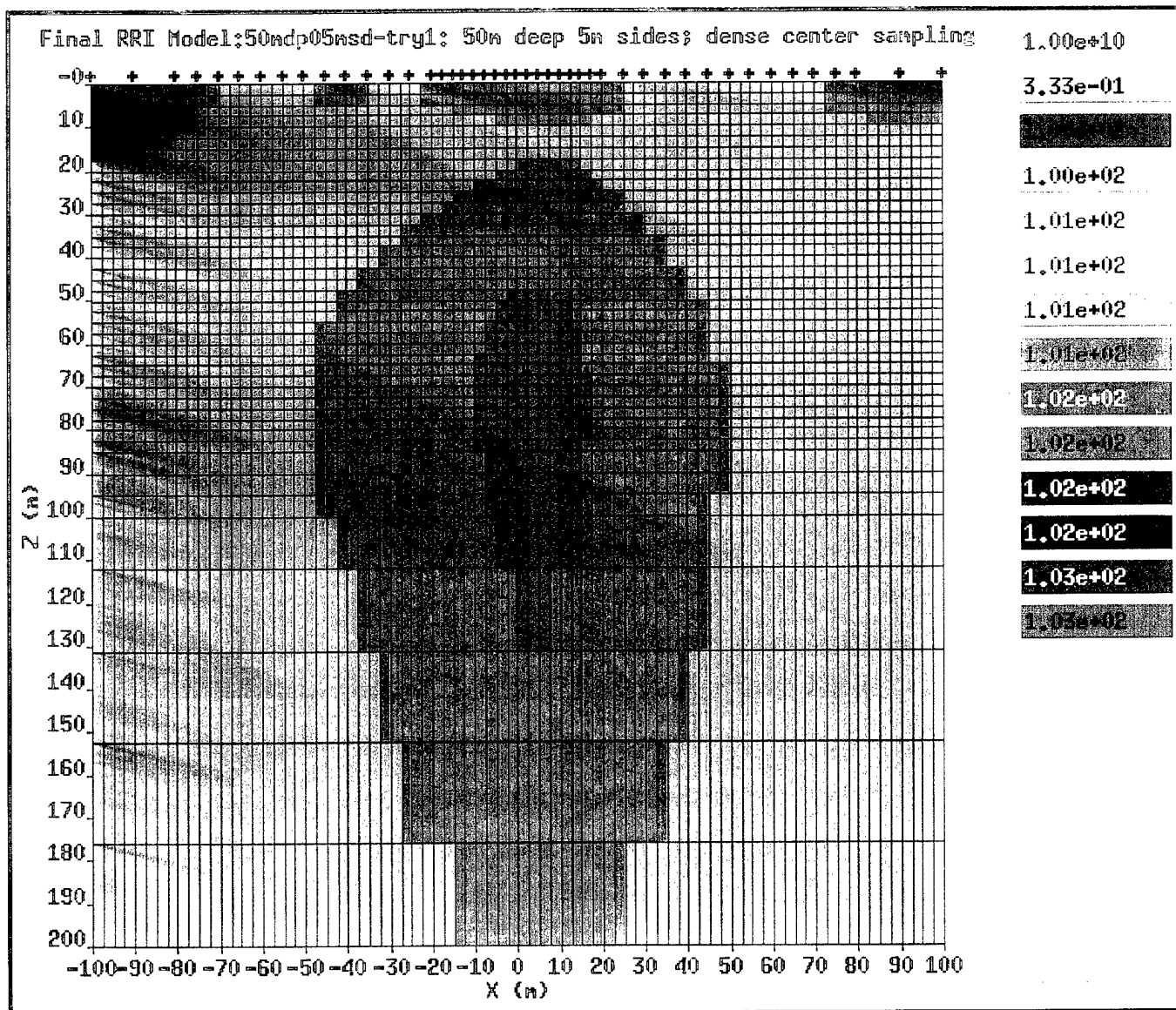


Figure 23. RRI Inversion of Forward Data from Figure 7.

Figures 21-23 show RRI inversions of smaller tunnels, and illustrate the effect of changes in inversion parameters on the images produced. The first example, Figure 21, shows a 10- meter tunnel inverted using the same parameters as Figure 20. Notice that the resolution is poorer and the contrast between the tunnel and the background has been reduced.

To improve the resolution, the vertical mesh spacing was decreased by a factor of 2, resulting in a vertical meshing interval of 2.5 m from zero to 100 m depth. The result of the inversion is shown in Figure 22. The increased vertical resolution allows RRI to compute more accurate forward data. The effect of this increased accuracy on the misfit calculation, and hence resultant inversions, depends on the size of the object of interest relative to the size of the mesh. For the 15×15 m tunnel, a vertical mesh of 5 m is one-third of a tunnel size; for the 10×10 m tunnel, a vertical mesh of 5 m is one-half a tunnel size. This is rather coarse for accurate calculations of the fields in the tunnel vicinity. Changing from a 5 m to a 2.5 m mesh improves the accuracy of the forward computations within RRI and results in a large difference in the resulting inversion image.

Figure 23 shows the results of RRI inversion for the 5×5 meter tunnel at 50 meters depth shown in Figure 10. This case corresponds to a depth-to-size ratio of 10. The inversion mesh is identical to that used in the previous case. However, the horizontal sampling density at the surface in the region between -20 m to 20 m has been increased from every 5.0 m to every 2.5 m. The increased sampling frequency produced an RRI image superior to the previous depth-to-ratio case. A comprehensive study of the tradeoffs between mesh resolution, horizontal sampling distance, accuracy and computational speed is in progress.

The results in Figure 23 show that, in the noise-free case and in a uniform background, starting with a forward simulation of a tunnel with a depth-to-size ratio of 10, RRI will produce a discernible image of the tunnel. To achieve this, it was first necessary to ensure that in the initial forward simulation, numerical errors due to meshing were kept small

(below 0.1%) compared to tunnel induced field perturbations at the surface of the earth model (on the order of 0.2 to 1%). Second, it is also necessary that the RRI inversion mesh be set fine enough to do accurate forward calculations for the objects of interest. Third, the spatial sampling density at the surface must be high enough (at least every 5 m) to accommodate expected variations of the field for the overall object size and depth. The scale of this sampling density should be a fraction of the depths of interest. Fourth, by making sure the forward data was accurate to 0.1%, it is possible to set the target RRI misfit (RMS error) to 0.1%. RRI ignores fluctuations less than the target misfit, so a 1% misfit would miss the majority of perturbations induced by a tunnel with a depth to size ratio of 10.

From the viewpoint of geophysical experiments that often have errors in field data on the order of 5%, objects that give rise to perturbations much smaller than 5% have not merited a great deal of attention. However, from the viewpoint of testing the limits of detectability, we see that underground structures with depth-to-size ratios of 10 are within the theoretical limit of detection even with current algorithms such as RRI.

While the tunnel in the forward models is two orders of magnitude more resistive than the background (10^4 Ohm-m tunnel vs. 100 Ohm-m background), the maximum resistivity contrast between the tunnel image and tunnel background in the inversion is much less. Further, this maximum contrast decreases with decreasing tunnel size. For the 15×15 m 50 m deep case, the tunnel image is only 19 percent more resistive than the background (119 Ohm-m maximum resistivity vs. 100 Ohm-m background). For the 10×10 m 50m deep case, the tunnel image is 10% more resistive than the background (110 Ohm-m maximum resistivity vs. 100 Ohm-m background). For the 5×5 m 50 m deep case, the tunnel image is 3% more resistive than the background. Hence, the smaller perturbations from smaller tunnels manifest themselves in RRI inversions as decreases in tunnel image contrast from the background. These low contrasts between the tunnel and the background are another consequence of the low resolution of the inversion algorithm.

The relatively poor resolution exhibited by the RRI inversions can be attributed to the way in which RRI computes its results, and not to the inherent resolution limits set by the physics of the problem. RRI determines a model structure, $m(x,z)$, for the conductivity as a function of position. To determine $m(x,z)$, RRI minimizes a functional that includes both a smoothness constraint Q and a measure of misfit χ^2 . The smoothness constraint Q favors models whose conductivity $m(x,z)$ has small second derivatives with respect to x and z . Hence, a smoothly varying $m(x,z)$ with small second derivatives is favored over a sharp $m(x,z)$ with large second derivatives - even if both models fit the input data equally well. As a result, RRI tends to produce smooth images. Although this approach has been useful for the targets encountered in geophysical exploration, man-made structures are smaller and have sharper contrasts, and the inherent bias of RRI toward the smoother output is not appropriate for this type of target.

It might be argued that the bias toward the smoother image ensures that any sharp features that are seen in the output inversion are genuinely present in the input data; this point is correct, but does not justify the approach taken by RRI. The implicit assumption in RRI's use of smoothness is that smooth conductivity profiles are *a priori* more likely than rapidly varying profiles, and this is clearly not justified by the characteristics of man-made structures. Even for use on geologic targets, we would argue that the tradeoff between resolution and reliability should be under the control of the operator, not fixed at the most conservative value.

3.2.2. RRI Inversion of Simulated Golden Zone Data

We discuss next the results of the simulations and RRI inversions for an underground structure with characteristics similar to those of the Golden Zone survey line 1 experimental data. In this case the tunnel depth to size ratio was 10, similar to the case presented in Figure 23. The tunnel dimensions were 2.5×3.0 m, the tunnel depth 28 m, and the half-space resistivity 200 Ohm-m. The forward simulation results for this case are shown in Figure 15; the inversion results are shown in Figure 24. The inversion mesh

was similar to the case shown in Figure 22. The horizontal sampling at the surface was uniform, every 5 m, for the inversion shown in the right side of Figure 24, and was increased to every 2.5 m between -20 m and 20 m for the inversion shown on the left side.

The differences in the two inversion images can be explained in the following manner. When supplied data every 5 meters on a mesh that is spaced every 2.5 meters, RRI interpolates between the soundings. However, on the same mesh, but with soundings every 2.5 meters in the region above the tunnel, interpolation is not needed above the tunnel. The result on the final RRI model is that the region of highest conductivity contrast from the background is twice as wide as the uniformly sampled case. The strongest horizontal variation in field on the surface occurs in a neighborhood directly above the center of the tunnel. Hence, this is the region where interpolation is the least desirable. In short, interpolation of sounding data near the center of the tunnel is causing RRI to lose too much information about the slopes of the field in this region, resulting in a poorer image.

3.2.3. Effect of Surface Layers on Tunnel Detection

Consider next RRI inversions of tunnels in half-spaces with conducting surface layers. The left image in Figure 25 shows the result of inverting the forward data in Figure 16. The meshing and uniform sampling density, and the image intensity scale, are the same as in Figure 24. The tunnel, the intensity peak at 205 Ohm-m at a depth between 50 m and 70 m, is barely visible.

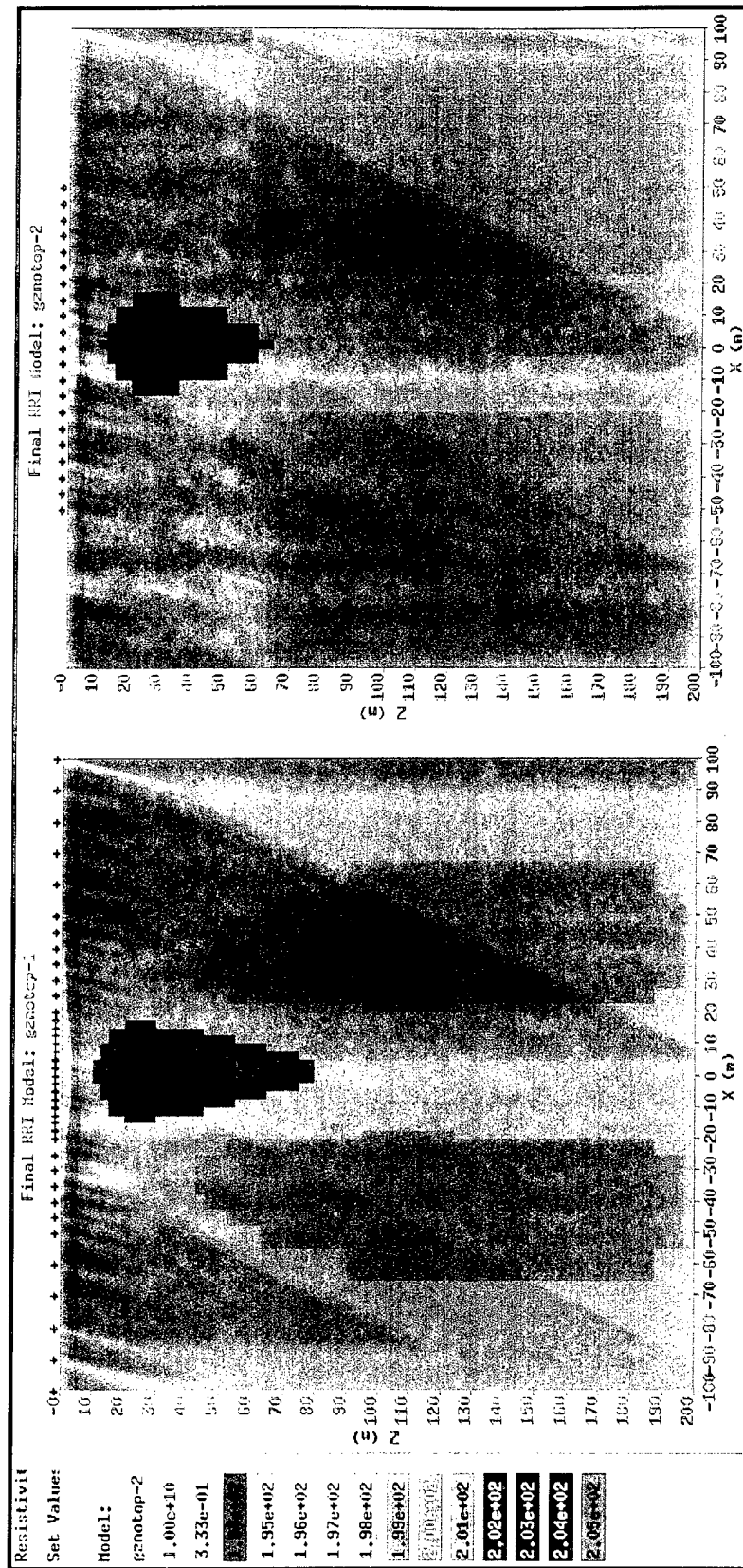


Figure 24. Effects of Sampling Density on RRI Inversion. Inversion of Data from Figure 15; Sampling Points are Shown at the Surface.

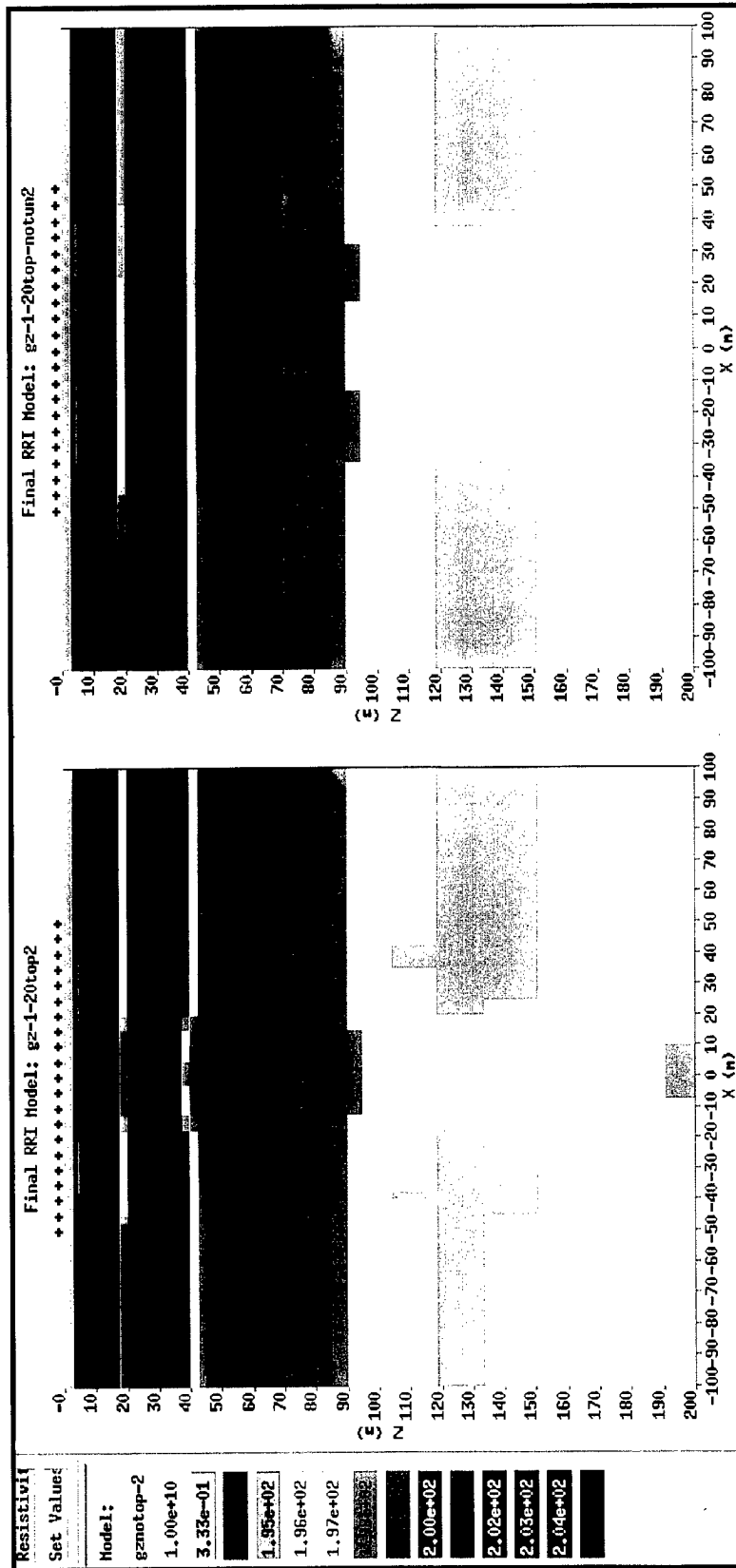


Figure 25. Effect of Conductive Layer on RRI Inversion Result. Inversions of Data from Figure 16 With (left) and Without (right) Tunnel.

The main problem here is that the surface layer is an order of magnitude more conductive than the background and therefore introduces a second contrast scale into the problem. On the other hand, RRI shows the smaller tunnels as smoothed regions differing by only a few percent from the background. Once RRI is given the large conductivity contrast due to the surface layer, it does not perform well for effects on a much smaller conductivity contrast scale. To highlight the multiple scaling problem, we also show the inversion for the case without a tunnel but with the same conducting surface layer and background conductivity as in the previous case. The result is shown in the right image in Figure 25. In this inversion, the image should be uniform in x . This is not the case. Rather, we see banding of what should be a uniform background below the conducting layer. For the case of uniform half space with a tunnel but no top conducting layer, such banding does not occur. Furthermore, we even see two perturbations that could be interpreted as structures (at 25 m, and -25 m, and both at a depth of 60 m) even though there was no structure in this forward simulation.

The above discussion shows that the second conductivity contrast scale introduced by the presence of a conducting surface layer can mask the relatively small perturbations induced by the tunnel. To correct for this effect, we can map the two-layer problem into an equivalent half-space. In the forward simulation, the equivalent conductivity would be a weighted average of the conductivity of the top layer, its thickness, and the rest of the half-space conductivity and thickness. In the inverse problem, one could constrain the large scale structure to be a uniform half-space. Such a procedure would result in poor depth estimates, but would remove the large conductivity difference from the inversion problem. Once the tunnel is found, it is possible to compute the background conductivity more accurately in order to estimate the tunnel's depth.

4. Experiments

A major part of this effort is the verification of theoretical and computational studies of imaging performance by field experiments. Two experiments have been conducted to date: the first at the Superconducting Supercollider site near Waxahatchee, Texas, and the second at the Golden Zone mine near Cantwell, Alaska. A detailed description of the experimental equipment and procedures is given in this section, followed by an analysis of the results obtained in each of the two experiments.

4.1. Equipment and Measurement Procedures

A complete ELF/VLF measurement system, including a transmitter, sensors, and data recorder, was assembled for the purpose of acquiring experimental data under this contract. The system was optimized for making magnetotelluric measurements in the VLF frequency range, which is the optimum frequency range for most man-made underground targets. Each of the major components is described in detail in the sections below.

4.1.1. Transmitter

The local source transmitter was designed and built by APTI, and designed to provide VLF signals to supplement natural background noise. The system is very compact when disassembled, and can be set up or taken down in approximately 30 minutes. It is composed of a pair of triangular vertical loops, supported by a central fiberglass mast 5 meters in height. Each of the two perpendicular loops is 14 meters across at the base, and contains 3 turns, for a total effective area per loop of 105 square meters.

The two loops are driven by a battery powered two-channel amplifier with a peak output voltage of 9.0 Volts; since the DC resistance of each loop is 2.9 Ohms, the loop current at low frequencies is 3.1 Amps, resulting in a total moment of 325 A-m^2 for each of the two

loops, and a total moment of 650 A-m^2 . The inductance of each loop is approximately 0.3 milliHenries, so at frequencies above 1.5 kHz, the loop current decreases; at the highest operating frequency of 42 kHz, the loop current has decreased to 0.11 Amps, reducing the total moment to 23 A-m^2 . Since the power supplied by the transmitter is needed most in the region from 1 kHz to 3 kHz where little natural noise is present, the reduction in moment with frequency is not normally significant.

However, transmitter enhancements planned for the next year include the addition of a larger driver amplifier capable of operation into loads as small as 1 Ohm, and a meter for real-time current monitoring. This will allow the operator to adjust the current level to maintain a more nearly constant moment if desired. In addition, to allow operation over very resistive ground where the highest transmitter frequencies are most important, a single-turn loop assembly will be fabricated. This would reduce the inductance to 0.033 mH, and raise the frequency at which moment falloff begins to 14 kHz. In conjunction with the larger driver amplifier, this configuration could provide higher moments at all frequencies, and much higher moments at the upper end of the frequency range, at the expense of higher power consumption.

Input to the driver amplifier is provided by a manually controlled function generator capable of producing either square or sine wave signals of adjustable amplitude at frequencies from 10 Hz to 80 kHz. In normal operation, sine waves at the 20 frequencies shown in Table 1, starting at 800 Hz and ending at 42 kHz, are used.

Table 1. Standard local source operating frequencies.

Frequency Designation	Frequency (kHz)
A	0.8
B	1.0
C	1.2
D	1.5
E	2.0
F	2.8
G	3.2
H	4.2
I	5.0
J	6.4
K	7.5
L	8.0
M	10.0
N	12.0
O	15.0
P	18.0
Q	20.0
R	28.0
S	32.0
T	42.0

Additional transmitter improvements planned for the next year include the ability to set transmitter frequencies remotely, to allow the recorder operator to control the transmitter and to allow computer control of both the transmitter and the recorder. This would eliminate the possibility of operator error in frequency selection and transmitter/recorder synchronization.

4.1.2. Sensors

The sensors used to acquire experimental data are grouped into three sensor stations. Each station has two electric field and three magnetic field sensors, giving it the capability to measure five of the six electromagnetic field components simultaneously. The components of each sensor station are described in the sections below.

4.1.2.1. Electric Field Sensors

The electric field sensors used to acquire all experimental data are models BF-16 or BF-25, manufactured by ElectroMagnetic Instruments. The BF-16 and BF-25 models are identical except for the length of the cables connecting them to the analog front end amplifier. Both models consist of a pair of stainless steel electrodes approximately 10 centimeters in length, and a cable containing a built-in preamplifier. The measured frequency response of the electrode and preamplifier is shown in Figure 26, and the manufacturer's specified noise spectrum is shown in Figure 27.

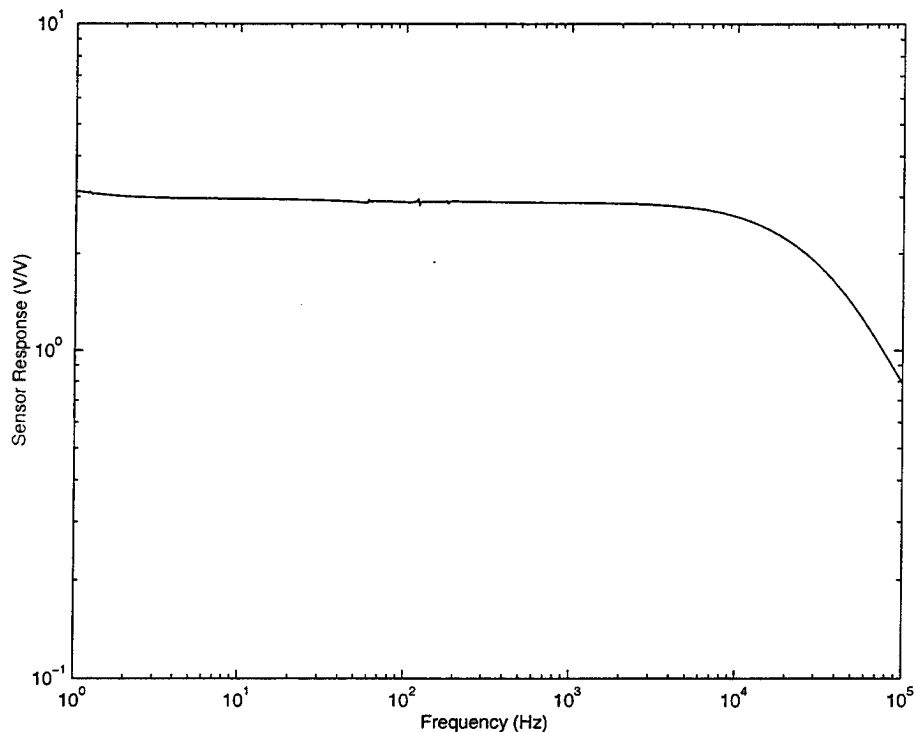


Figure 26. Electric Field Sensor Frequency Response

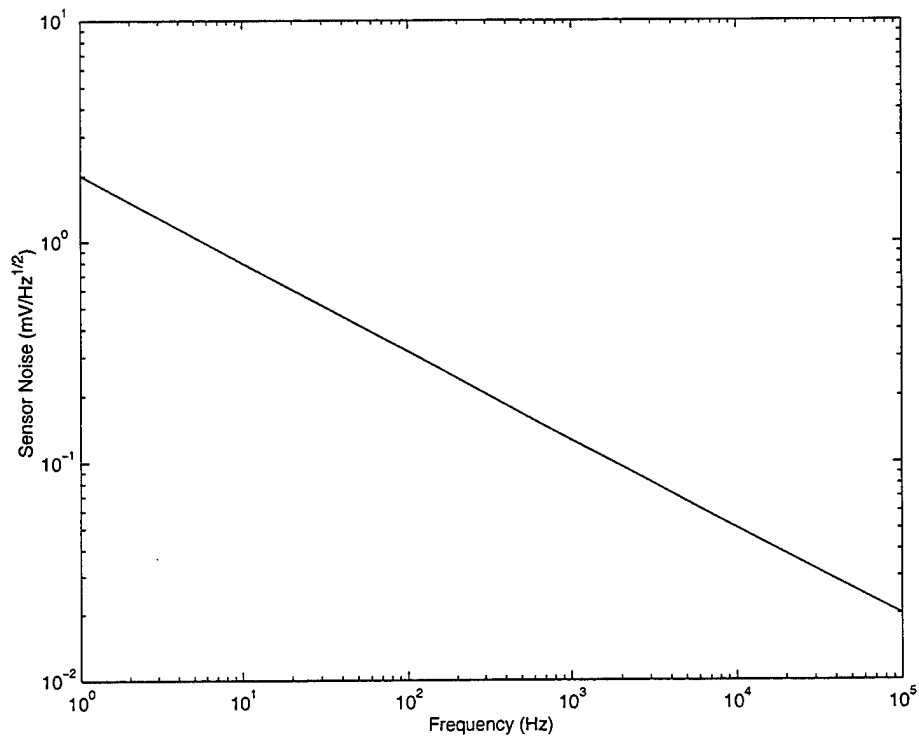


Figure 27. Specified Electric Field Sensor Noise Spectrum

Sensing the electric field in a single direction requires a pair of electrodes. Both members of the pair are driven into the ground a specified distance apart, and the voltage difference is measured; dividing this voltage by the known separation yields the electric field. The electric field sensors for adjacent stations are positioned so that the measurements are contiguous; this reduces the possibility of spatial aliasing. Normal experimental procedure is to space the stations 5 meters apart; although a wider spacing produces a larger signal for the same electric field, it also reduces the spatial resolution of the resulting data. To determine the effect of increasing separation on resolution, one data set has been taken at 10 meter spacing, as will be described below.

4.1.2.2. Magnetic Field Sensors

The magnetic field sensors used are ElectroMagnetic Instruments model BF-IM, which are essentially identical to the BF-6. The sensors are induction coil magnetometers 5 centimeters in diameter and 80 centimeters in length. They have a mu-metal core and an

integral preamplifier with magnetic feedback for flat response over a broad frequency range. The specified frequency response and noise spectrum of these sensors are shown in Figures 28 and 29. An additional pair of BF-6-HF sensors, also from ElectroMagnetic Instruments, are used as a remote reference.

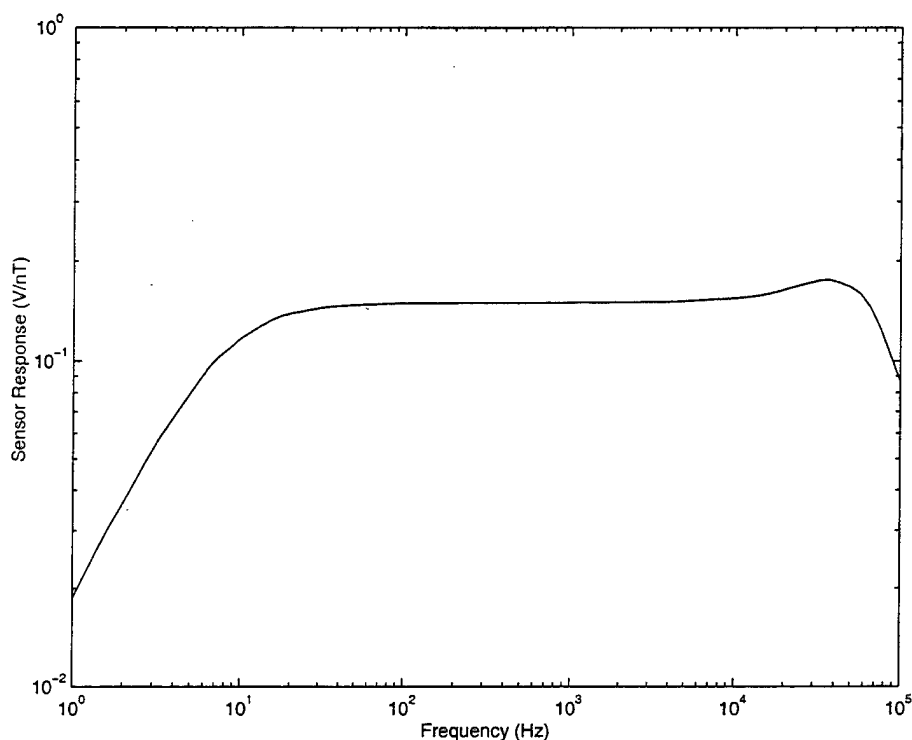


Figure 28. Magnetic Field Sensor Frequency Response

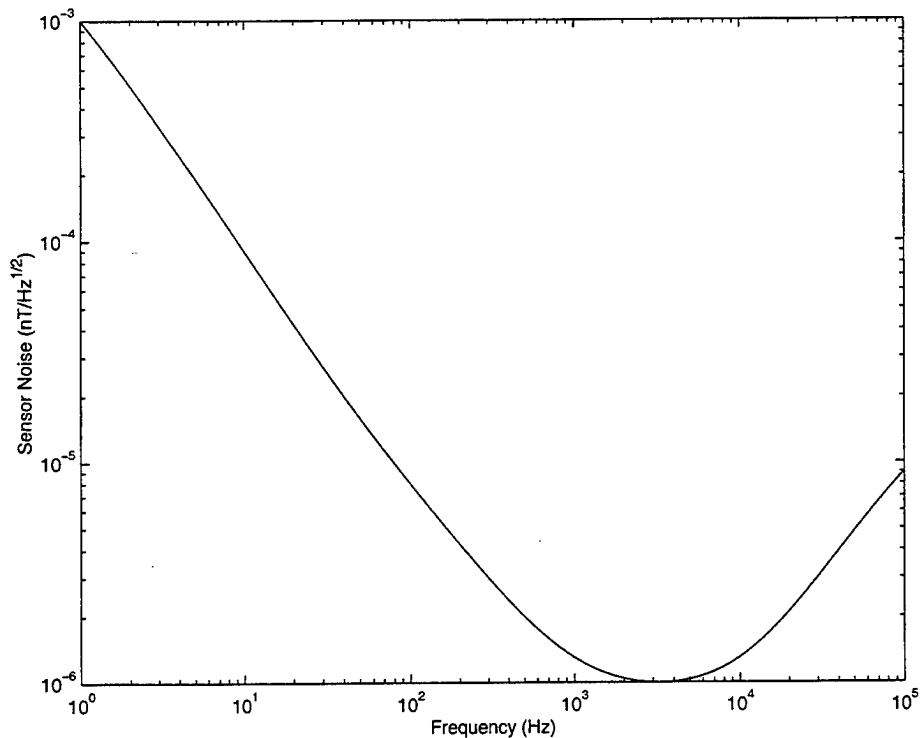


Figure 29. Specified Magnetic Field Sensor Noise Spectrum

Each sensor station includes three magnetic field sensors, allowing simultaneous measurements of the magnetic field in all three axes. To date, all experimental data has included only the horizontal electric and magnetic field components, principally because of the additional setup time required for vertical magnetic measurements. Except in still conditions, measurement of the vertical magnetic field requires burying the vertical magnetic sensor to prevent wind-induced vibration. This slows the process of station setup significantly. In addition, simulation results suggest that the addition of a vertical magnetic field measurement is most helpful on highly conductive targets; since all of the targets examined to date have been resistive, it is expected that the absence of a vertical magnetic measurement has not significantly reduced imaging performance. Experiments on conductive targets, including vertical magnetic field measurements, are planned for the next year.

4.1.2.3. Analog Front End Amplifier

Both the electric and magnetic field sensor outputs are passed through the analog front end amplifier before being sent to the data recorder. The principal purpose of the analog front end, also produced by Electromagnetic Instruments, is to provide additional amplification and filtering of power line signals and their harmonics. The electric field channels in the analog front end have an adjustable gain from 10 to 3200, the magnetic field channels from 1 to 800. All five channels also contain switchable highpass, lowpass, and power line filters; in normal operation, the filters are set to provide flat response and filtering of 60, 120 and 180 Hz power line signals. The measured response of an electric field channel in this configuration is shown in Figure 30.

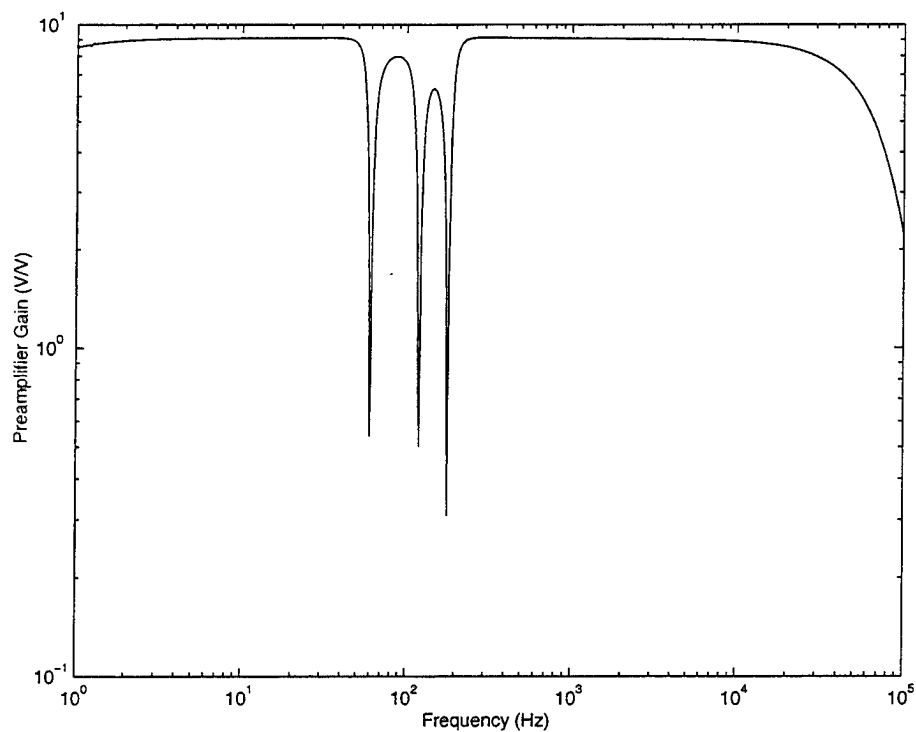


Figure 30. Analog Front End Frequency Response

4.1.2.4. Data Recorder

Signals from each of the three stations, as well as the two remote magnetic reference channels, are recorded by a Storeplex Delta digital data recorder manufactured by Racal Recorders. By recording all of the time series data, rather than just spectra, it is possible to examine the recorded data in detail and process it with several different techniques to compare the results. The recorder is equipped with 20 analog input channels, each with a 16-bit sigma-delta analog-to-digital converter capable of operating at a sampling rate of up to 100 kHz. The sigma-delta converters used in this system contain internal digital decimators that reduce an internal 6.4 megahertz low resolution output sample stream to a higher resolution 100 kHz output sample rate, while applying a linear phase digital antialiasing filter with ± 0.1 dB ripple from 0 to 45.5 kHz and greater than 90 dB of stopband attenuation. A significant advantage of sigma-delta converters is that the digital antialiasing filter eliminates the need for all but a simple second order analog filter at the recorder input.

The recorder is capable of recording 14 channels of 100 kHz sampled data (two electric and two magnetic channels for each of the three sensor stations, and two remote reference channels) for up to 60 minutes on a single ST-160 S-VHS video tape. When three additional vertical channels are added, the maximum recording time is reduced to 30 minutes at a 100 kHz sampling rate. The recorder can also sample at 6.25, 12.5, 25, and 50 kHz when high frequency data is not required, with corresponding increases in the recording time. An additional advantage of the sigma-delta converters is that the digital antialiasing filters automatically adapt to changes in the sampling rate.

The dynamic range of a 16-bit sampling system is somewhat smaller than the specified dynamic range of the sensors, so care must be taken to match the analog front end gains to the signal amplitude so that quantization noise does not contribute to the noise floor of the overall data acquisition system. The ideal noise floor of a perfect 16-bit data acquisition system and the measured noise floor of the recorder are shown in Figure 31.

The ideal system has a dynamic range of 96 dB; the recorder delivers approximately 90 dB of dynamic range, a very good performance for a system sampling at the relatively high rate of 100 kHz.

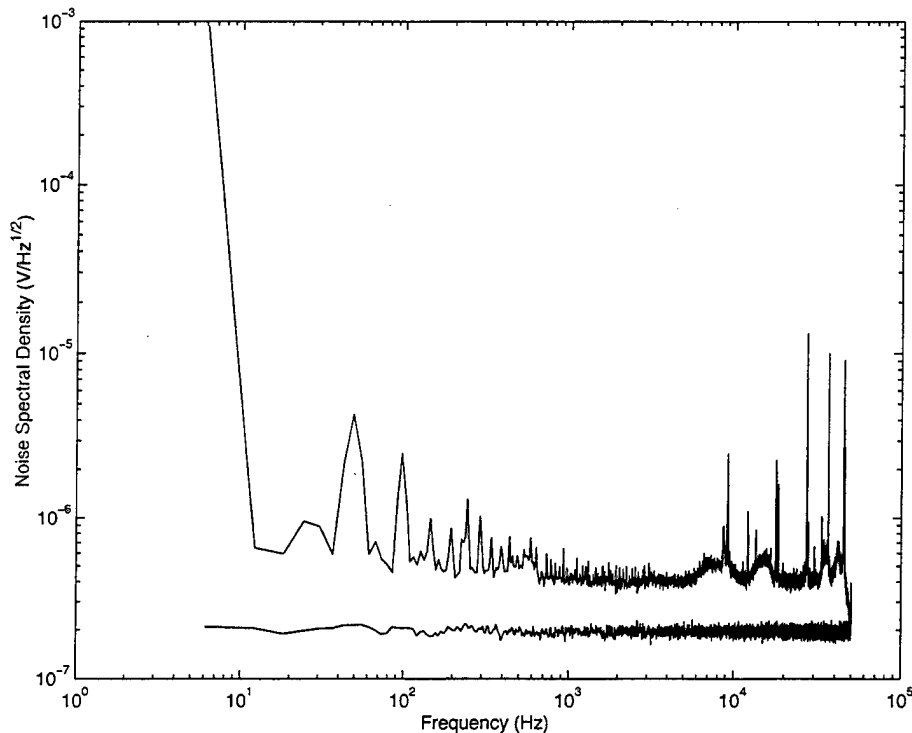


Figure 31. Ideal and Measured Recorder Noise Spectra.

A comparison of the noise contribution of the recorder and the intrinsic noise of a magnetic field sensor with a typical field spectrum is shown in Figure 32. The signal spectrum shown is recorded from one of the remote reference sensors, which do not pass through the analog front end and have no filtering of power line harmonics. This represents the worst case with respect to the dynamic range demands placed upon the data recorder. Note that in this case, both the recorder's quantization noise and the intrinsic noise of the sensor are well below the level of the recorded noise spectrum, indicating that the recorded signal is an accurate representation of the actual magnetic field level.

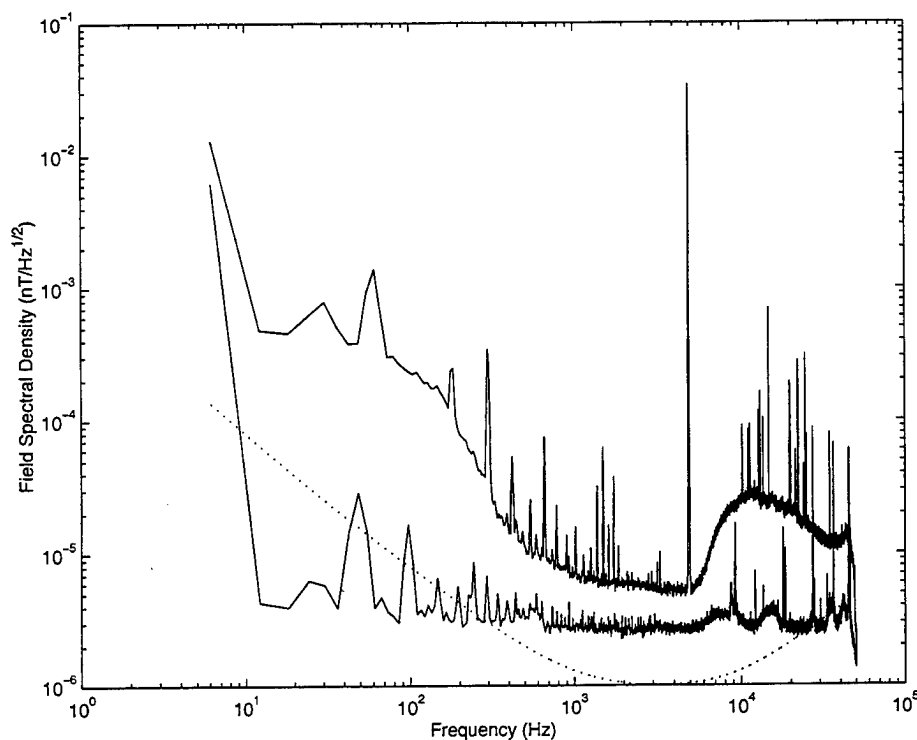


Figure 32. Comparison of Recorder and Sensor Noise with Typical Measured Signal

In examining the recorder and sensor noise spectra in Figure 32, we can see that the quantization noise of the recorder is somewhat higher than the intrinsic noise of the sensor in the region from 1 to 10 kHz; this would be the limiting factor in this frequency region if the natural magnetic signal level were very low. The sensor's internal noise is fixed by the design of the sensor, and cannot be adjusted, but if the signal level is low, it is possible to adjust the recorder gain so that the quantization noise is reduced. This procedure has been followed whenever possible.

The data recorder also automatically records date and time information accurate to 0.01 seconds for all recorded data. Before each recording session, the recorder clock is manually synchronized to the UTC time obtained from a handheld GPS receiver, ensuring that the recorded time is accurate to approximately ± 0.1 seconds. If higher accuracy is needed in the future, the recorder can also accept an IRIG-B timecode input that can be produced by a portable GPS time standard, allowing the recorded time to be matched to UTC to within the 10 millisecond resolution of the recorder clock.

4.1.2.5. Data Transfer

The data recorder includes a SCSI-2 interface to allow direct transfer of the recorded data to a computer for analysis. The data are transferred in 16-bit digital form under the control of data transfer software provided by the manufacturer. During the course of processing experimental data, it was discovered that the data received by the computer were corrupted by occasional errors. These errors, although infrequent, were sufficient to corrupt the spectra and make them unusable for imaging. In order to obtain uncorrupted spectra, it was necessary to repeat the data transfer process.

In examining this problem, it was determined that the fault lay with the data transfer software. The errors appearing in the outputs were not flaws in the data recording tape, because they were not replicated when a second transfer of the same section of tape was made. To rule out a hardware flaw, an identical data recorder was obtained and tested; the results were similar using both recorders. Different computers and SCSI controllers were also tested, with similar results. The only common element was the manufacturer-provided data transfer software. A preliminary version of the next software revision was obtained from the manufacturer; this version reduced but did not eliminate the data transfer errors.

Although the errors could be corrected by repeating the data transfer process, this problem made it necessary to manually examine the output of each data transfer to determine which were correct and which should be repeated. Because thousands of spectra are computed for each line of sensor data, the process of manual examination greatly slowed the analysis of experimental results.

Since this problem has had a serious impact on the efficiency of the analysis process, a permanent solution has been developed. A high-speed digital interface that bypasses the SCSI subsystem and does not require use of the manufacturer's software has been ordered

and is currently under test. This hardware solution should solve the transfer error problem and remove the need for manual examination of spectra. The new hardware is expected to be delivered before the start of the next field experiment and will be utilized in all future processing.

4.1.3. Standard Procedures

The normal data acquisition procedure is to place three stations at adjacent locations 5 meters apart, and record electric and magnetic field levels at these three stations simultaneously. A remote reference station, composed of two perpendicular magnetic field sensors, is also recorded at the same time as the station signals. The remote reference is typically placed 70-100 meters from the sensors, and is connected to the data recorder by a shielded coaxial cable.

To reduce the amount of wind-induced noise due to motion of the magnetic sensors, these sensors are stabilized with sandbags, or, under windy conditions, buried in trenches. Coupling of wind-induced vibration to the sensor outputs is less severe at the VLF frequencies of interest here than at ELF frequencies; nevertheless, it can be the principal contributor to the noise background if care is not taken to stabilize the sensors.

If the ground conditions are dry, the electrodes used for electric field measurements are wet with water to reduce the contact resistance. As in the case of wind-induced noise for the magnetic field sensors, noise caused by the contact resistance of the electrodes is less of a problem at VLF than at lower frequencies. In both of the experiments described below, the ground surface was sufficiently wet that additional moisture was not needed.

Although the sensor station configurations are identical, the data recording procedure varies depending on whether a local source or an ionospheric source is used. The standard procedures for each of these are described below.

4.1.3.1. Local Source

When the transmitter described above is used as a local source, twenty minutes of data are recorded at each station. One minute of data is recorded at each of the transmitter frequencies shown in Table 1. To allow accurate identification of the frequencies using the time data recorded automatically by the recorder, the transmitter frequency schedule is synchronized to the recorder clock, so that all frequency transitions occur between :50 and :00 seconds on the recorder clock. This permits the transmitter frequencies corresponding to each minute of recorded data to be easily identified, and ensures that at least 50 seconds of usable data are obtained at each frequency.

The range of 800 Hz to 42 kHz covered by the standard local source frequency schedule is appropriate for a wide range of ground conductivities, and it has not been found necessary to modify this schedule for any of the experiments performed to date. The remainder of the measurement system limits the useful frequency range to below 50 kHz; this limit is set both by the rising noise level of the magnetic field sensors and the 45.5 kHz cutoff frequency of the recorder. As described in the transmitter section above, some source modifications are possible to increase the transmitted power at high frequencies; this would increase the available power at frequencies up to the 45.5 kHz recorder cutoff.

At frequencies below 1.5 kHz, the output of the transmitter is constant with frequency down to the lower frequency limit of 10 Hz. The major difficulty in employing the local source at low frequencies is placing it sufficiently far from the measurement site so that its signal approximates that of a distant source. In order to meet this requirement, the transmitter must be positioned at least 3 skin depths (in the ground at the experiment location) away from the measurement location. As the conductivity of the ground drops, this distance becomes larger, and since the field from the transmitter falls off as $1/r^3$, it becomes difficult to obtain sufficient signal from the transmitter at the distances that must be employed in resistive grounds.

Although these factors could limit the utility of the local source in regions of very high or very low ground conductivity, little difficulty has been experienced with these effects in the experiments conducted to date. In some cases, the experimental data show that the 3 skin depth minimum distance has not been met for the lower end of the transmitter frequency range. This is not so much a problem of transmitter design as of logistics; the transmitter location is also affected by practical considerations such as ease of operator access. The modifications to increase transmitter power described in the transmitter section above should give increased flexibility in selecting the transmitter location.

4.1.3.2. Ionospheric Source

When an ionospheric source is used, the signals from the source are typically much weaker than those from a local transmitter. To accommodate the reduced signal level, the amount of time spent at each frequency is doubled to two minutes, and a total of forty minutes of data are recorded at each sensor location. Synchronization of the recorder clock with the transmitted signal is made possible by setting the recorder clock using a GPS derived time signal as described above. The ionospheric heater's transmission schedule is also accurately synchronized to GPS time, so the location of the frequency transitions of the ionospheric source can be identified with an error of much less than a second. As with the local source, this allows easy identification of the transmitter frequency using time data recorded along with the measured signals.

The frequency range used for the ionospheric source is selected for each experimental site on the basis of conductivity estimates derived from local source measurements. The ionospheric source does not suffer from the low frequency limitations that the local transmitter does, since it is always at a large distance from the measurement site. At higher frequencies, an ionospheric source has approximately constant signal output (for fixed ionospheric conditions) up to the point at which it can no longer raise the ionospheric electron temperature fast enough to keep pace with the modulating waveform. This limit is determined by the RF power density achieved at the heating

altitude by the ionospheric source, and depends on the heating frequency, gain and transmitter power of the heating facility. For the HAARP DP facility at 330 kW RF power, it is approximately 5 kHz, for the HIPAS facility, approximately 8 kHz, and for the completed HAARP facility at 3.6 MW, it is estimated to be 20 - 40 kHz.

4.1.3.3. Surveying

To provide reliable data on the location of the sensor stations relative to the target, the locations are surveyed using a total station instrument. Survey data are adjusted to produce accurate position estimates and ensure consistency of the measured angles and distances; the typical residual error (the estimated standard deviation of the adjusted points) is less than 0.05 meters. In many cases, the target itself is not accessible, so data must be obtained on the location of the target relative to surface landmarks that can be surveyed. In this case, the accuracy of location estimates also depends on the accuracy of the target location data.

4.2. SSC Experiment

Two trips to perform experiments at the Superconducting Supercollider site near Waxahatchee, Texas were made on March 10-14 and April 7-11, 1997. The original intent was to acquire all the necessary data in one trip; however, because of poor weather, very little data was acquired during the first visit in March. On the second trip, it was decided to repeat the acquisition of the data acquired on the first trip to ensure that all the data were gathered under similar conditions.

4.2.1. Description of Experiment

The target for this experiment was the main ring of the Superconducting Supercollider at a location just north of the building complex at station N-15. At this location, the main ring is 5.6 meters in diameter and approximately 65 meters beneath the surface. This section of the tunnel is lined with reinforced concrete in prefabricated sections. Because pumping of water from the tunnel ceased more than two years before this experiment, it is assumed that the tunnel is partially or completely filled with groundwater.

Data were taken along two lines of length 105 meters, as shown in Figure 33. Line 1 crossed the tunnel approximately perpendicular to the tunnel centerline; it was surveyed both at the usual 5 meter station spacing and at a spacing of 10 meters to determine the effects of station spacing on resolution. The second line crossed the tunnel at approximately a 45° angle to the tunnel centerline and was taken to examine the effects of crossing angle on resolution of two-dimensional targets.

The line locations were surveyed with respect to the intersections of Loop Road with Hoyt Road, and Hoyt Road with FM 1446, as well as the corners of the MTL building and the surface mounds associated with the personnel, utility, and magnet delivery shafts. The end points of a USGS survey conducted during the first visit were also surveyed and are shown on Figure 33. These locations were correlated with data obtained later to accurately locate the tunnel; it is estimated that the horizontal location of the tunnel is known to within 1 meter, and the depth to within 5 meters.

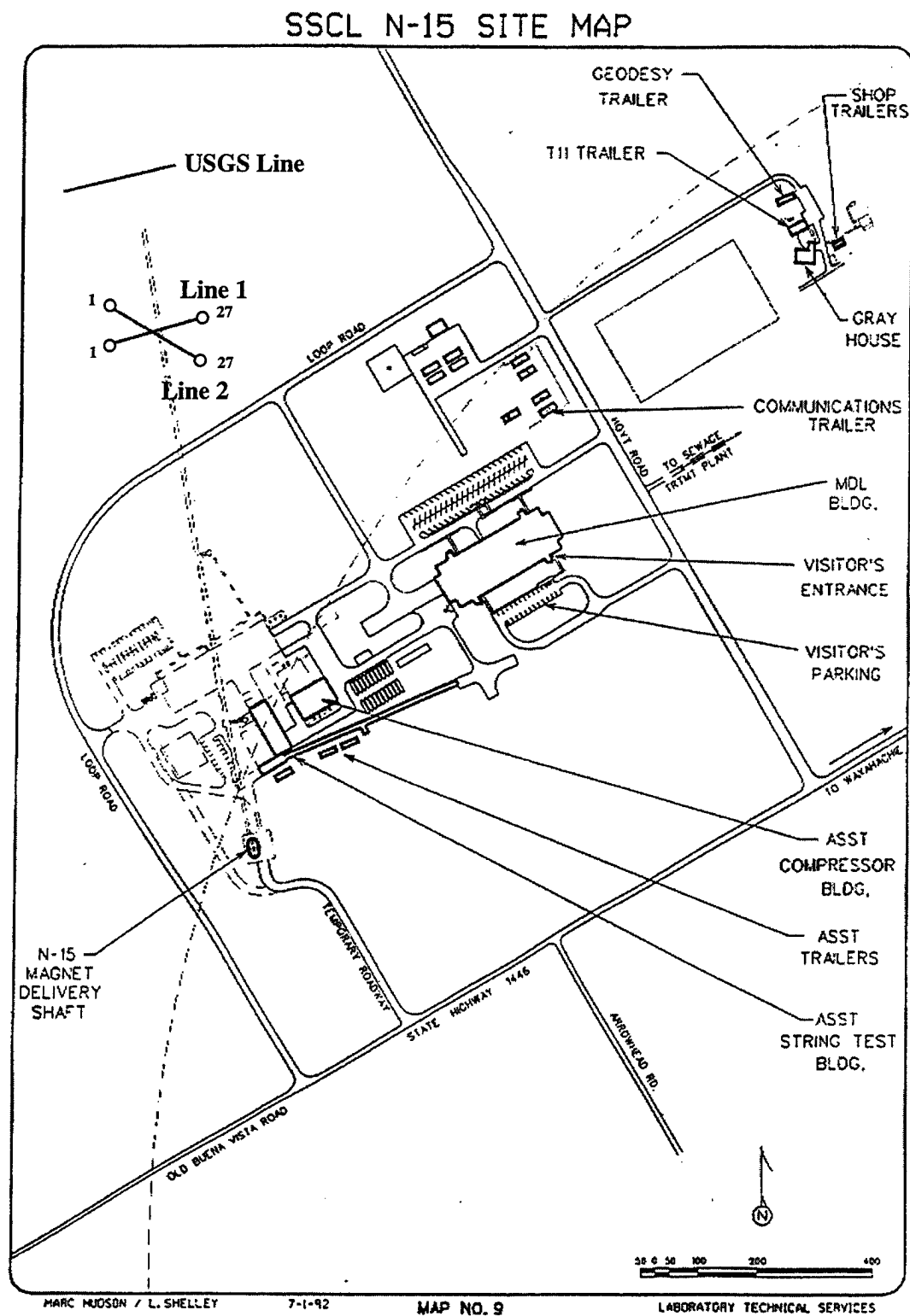


Figure 33. Site Map of the SSC Experiment.

4.2.2. Analysis of Results

As the data from the survey were analyzed, it became apparent that one of the three sensor stations exhibited a systematic gain difference that was consistent throughout the experiment. Although examination of the time series data showed that the data were valid, the response of the station was different from the other two stations by a significant amount. The size of the difference and the fact that it appeared at every location where that sensor station was employed ruled out the possibility that the variation resulted from genuine conductivity variations in the ground.

In order to correct for this error, the data from the station in question were normalized so that their average apparent resistivity along the entire survey line was similar to the other two stations. This reduced the variation sufficiently to allow the data to be analyzed, but did not completely eliminate the problem. Extensive calibration tests of the sensors did not detect any malfunction in the sensors or the analog front end; it appears that the difference must have resulted from a systematic error in setting up the station or in programming its gain at each of the sensor positions.

Shown in Figure 34 is an inversion result obtained using the 5-meter spacing data from survey line 1. The true location of the tunnel is between stations 2 and 3, at a depth of approximately 65 meters. This result was a disappointment for a number of reasons, the principal one of course being that no identifiable response at the known location of the tunnel was observed. The residual effects of the partially corrected gain variation can be seen as vertical striations. The large resistive anomaly seen at stations 5-11 is similar to the expected signature of the tunnel, but this would require an error in position location of approximately 25 meters, which is extremely unlikely. It is more likely that this resistive anomaly is not the tunnel itself, but perhaps caused by a variation in groundwater flow due to the presence of the tunnel.

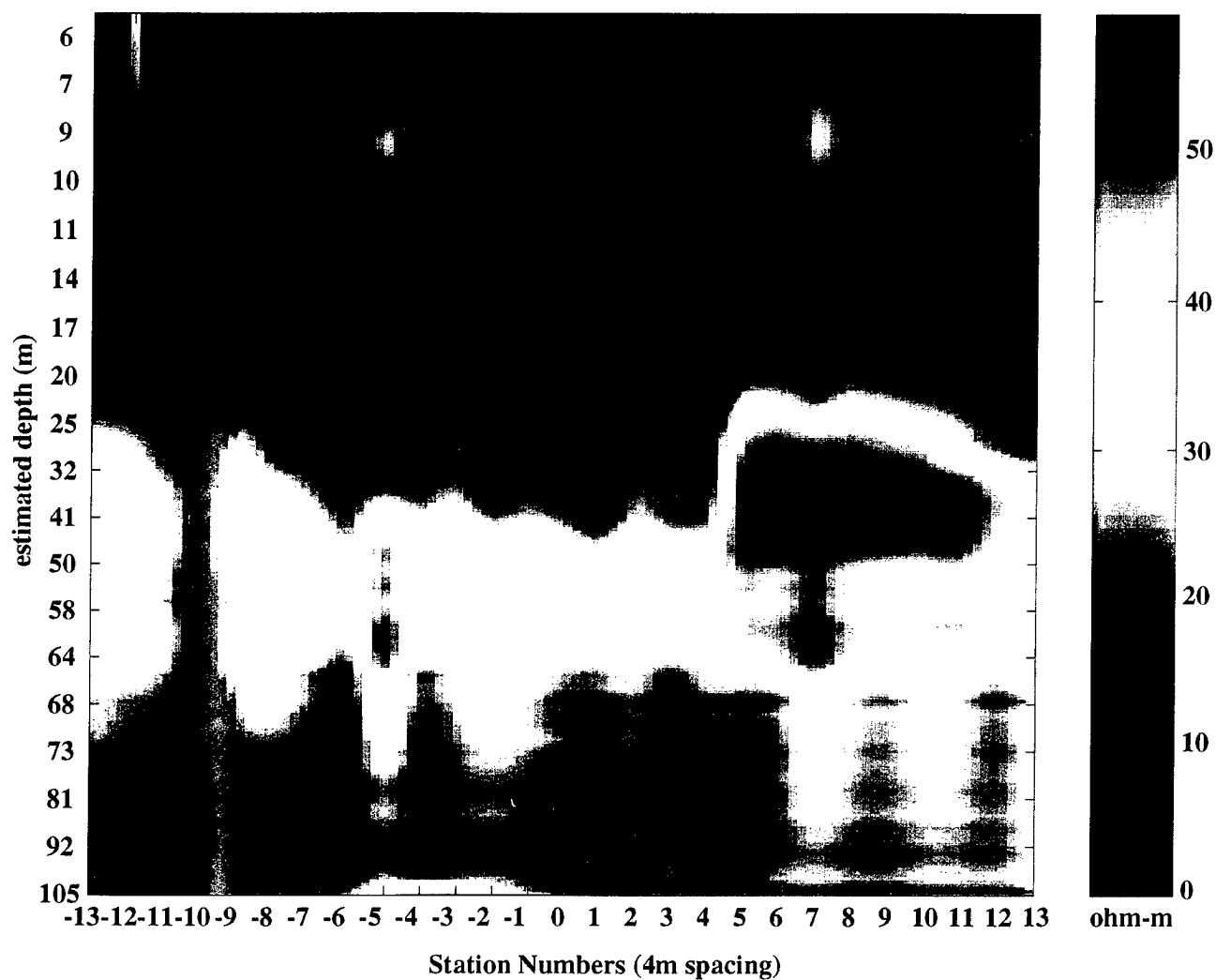


Figure 34. Resistivity Image for SSC Experiment using
Parameters $\kappa = .77$, $\lambda_v = .01$, $\lambda_h = 50$; $\% (77) = 24.0$.

The parameters which affect the performance of the imaging algorithm have been described in Section 2.2. The algorithm parameters used for this result were a minimum coherence threshold of $\kappa=.77$, a spectral regularization parameter of $\lambda_v=.01$, and horizontal Lagrange multiplier of $\lambda_h=50$. This coherence threshold delivered a percent over threshold of $\%(.77)=24$. This is an unusually small κ compared to what is usually employed, but was chosen to mitigate the effects of the gain variation discussed above. Both the spectral regularization parameter λ_v and the horizontal parameter λ_h are significantly smaller than usual.

During the analysis of the Golden Zone data described below, several modifications to the processing and inversion procedures were implemented. These changes resulted in significantly better performance on those data, and data from the SSC survey will be reprocessed using the modified procedures to determine whether better results can be achieved. Processing of the remaining lines from the SSC survey will also be completed using the updated procedures.

4.3. Golden Zone Experiment

A full experimental campaign, including use of the HAARP ionospheric source, was conducted at the Golden Zone mine near Cantwell, Alaska, on August 4-18, 1997. The details of this experiment and an analysis of the results are given in the sections below.

4.3.1. Description of Experiment

The Golden Zone is a gold mine whose initial workings date from the early part of this century; it was last extensively mined in the 1930s. Four levels of workings exist, at depths of approximately 100, 200, 325, and 500 feet from the top of the ore body. The depth below ground level varies depending on the location.

Of the four levels, the 325 foot level was the most recent, having been opened in 1983, and was the only level accessible for inspection. The tunnel is approximately 3.0 meters

in diameter, and contains two compressed air lines approximately 10 cm in diameter; over most of its length the roof of the tunnel has been lined with wire mesh. A typical interior view of the 325 foot level is shown in Figure 35.

A plan view of the Golden Zone experiment setup is shown in Figure 36. Data were taken along three lines; all three lines passed over the 325 foot level tunnel, at depths of 29 meters for survey line 1, 36 meters for survey line 2, and 48 meters for survey line 3. All three lines were surveyed using the local transmitter at the position shown, following the standard procedures described above. In addition, survey line 1 was surveyed on seven consecutive nights, 12 August – 18 August universal time (11 August – 17 August local time), using the HAARP facility as a transmitter.

The HAARP facility was 248 kilometers from the experimental site at a bearing of 110° true. On each night, the facility transmitted in X polarization at an RF power level of approximately 300–320 kW. The HF carrier was amplitude modulated with a modulation level of 90% by a sinusoidal signal at the desired VLF frequency. The modulation frequency schedule is shown in Table 2 below.



Figure 35. Golden Zone Mine Interior

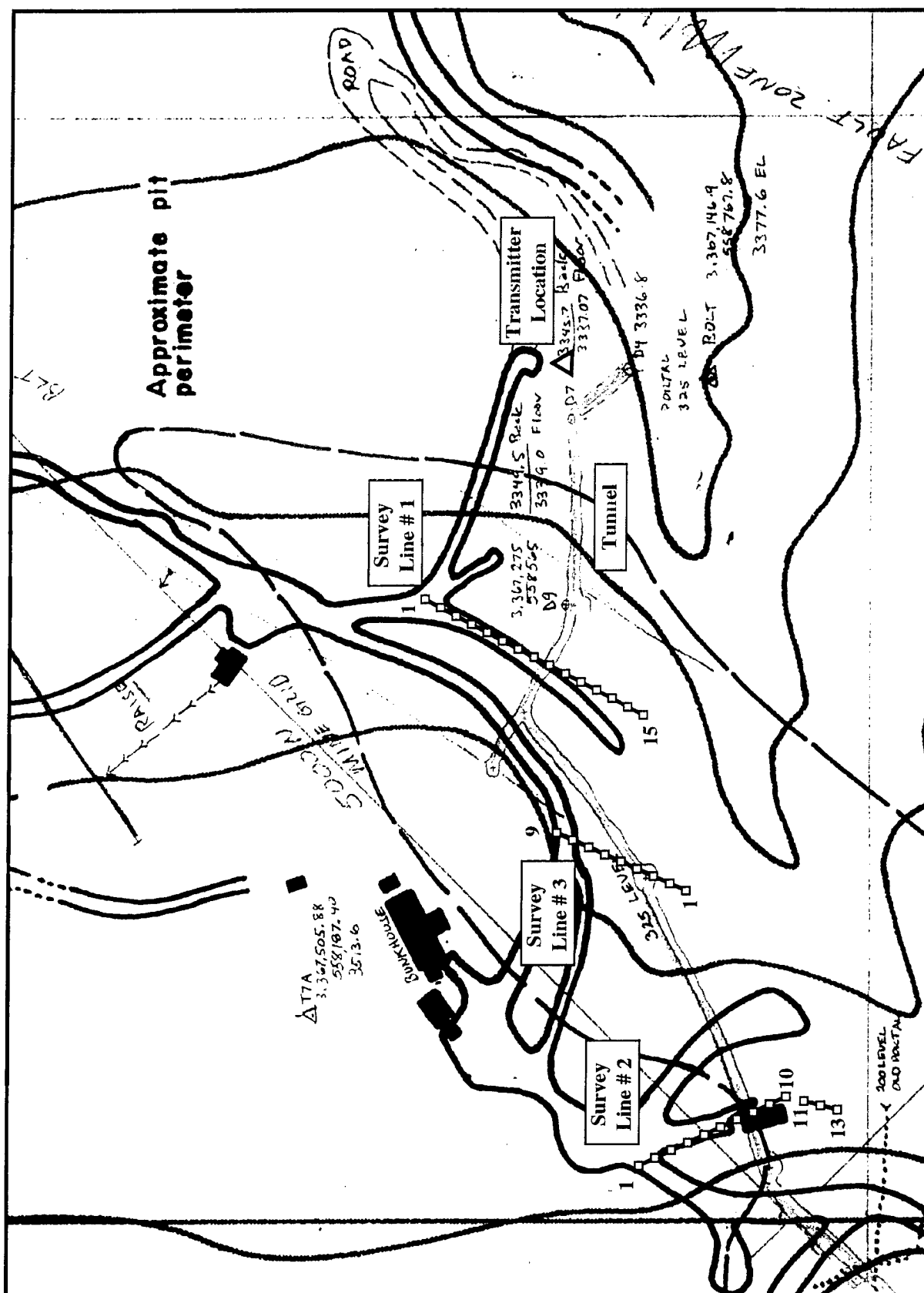


Figure 36: Golden Zone Mine Plan View.

Table 2. HAARP Modulation Frequency Schedule

Minutes After Start	Modulation Frequency (kHz)
:00 – :02	1.0
:02 – :04	1.1
:04 – :06	1.3
:06 – :08	1.4
:08 – :10	1.6
:10 – :12	1.8
:12 – :14	2.0
:14 – :16	2.3
:16 – :18	2.6
:18 – :20	3.0
:20 – :22	3.3
:22 – :24	3.8
:24 – :26	4.3
:26 – :28	4.8
:28 – :30	5.5
:30 – :32	6.1
:32 – :34	7.0
:34 – :36	7.8
:36 – :38	8.9
:38 – :40	10.0
:40 – :00	OFF

This schedule was repeated five times each night at one hour intervals. During each hour, data was collected at three locations on survey line 1, allowing all 15 stations on that survey line to be covered each night. The starting time for HAARP operation varied over the seven nights on which data were collected; the times for each night are shown in Table 3 below.

Table 3. HAARP Starting Times

Night 1	20:00 11 Aug 1997 ADT	04:00 12 Aug 1997 UT
Night 2	20:30 12 Aug 1997 ADT	04:30 13 Aug 1997 UT
Night 3	20:30 13 Aug 1997 ADT	04:30 14 Aug 1997 UT
Night 4	22:30 14 Aug 1997 ADT	06:30 15 Aug 1997 UT
Night 5	22:00 15 Aug 1997 ADT	06:00 16 Aug 1997 UT
Night 6	22:00 16 Aug 1997 ADT	06:00 17 Aug 1997 UT
Night 7	22:00 17 Aug 1997 ADT	06:00 18 Aug 1997 UT

Table 4. HAARP Carrier Frequencies and RF Powers

Time (UT)	Carrier Frequency (MHz)	RF Power (kW)
12 Aug 1997 (Night 1)		
04:00 – 04:40	3.200	340
05:00 – 05:40	3.200	340
06:00 – 06:40	3.200	330
07:00 – 07:40	3.200	320
08:00 – 08:40	3.200	320
13 Aug 1997 (Night 2)		
04:30 – 05:10	4.438	300
05:30 – 06:10	4.438	320
06:30 – 07:10	4.438	320
07:30 – 08:10	4.438	300
08:30 – 09:10	4.438	300
14 Aug 1997 (Night 3)		
04:30 – 05:10	4.438	300
05:30 – 06:10	4.438	300
06:30 – 07:10	4.438	300
07:30 – 08:10	4.438	300
08:30 – 09:10	4.438	300
15 Aug 1997 (Night 4)		
06:30 – 07:10	4.438	280
07:30 – 08:10	4.438	300
08:30 – 09:10	4.438	300
09:30 – 10:10	4.438	300
10:30 – 11:10	4.438	300
16 Aug 1997 (Night 5)		
06:00 – 06:40	4.438	320
07:00 – 07:40	4.438	320
08:00 – 08:40	4.438	320
09:00 – 09:40	4.438	320
10:00 – 10:40	4.438	300
17 Aug 1997 (Night 6)		
06:00 – 06:40	4.438	320
07:00 – 07:40	4.438	320
08:00 – 08:40	4.438	320
09:00 – 09:40	4.438	320
10:00 – 10:40	4.438	320
18 Aug 1997 (Night 7)		
06:00 – 06:40	4.438	320
07:00 – 07:40	4.438	320
08:00 – 08:40	4.438	320
09:00 – 09:40	4.438	320
10:00 – 10:40	4.438	320

There was a slight variation in the transmitted power level as the experiment progressed due to changes in the number of transmitters operational. In addition, the carrier frequency was different on the first night of operation. The complete schedule of carrier frequencies and RF power levels for each hour of transmission is shown in Table 4.

On 16 August (Night 5), difficulties with the transmitter control system at the HAARP facility caused some of the desired frequencies not to be transmitted. The scheduled start times for the five hours of operation were 06:00, 07:00, 08:00, 09:00, and 10:00 UT; the actual start times were 06:05, 07:25, 08:00, 09:00, and 10:10 UT. For the three hours that the actual start times were missed, the frequencies that would have been transmitted were skipped, so that the remaining frequencies were transmitted according to the schedule in Table 2.

During this experiment, the HAARP facility was operating at a very low power level; consequently, the signal received at the experiment site was relatively small. Because of difficulties encountered in transferring data from the data recorder, as discussed in Section 4.1.2.5, not all of the HAARP data recorded have been analyzed at this time. However, sections of the data spaced approximately one hour apart have been analyzed, and it is possible to give general estimates of the signal levels obtained.

The minimum signal level useful for imaging at the Golden Zone site would have been approximately 0.05 pT RMS; although the HAARP signal was often easily detectable in the recorded data, there were few instances when the signal reached 0.05 pT. Diagnostics available at the HAARP site indicated that ionospheric conditions for VLF generation ranged from moderate to poor over the period of the experiment. Unfortunately, no real time data from local receivers were available to the HAARP operator to allow selection of the optimum RF frequency, so it is impossible to know whether higher signal levels could have been achieved by heating at different frequencies.

The maximum signal obtained from the HAARP transmitter in the data records analyzed to date was approximately 0.1 pT RMS. This signal was obtained for a brief period at approximately 06:48 UT on 13 August, while HAARP was transmitting at a modulation frequency of 3 kHz. A field spectral density plot of this signal, computed from data taken at 06:48:00 to 06:50:00 UT, is shown in Figure 37. The origin of this signal is confirmed by the fact that the previous and following two minute data records show similar strong signals at 2.6 kHz and 3.3 kHz, respectively, the corresponding HAARP modulation frequencies for those times.

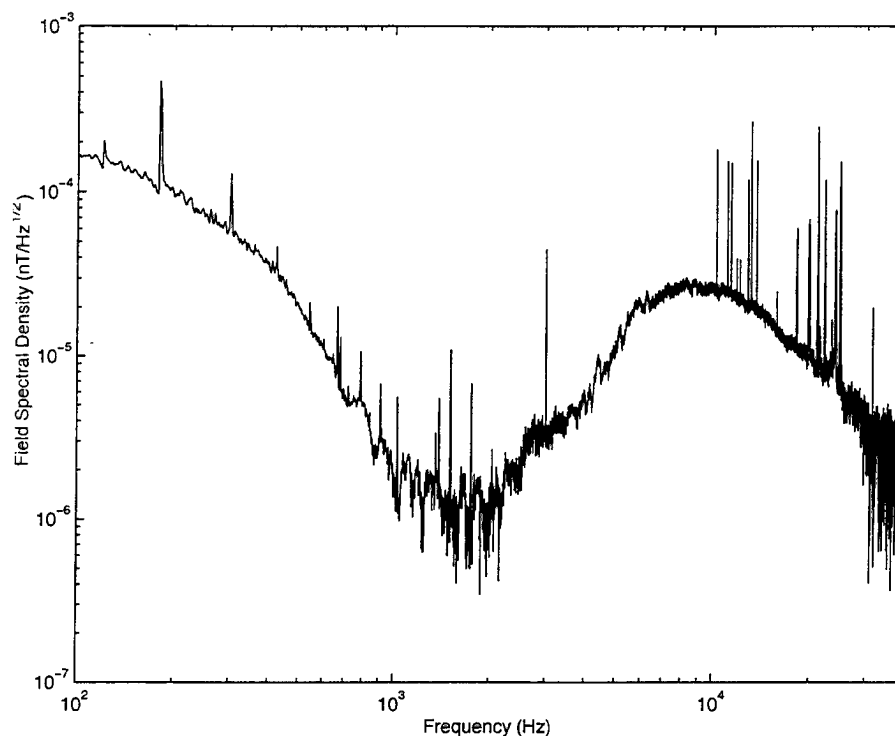


Figure 37. Field Spectrum Showing HAARP Signal at 3.0 kHz

In general, it appears that the signals obtained from HAARP were not sufficiently strong to be useful for imaging over most of the experimental period. For the facility at a power level of 320 kW to produce signals strong enough to be useful at the 250 kilometer distance of the experimental site, good to excellent ionospheric conditions would be required. The brief periods of strong signal obtained indicate that these conditions do occur, but it appears that during the late summer period they do not occur frequently. It is

unfortunate that the facility operators did not have real time diagnostics of the VLF signal level available to allow them to select an optimum heating frequency.

The signal level obtained from the HAARP facility operating at a heating frequency of 4.438 MHz appears to have smaller amplitude variation from night-to-night than has been previously observed in experiments using the HIPAS facility at a heating frequency of 2.85 MHz. Although this observation is based on small sets of data taken at different times and under different conditions, it is in accord with some previous theoretical analyses of heating. An experiment to test the relative efficiency and stability of heating at different RF frequencies could easily be conducted using the HAARP facility and a single set of VLF receiving coils. Because of the importance of signal level to the imaging mission, plans are underway to conduct such an experiment during the next year; this would provide quantitative data to determine how to optimize the ionospheric generation of VLF signals.

The HAARP facility is in the process of being upgraded to a RF power level of 960 kW; it is currently expected that the facility will be available for experiments at this power level in the Fall of 1998. The threefold increase in RF power level is expected to result in approximately a threefold increase in field levels (a factor of nine increase in radiated VLF power). Scaling the data observed at the Golden Zone to account for the increased power level, it appears that useful signals would have been observed as much as 50% of the time had the 960 kW facility been available for this experiment.

4.3.2. Analysis of Results

This section contains an analysis of data from Golden Zone survey line 1, taken using the local transmitter. Data from local transmitter measurements on survey lines 2 and 3, as well as from the seven nights of data collection using the HAARP source, are currently being analyzed.

One effect noted in the initial analysis of the survey line 1 data was that at the lowest source frequencies, the transmitter was too close to provide an approximation to a distant plane wave. Figure 36 shows that line 1 was the closest to the transmitter of all the lines; source proximity effects should be much smaller at the other locations. Analysis of the data showed that at line 1, the transmitter signal was usable only at frequencies of 6.4 kHz and above. All data at frequencies below this were obtained using natural background noise recorded concurrently with the higher transmitter frequencies to ensure that the plane wave assumption inherent in the inversion was obeyed.

In order to illustrate the factors affecting the output image, we will first examine several different images derived from the same input data set. We will begin by examining images from the survey line 1 local source data as key parameters of the algorithm are adjusted, to provide insight into the effects of these parameters. All detection, estimation and inversion algorithms have similar thresholds and parameters to adjust, and each parameter should have a distinctly different effect on the output. Here, we will concentrate on the three most important parameters discussed earlier in Section 2.2.3, namely:

- 1) The minimum coherence threshold, κ , which is used to screen less reliable input data from the inversion process;
- 2) The Lagrange multiplier, λ_v , which controls the degree of vertical spectral regularization of the input data; and,
- 3) The Lagrange multiplier, λ_h , which controls the degree of horizontal spatial regularization of the data filtered in Step 2.

These three parameters are the most important in defining the operating points of the inversion. Significant attention will be paid to how the κ threshold controls the solution output. The Lagrange multiplier for the spectral regularization will be examined with respect to its effect on the vertical smoothing. The Lagrange multiplier for the horizontal regularization will be given the least attention since it amounts to a conceptually simple adaptation of the widely used and well understood Bostick filtering method.

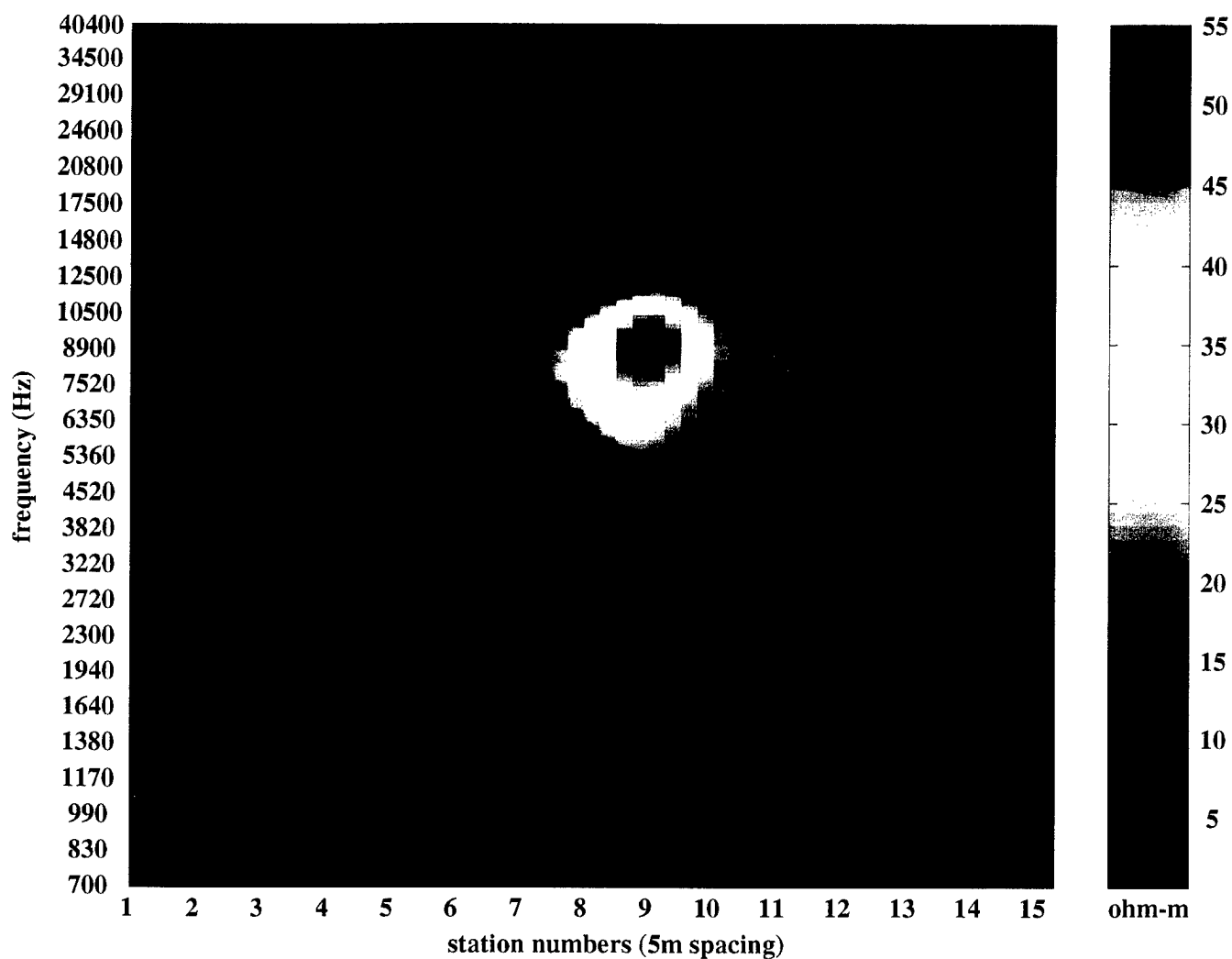


Figure 38. Complex Resistivity Magnitude Image using
Parameters $\kappa = .89$, $\lambda_v = .4$, $\lambda_h = 190$.

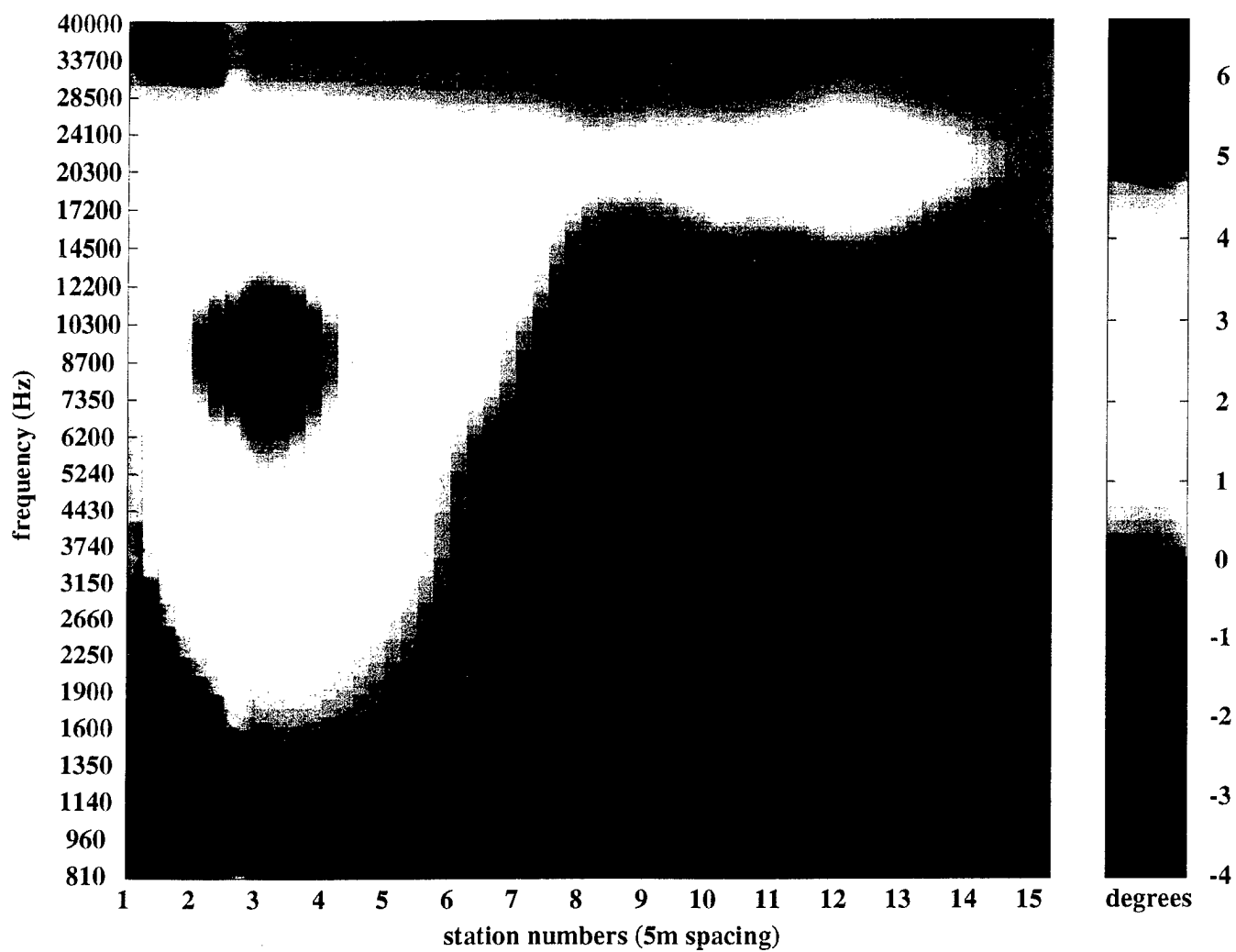


Figure 39. Complex Resistivity Phase Image using
Parameters $\kappa = .89$, $\lambda_v = .4$, $\lambda_h = 190$.

In all cases where we compare the effects of different parameter settings, we will plot the magnitude and phase of the complex resistivity ρ_c defined in Section 2.2.3, because the effects of the different parameter settings are most clearly visible in ρ_c . It is important to realize that the magnitude of ρ_c alone is not sufficient to determine whether a perturbation is conductive or resistive in nature; it is also necessary to examine its phase. Once the analysis is complete, we can plot an estimate of the actual ground resistivity as a function of depth taking into account both the magnitude and phase of ρ_c .

We turn first to the complex resistivity images shown in Figures 38 and 39. The magnitude image shows a distinct anomaly starting at a frequency of about 12 kHz located beneath stations 8 and 9. The peak of the anomaly occurs at a frequency of 9 kHz, corresponding to a depth of about 36 meters using the simple method outlined below to estimate the depth. These parameters compare well with the known location of the tunnel, which crosses the survey line between stations 8 and 9 at a distance of 0.8 meters from station 9, and with the known tunnel depth of 29 meters.

The image shown in Figure 38 was computed using a minimum coherence threshold of $\kappa=.89$, a spectral regularization parameter of $\lambda_v=.4$ and a Lagrange multiplier for the horizontal of $\lambda_h=190$. This image is the current best result, obtained by processing remote reference impedance estimates using the APTI spectral regularization technique, followed by a modified Bostick inversion. A true resistivity image corresponding to the complex resistivity images shown here will be given in Figure 52 at the end of this section.

The results in Figures 38-39 were obtained by choosing an acceptable operating point $(\kappa, \lambda_v, \lambda_h)$ subjectively, not by having objectively arrived at this choice as a result of some initial optimization, or by having had taken advantage of some prior constraints resulting from some trustworthy prior knowledge. Nevertheless, having chosen $\kappa, \lambda_v, \lambda_h$ by whatever means, we may then discuss an optimal solution ρ_c^* that minimizes the objective $J[\kappa, \lambda_v, \lambda_h](\rho_c)$, determined by these parameters.

Many inversion algorithms, including widely used magnetotelluric inversion methods, have similar subjectively chosen parameters. In this case, we are attempting to estimate a temporally constant state in which the forward observer has a nontrivial kernel that is also rendered uncertain due to noise. In such cases, the use of asymptotic methods is appropriate. There are many mathematical techniques available to address this important part of the problem, and examination of the alternatives is an important part of APTI's algorithm research. For the moment, we will focus on the more immediate aspect of the problem, namely the design and evaluation of objectives such as $\mathbf{J}[\kappa, \lambda_v, \lambda_h](\cdot)$, rather than the feedback aspect related to $\mathbf{J}(\rho_c)$.

Returning to Figure 38, we also observe a less pronounced anomaly beneath stations 2 and 3 to the left of the Golden Zone anomaly. It is important to understand that it is proper to refer to both as resistivity anomalies but we have yet to discuss their phase, which will determine whether they are more or less resistive than the background. Figure 39 shows the phase corresponding to the magnitude image of Figure 38. Here, we see that the two anomalies yield a phase response of opposite sign. For the case of a void, one expects that a good estimate of the complex resistivity ρ_c should have negative phase at frequencies corresponding to skin depths near its actual depth, while a conductive anomaly should have positive phase. This can be seen intuitively in two limiting cases.

In a homogeneous medium the skin depth is related to the wavelength according to $\lambda = 2\pi\delta$, so that wavelength and target depth can be related using the approximation

$$\frac{\lambda}{4} = \frac{\pi}{2}\delta = \frac{\pi\sqrt{2}}{4}2D \approx 2D,$$

where we have used the Bostick estimate of the target depth, $D = \delta/\sqrt{2}$. This means that a surface field excitation has a 90° phase lead over the surface response, if there is any, due to a target at depth D . In the case of a target satisfying the relatively deep

approximation, namely that its depth and diameter are in the relation $D \gg d$, the surface response for a TM mode excitation is almost entirely due to static charge collection at the target surface, and is well modeled as an equivalent two-dimensional dipole. In the case of a void, this charge collection leads to a secondary electric field that is in-phase with the primary electric field at depth. As a result, the secondary electric field at the surface lags the primary magnetic field in phase by 45° and therefore produces a ρ_c that can be approximated as

$$\rho_c \approx \frac{1}{\mu_0 \omega} \left[\frac{1}{j} \left(\frac{E_0 + E_s}{H_0} \right)^2 \right] = \frac{1}{\mu_0 \omega} (|Z_0| - j|Z_s|)^2$$

so that its phase satisfies

$$\tan \angle \rho_c \approx \frac{-2|Z_0||Z_s|}{|Z_0|^2 - |Z_s|^2},$$

from which it follows that $\tan \angle \rho_c < 0$ and in the limit of small response we have

$$\tan \angle \rho_c \approx -2 \left| \frac{E_s}{E_0} \right|.$$

In other words, the complex resistivity will exhibit at most a 90° phase lag, similar to a capacitor connected in parallel, as a result of the in-phase charge collection on the void. In the case of a conductive body, the secondary electric field is 180° out-of-phase with the primary at the surface of the target and this results in

$$\rho_c \approx \frac{1}{\mu_0 \omega} \left[\frac{1}{j} \left(\frac{E_0 - E_s}{H_0} \right)^2 \right] = \frac{1}{\mu_0 \omega} (|Z_0| + j|Z_s|)^2,$$

so that the complex resistivity will exhibit an inductive phase lead of at most 90° . Of course, the above analysis employs a single lumped circuit argument that only grossly approximates what is in truth a three-dimensional ground. For completeness, we mention that a similar lumped circuit analysis can be applied when the target satisfies a relatively shallow approximation. Under this assumption, two-layer half space models apply — relatively shallow voids and conductors corresponding to more conductive and less conductive top layers, respectively — and can be used to show that the same phase characteristics are obtained.

In general, the lead or lag characteristics of the complex resistivity response due to the extremes of conductive targets or resistive voids can be expected to be less than the $\pm 90^\circ$ phase differences of ideal circuit elements. Nevertheless, significant and consistent departures of the phase of the complex resistivity away from zero indicate the conductive or resistive nature (relative to the background) of anomalies that are observed.

Returning to Figure 38, we see that the resistivity anomaly on the right, which correlates well with the known horizontal position and depth of the Golden Zone tunnel, exhibits a negative phase anomaly as seen in Figure 39. This is consistent, in light of the above analysis, with the presence of a void. On the other hand, Figure 39 appears to indicate that the anomaly to the left, beneath stations 2 and 3, is conductive in nature.

We turn next to the examination of the effect of changing the minimum coherence threshold κ , as discussed in Section 2.2.3, for fixed values of λ_v and λ_h . A statistic that is useful when adjusting the coherence threshold is the percentage of the input data that exceed the threshold. As a first example, the coherence threshold of $\kappa=.89$ that was used in computing Figure 38 resulted in 2.54% of the input data having a coherence greater than .89; as a shorthand we will write this as $\%(.89)=2.54$. Figures 40 through 44 give the

results of increasing κ while keeping the other parameters fixed at $\lambda_v = .4$ and $\lambda_h = 190$, as were used in the first two figures. For brevity, we will show only the magnitude images, although complete interpretation of the data would require the phase as well.

Figure 40 is important in that it has its minimum coherence threshold set to zero, so that $\%(0)=100$; in other words, all the input data at every frequency was included in the inversion. Although remote reference processing was employed, so that the input impedance estimates were unbiased, the peaks that can be seen in the resistivity image appear to be too high in magnitude, whether they are due to an underlying ground anomaly or not. This suggests some future attention be paid to robust remote reference impedance estimation.

Figures 41 through 44 present the remainder of the parameter scan through the five values of $\kappa = 80, 85, 87$, and 95 , respectively, which may be compared to the other figures; the associated percentages here are given by $\%(85)=3.9$, $\%(87)=3.0$, $\%(95)=1.8$. We observe that the anomaly associated with the tunnel is obscured by the inclusion of the relatively noisy data that passes the lower coherence thresholds, but appears strongly when a high threshold is set. This effect is due to the abrupt nature of the thresholding process.

It should be mentioned that many MT inversion algorithms that employ remote reference processing use no κ thresholding, since the cross-spectra from remote reference processing are unbiased estimates of the true spectra regardless of the coherence. However, the coherence is a measure of the degree to which the measured data are consistent with a distant plane wave, and so the coherence may be used with remote reference data as an indication of the quality of the data.

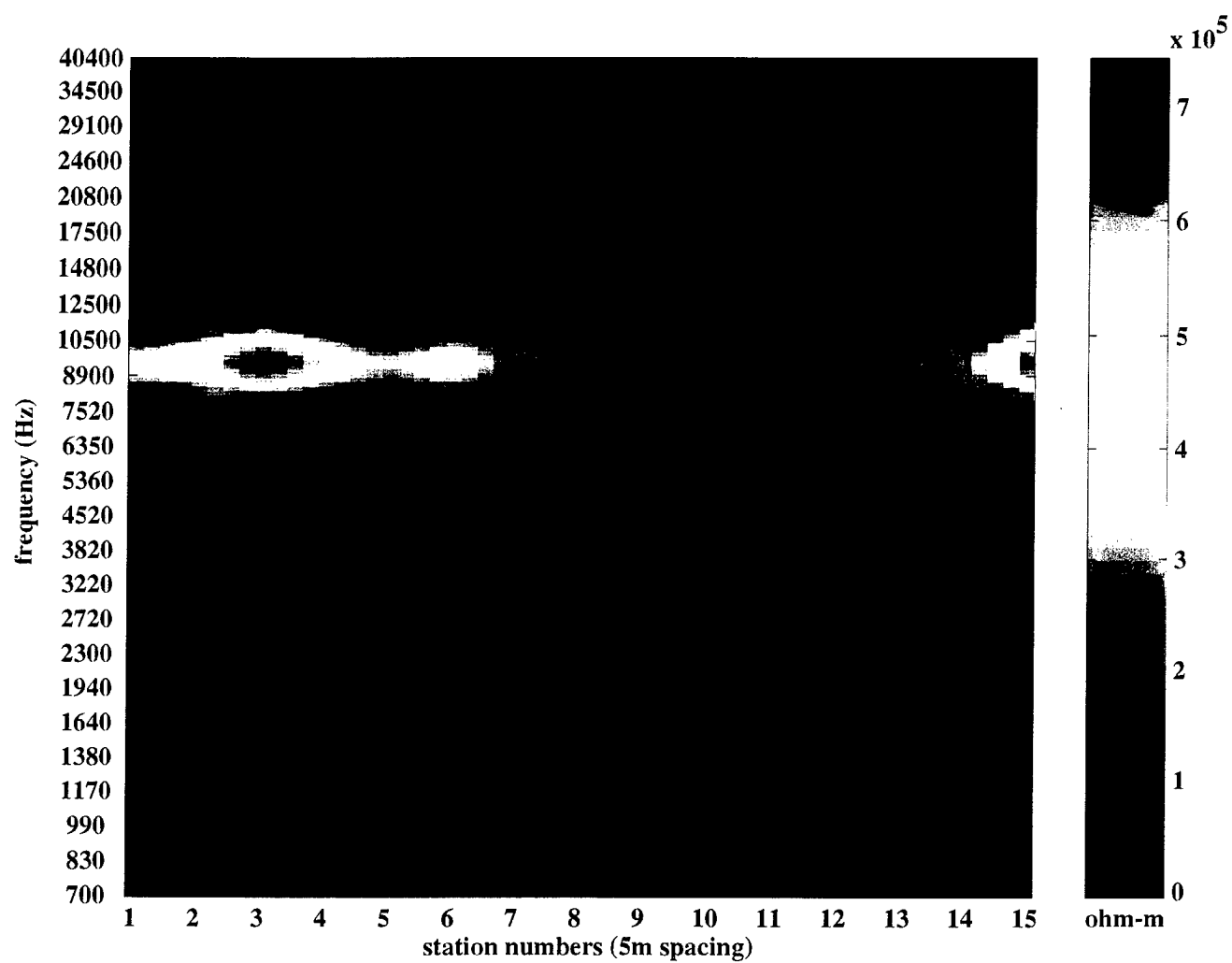


Figure 40. Complex Resistivity Magnitude Image using
Parameters $\kappa = 0$, $\lambda_v = .4$, $\lambda_h = 190$; $\%(0) = 100$.

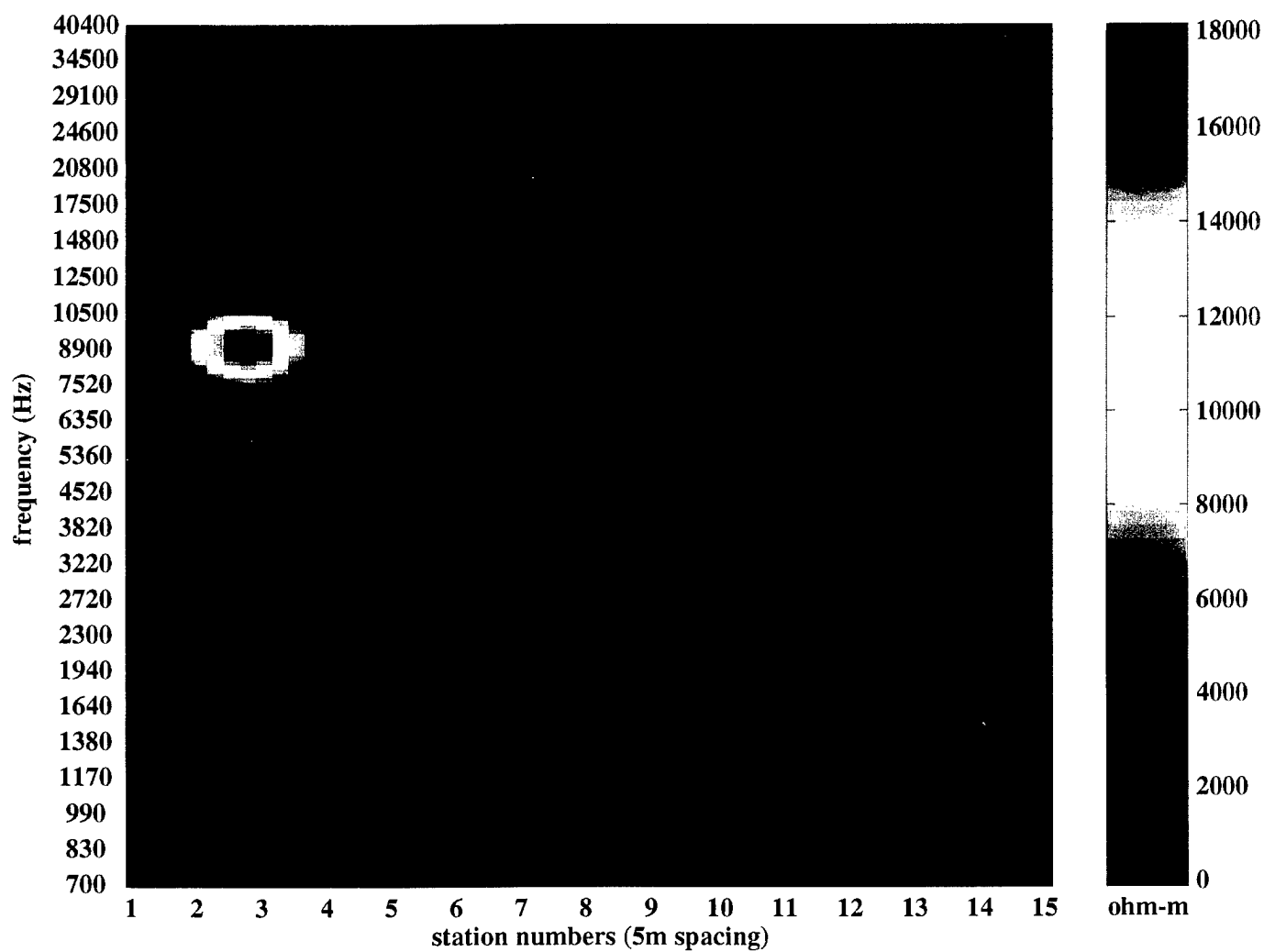


Figure 41. Complex Resistivity Magnitude Image using
Parameters $\kappa = .80$, $\lambda_v = .4$, $\lambda_h = 190$; $\%(80) = 8.2$.

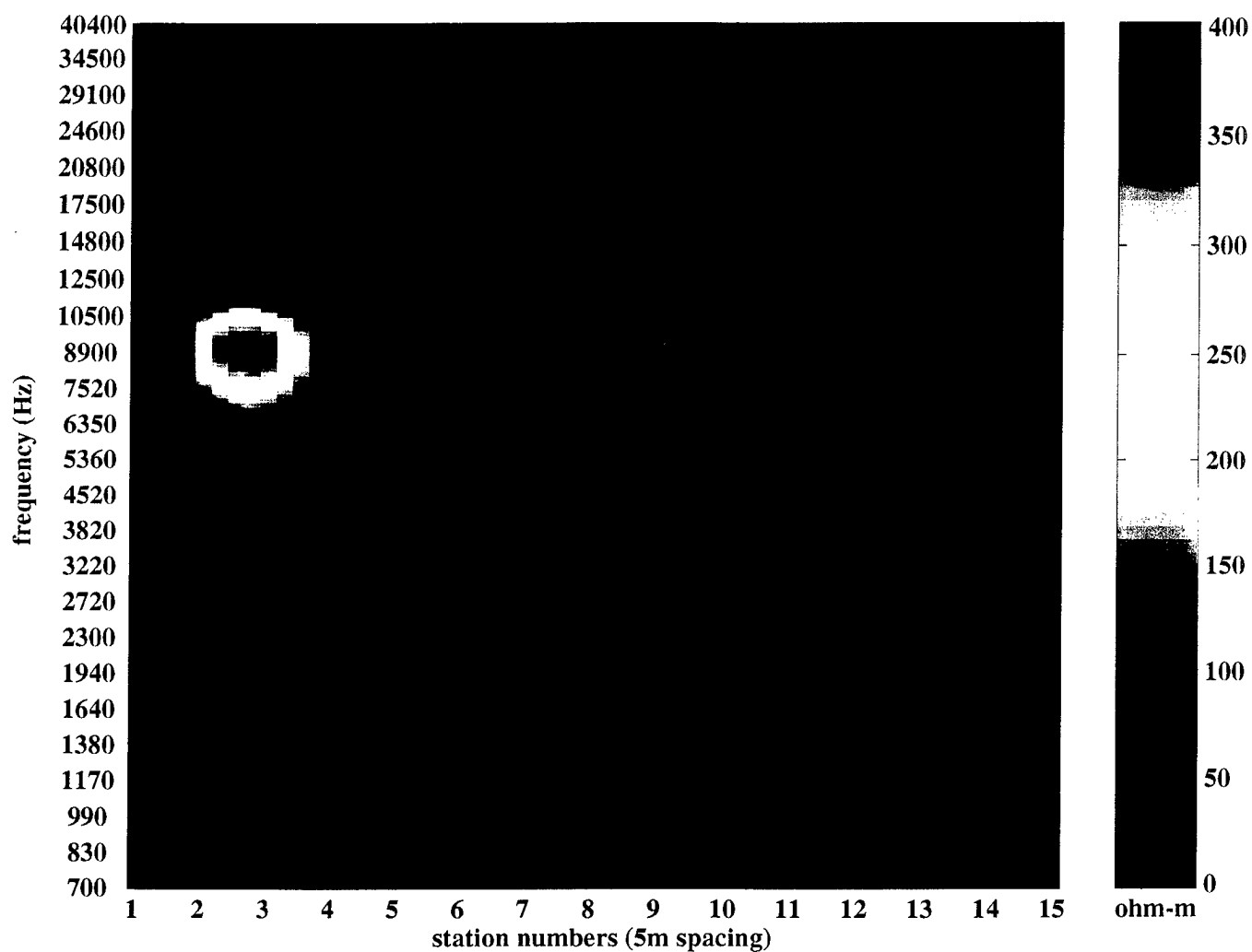


Figure 42. Complex Resistivity Magnitude Image using
Parameters $\kappa = .85$, $\lambda_v = .4$, $\lambda_h = 190$; $\%(85) = 3.96$.

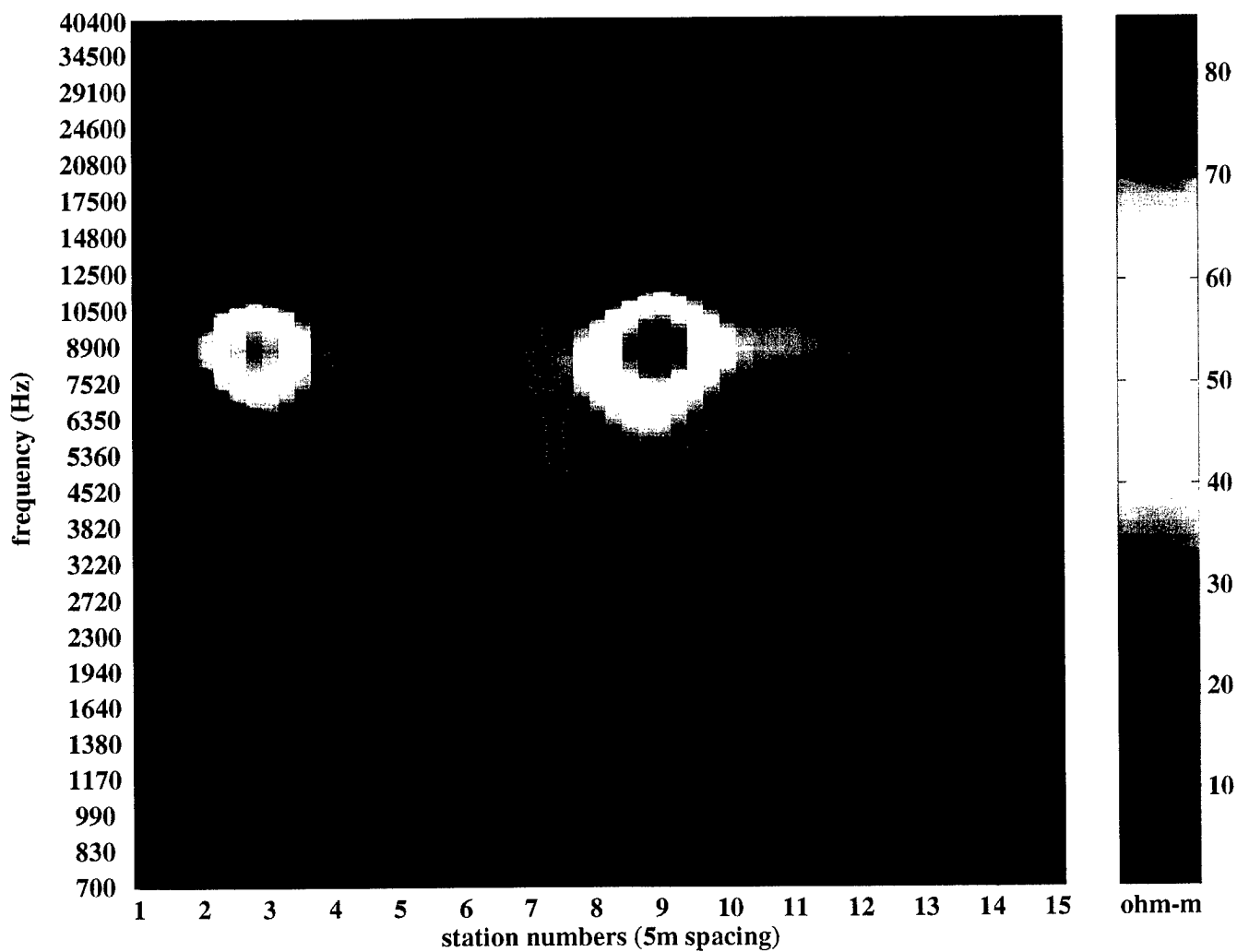


Figure 43. Complex Resistivity Magnitude Image using
Parameters $\kappa = .87$, $\lambda_v = .4$, $\lambda_h = 190$; $\%(87) = 3.01$.

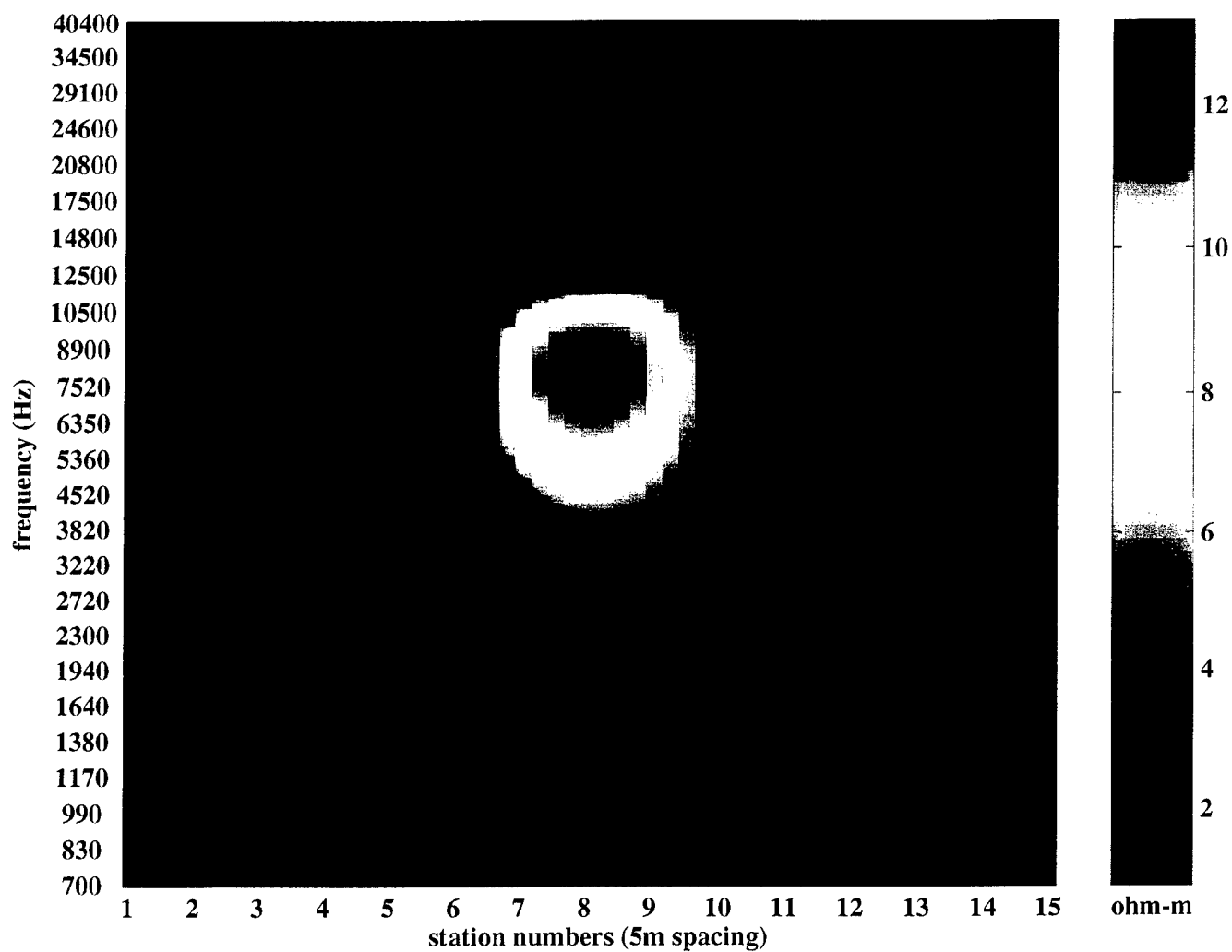


Figure 44. Complex Resistivity Magnitude Image using
Parameters $\kappa = .95$, $\lambda_v = .4$, $\lambda_h = 190$; $\%(95) = 1.80$.

We have seen that the abrupt inclusion or exclusion of data by coherence thresholding makes the images very sensitive to the value of κ . Ideally, a continuous weighting would be employed to reduce the effects of poor quality data without excluding it entirely. This would reduce the sensitivity of the image to settings of the weighting parameter. We have employed the coherence here as an easily computed indicator of data quality, but it is also possible to derive more accurate quality estimates using the electric and magnetic field signal-to-noise ratios that can be computed using a remote reference. Implementation of this enhancement to the processing procedure is planned for the next year.

An additional effect of changes in the threshold is that the average conductivity decreases as the κ threshold increases. This is because as the percentage of points that are used in the inversion falls, more weight is implicitly given to the prior constraint.

Directly modifying λ_v results in a similar bias. In this sense, the complex resistivity images shown are more properly considered as indicators of significant departures from a one-dimensional stratified earth (that is, indicators of the presence of two- and three-dimensional objects), rather than estimates of the background resistivity. Conversion of the complex resistivity to an accurate background resistivity estimate and production of a depth estimate consistent with that resistivity is the final step in producing an image, as will be described at the end of this section.

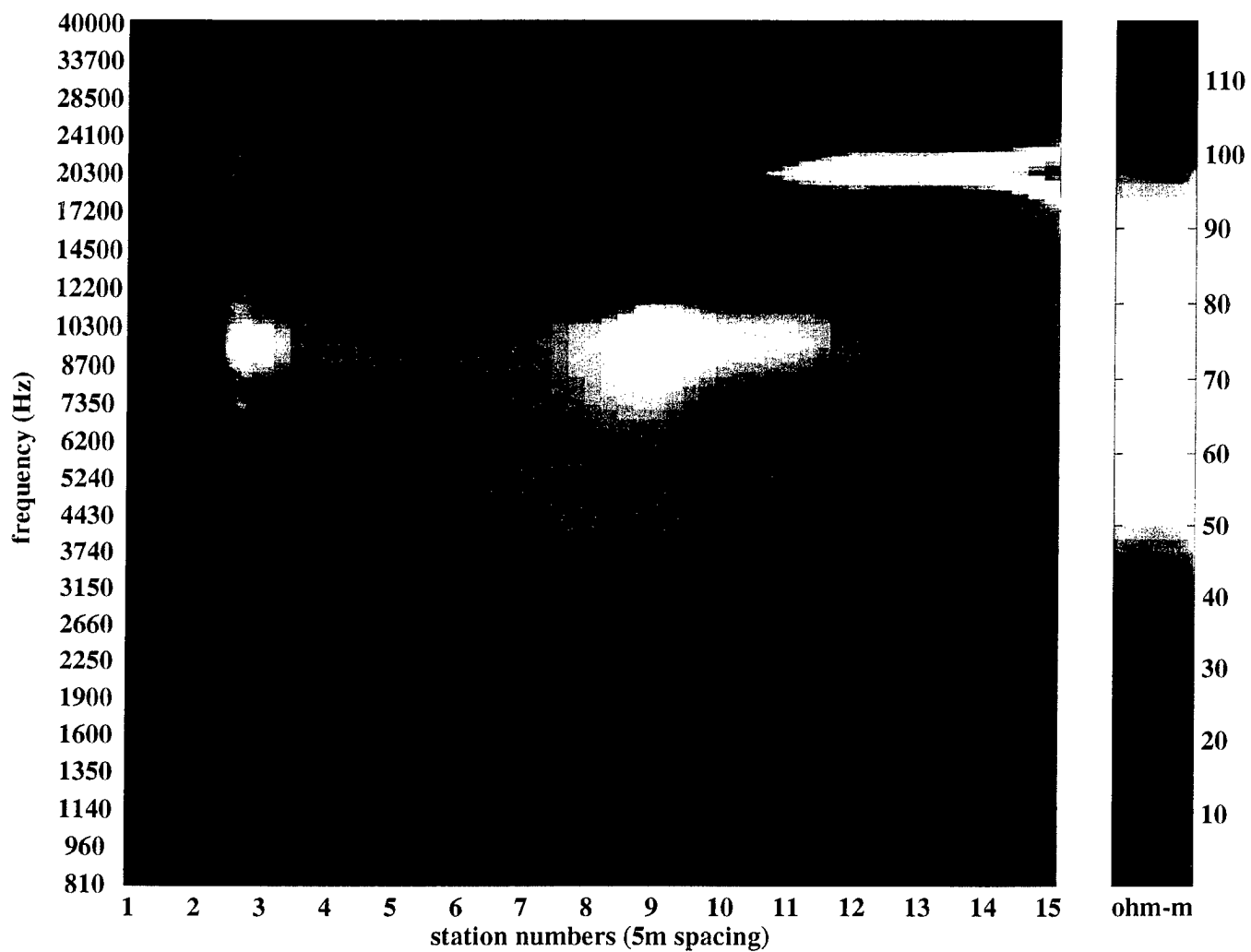


Figure 45. Complex Resistivity Magnitude Image using
Parameters $\kappa = .89$, $\lambda_v = .05$, $\lambda_h = 190$.

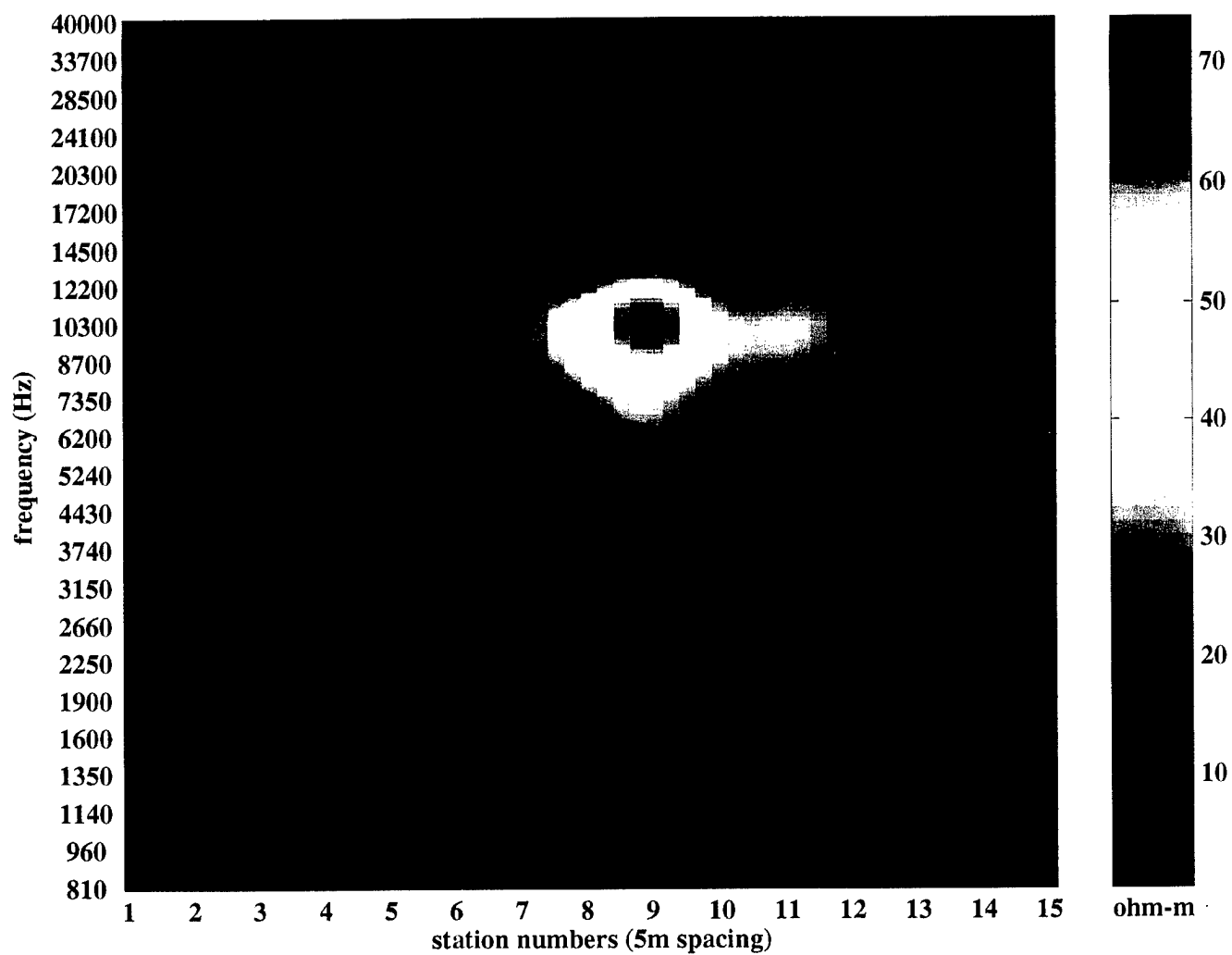


Figure 46. Complex Resistivity Magnitude Image using
Parameters $\kappa = .89$, $\lambda_v = .20$, $\lambda_h = 190$.

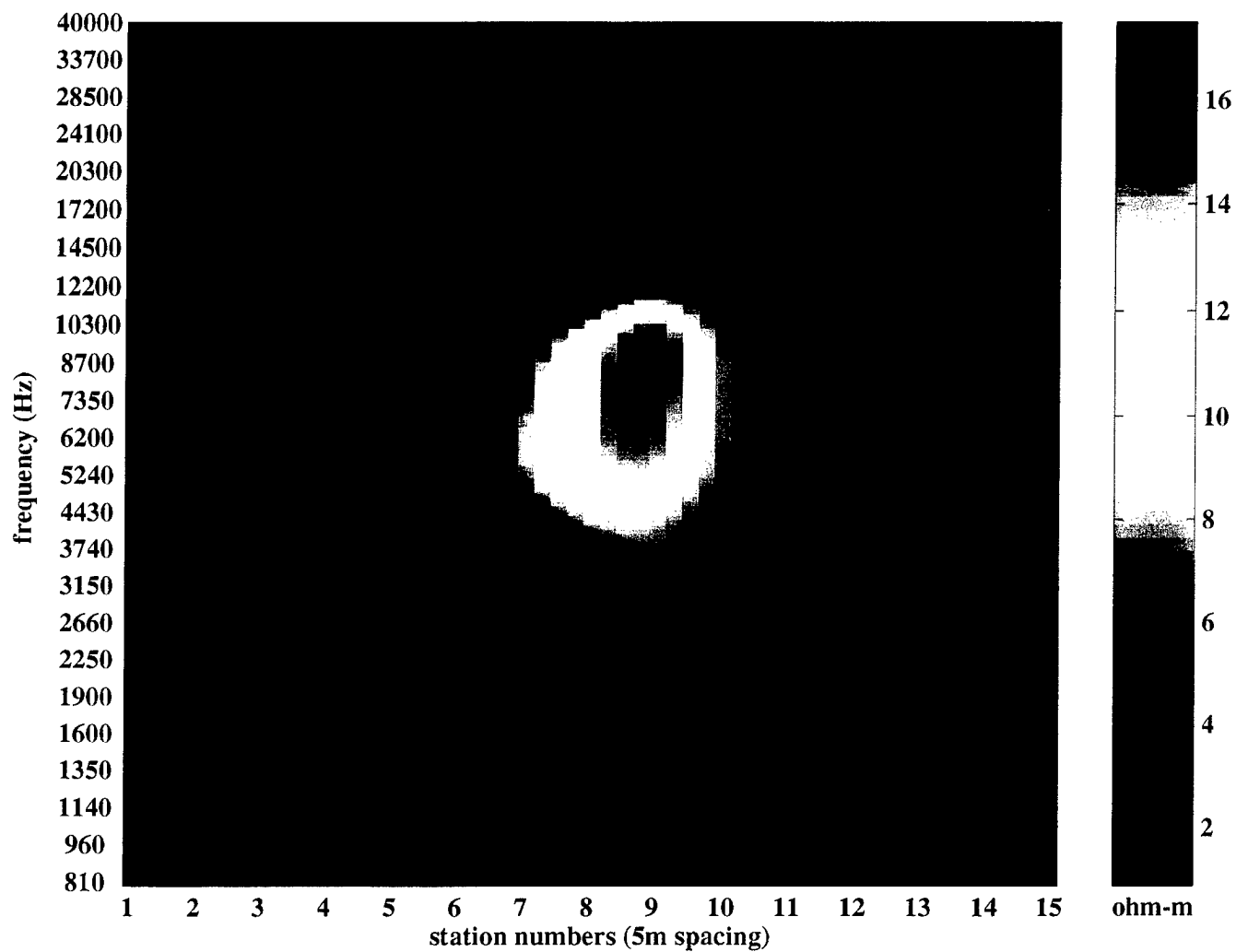


Figure 47. Complex Resistivity Magnitude Image using
Parameters $\kappa = .89$, $\lambda_v = .80$, $\lambda_h = 190$.

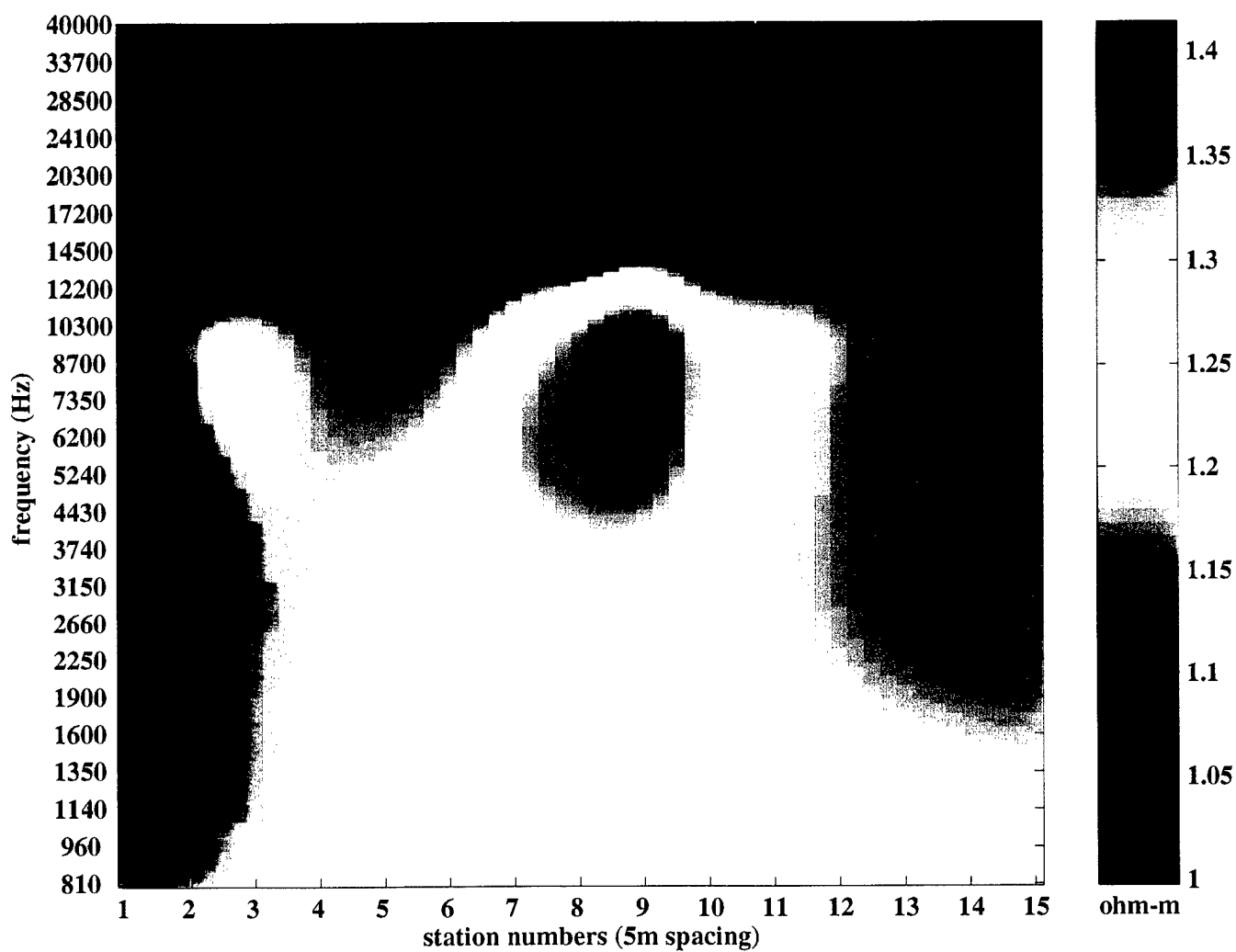


Figure 48. Complex Resistivity Magnitude Image using
Parameters $\kappa = .89$, $\lambda_v = 6.4$, $\lambda_h = 190$.

Next we turn to examination of $\rho_c^*(.89, \lambda_v, 190)$ as λ_v is varied. Figures 45 - 48 give the magnitude and phase images for the values $\lambda_v=.05, 0.2, 0.8$ and 6.4 . We see that as λ_v increases in value, the estimate displays less resolution in the vertical direction, which is a reflection of the fact that the $\mathbf{J}_v[\kappa, \lambda_v](\rho_c)$ objective determines an equivalent vertical filter width that becomes broader at a given frequency as λ_v increases. On the other hand, if λ_v is set too small (compare $\lambda_v=.05$ and 0.2), then there may be insufficient support for the vertical filter at a given frequency to achieve constructive superposition.

Figures 49 through 51 show $\rho_c^*(.89, .4, \lambda_h)$ as λ_h is varied to $\lambda_h=120, 220$ and 320 . The effect of this straightforward adaptation of the Bostick inverse is easy to appreciate, in that it simply leads to a loss of horizontal resolution as λ_h is raised, and for a fixed λ_h , a resolution loss that increases with depth.

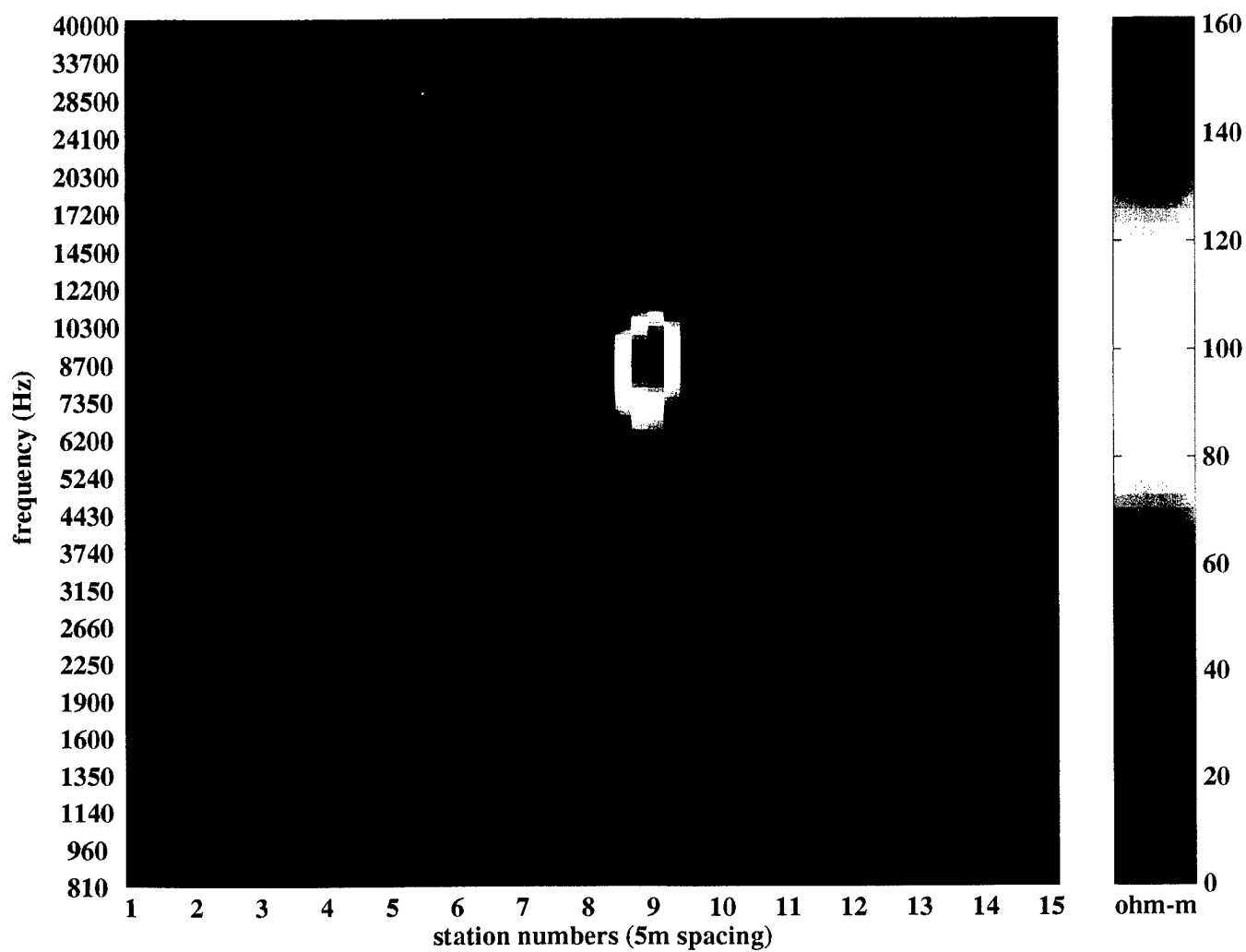


Figure 49. Complex Resistivity Magnitude Image using
Parameters $\kappa = .89$, $\lambda_v = .4$, $\lambda_h = 120$.

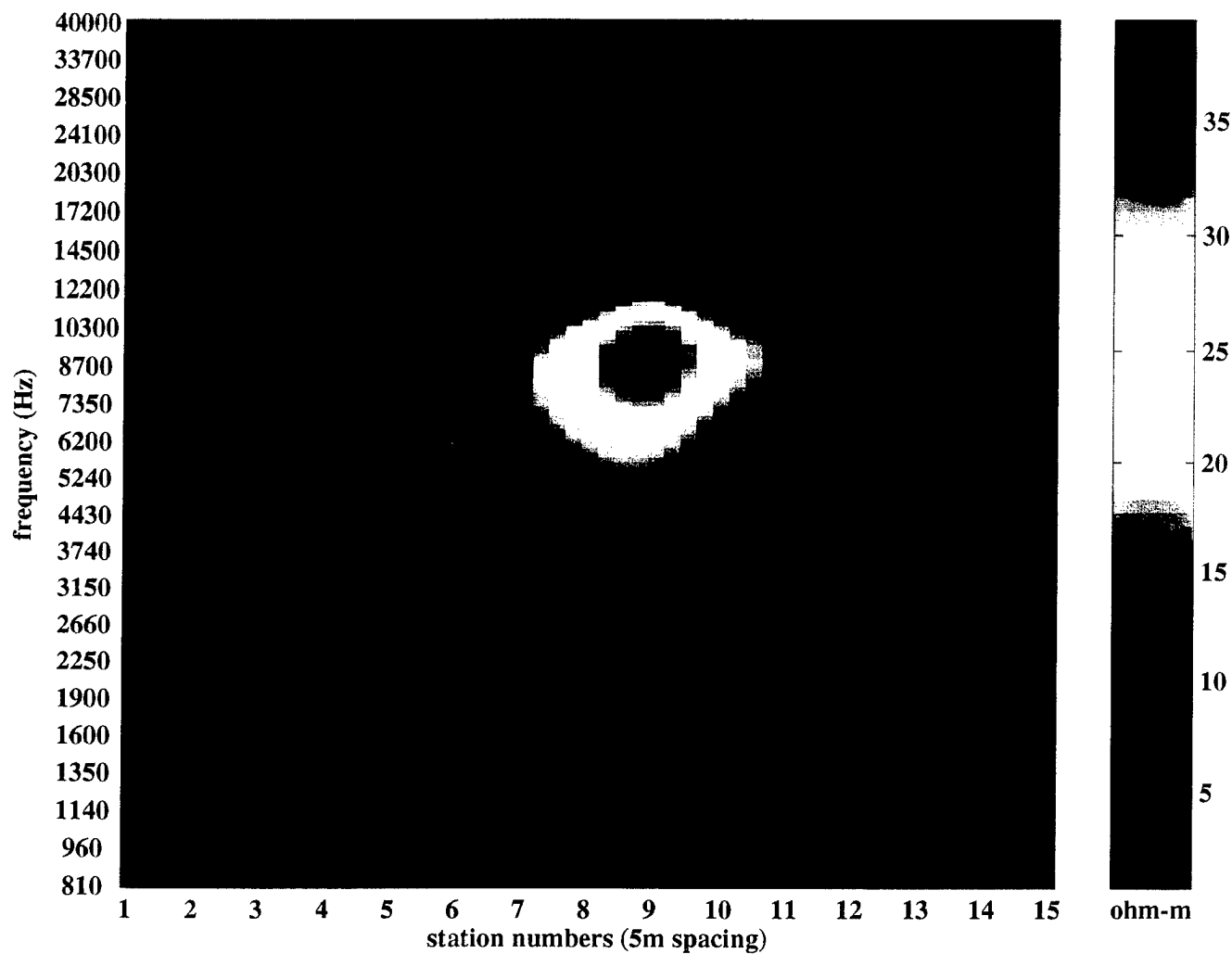


Figure 50. Complex Resistivity Magnitude Image using
Parameters $\kappa = .89$, $\lambda_v = .4$, $\lambda_h = 220$.

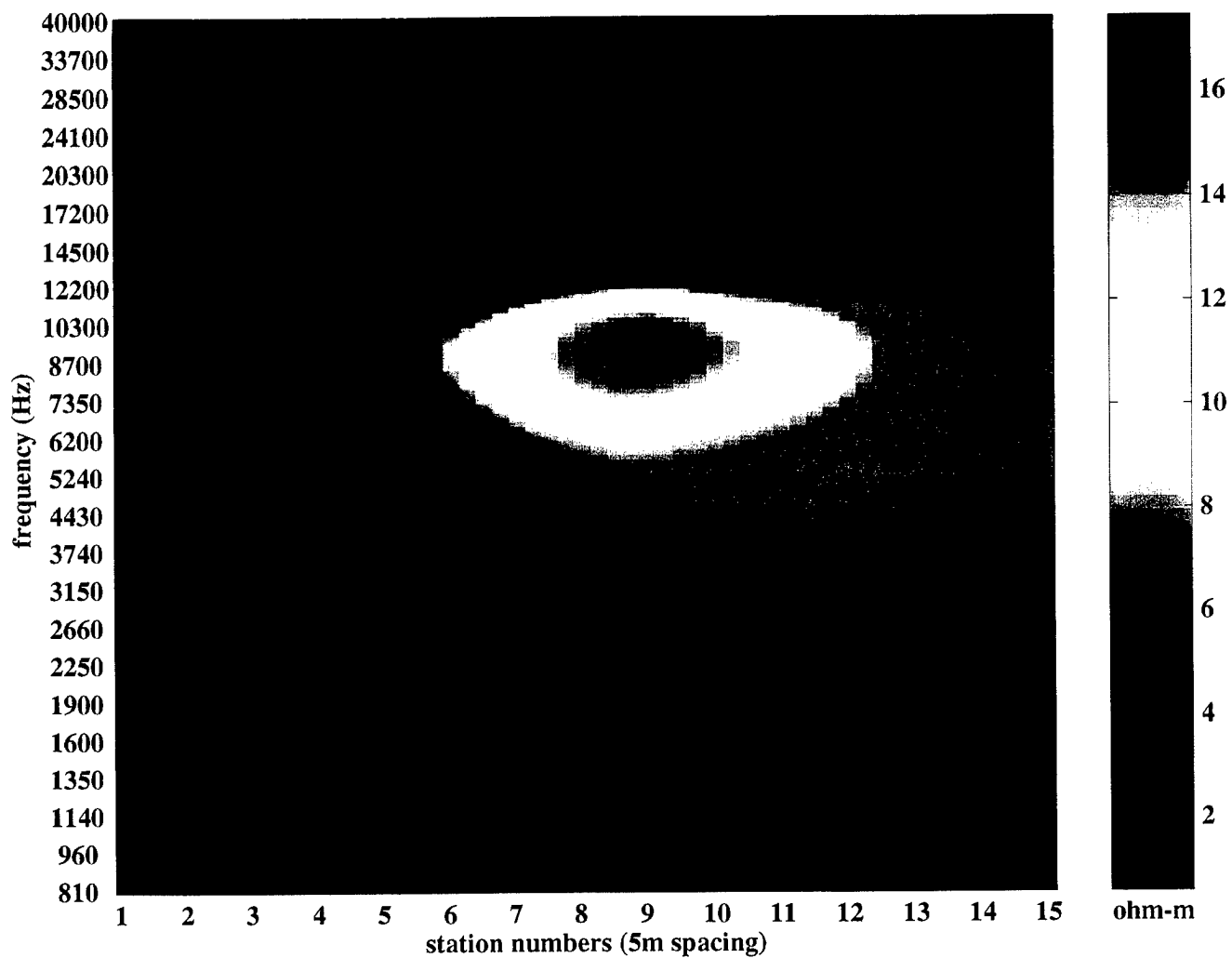


Figure 51. Complex Resistivity Magnitude Image using
Parameters $\kappa = .89$, $\lambda_v = .4$, $\lambda_h = 320$.

4.3.3. Final Resistivity Image

We next turn the discussion to the estimation of a real-valued resistivity image, as opposed to the complex resistivity images that has been the focus until now. As we have outlined earlier, the TM response of a two-dimensional void satisfying the relatively deep approximation, $D \gg d$, is well modeled as an equivalent quasi-static dipole in-phase with the current excitation at depth. For this case, in the limit defining the electrically shallow approximation, *i.e.*, $D \ll \delta(f)$, we see that the current due to the equivalent dipole response at the surface will be in-phase with the surface current due to the primary field. In this case, a void will result in a distinct rise in the magnitude of the complex resistivity while a metallic cylinder will result in its decrease, as one might expect.

However, in the discussion above, we have shown that the well known Bostick apparent depth criterion, which is valid for a half-space, defines a frequency at which the quarter wavelength approximates the round-trip distance to the target. At this frequency, for which we have only $D \sim \delta(f)$, the equivalent quasi-static dipole will yield a surface complex resistivity that has an increase in magnitude for either a resistive void or a conductive cylinder. The two cases will, however, have opposite complex resistivity phase responses.

From the complex resistivity magnitude and phase, we can compute a final output image that includes the information from both quantities and constitutes our best estimate of the actual (non-complex) subsurface resistivity. In addition, we can compute depth estimates for the frequencies at which these real resistivities are computed, resulting in an image showing the estimated subsurface resistivity as a function of depth. This image is shown in Figure 52.

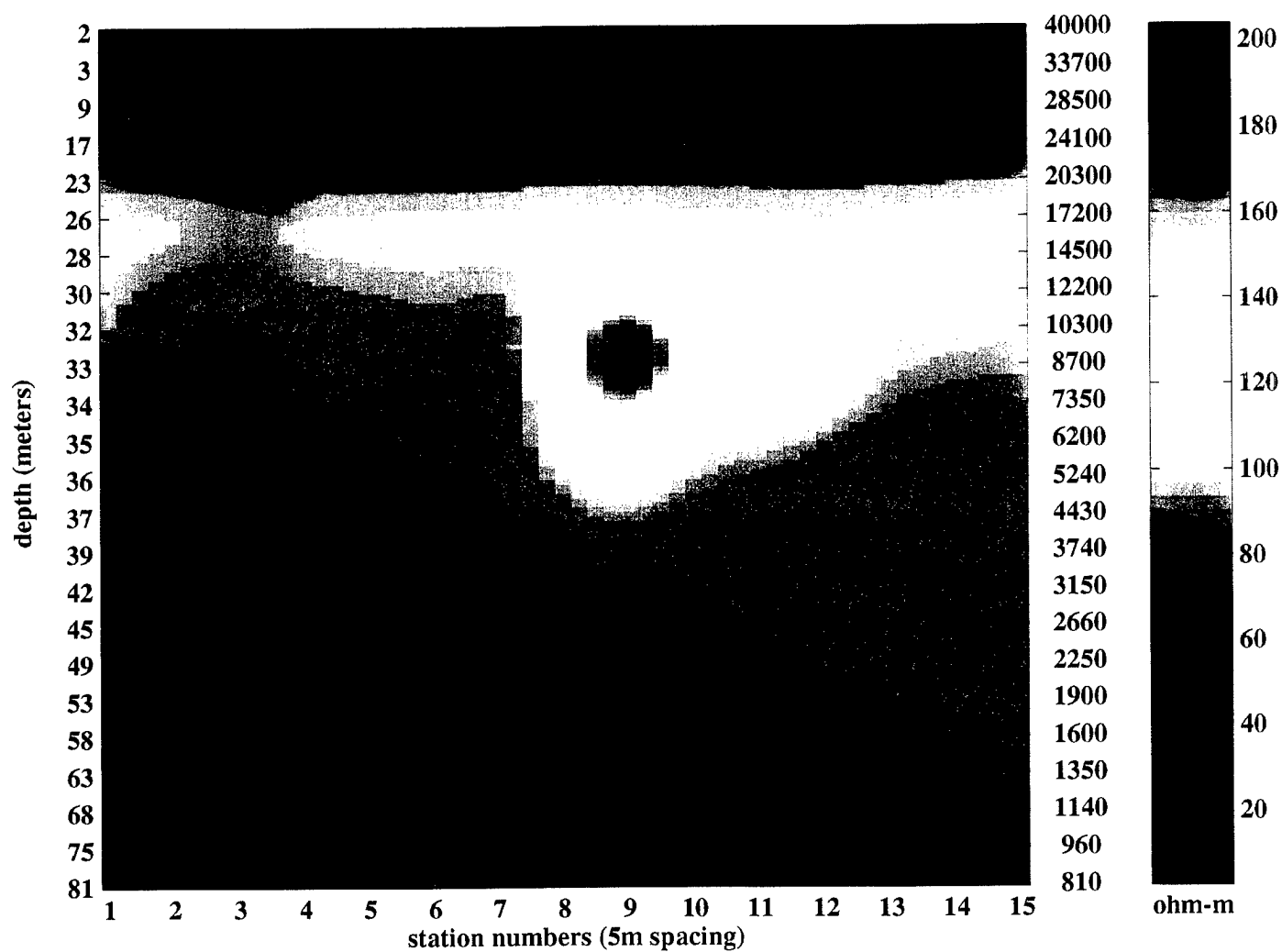


Figure 52. Final Resistivity Image of Golden Zone
Line 1 Data.

The resistivity estimate in Figure 52 is derived from the complex resistivity in the following manner. As discussed above, imaging in the TM case involves a perturbation solution for the problem, involving relatively deep loci of quasi-static charge. This perturbation solution may be easily recast in terms of a positive, real-valued resistivity if we superpose the magnitude and phase anomalies in the complex resistivity ρ_c using the expression

$$\rho_{final} = \left(1 + \frac{|\rho_c|}{\langle |\rho_c| \rangle} \sin \angle \rho_c \right) \cdot |\rho_b|,$$

where ρ_b is an estimate of the background resistivity obtained, for example, using classic, low-resolution resistivity estimation techniques.

The final image is consistent with most known information on the characteristics of the subsurface at survey line 1. A partially resolved surface conducting layer is present, as is common, although it is not clear that the surface layer at survey line 1 extended to the 15 meter depth shown. The site had been terraced by earthmoving equipment, so it is possible that the disturbed layer extended to this depth. It is more likely, however, that the conducting layer is not completely resolved, and that a thinner layer of higher conductivity has been imaged as a thick layer because the frequency data above 50 kHz needed to resolve the thin layer is not present in the input.

The location and depth of the resistive anomaly shown beneath stations 8 and 9 are consistent with the known location of the tunnel. The horizontal location of the anomaly matches the tunnel location to within 2-3 meters, approximately the limit of horizontal accuracy for a station spacing of 5 meters. The estimated depth of 34 meters is larger than the known tunnel depth of 29 meters. Accurate estimation of depths when a partially resolved surface layer is present is very difficult, and errors of 20 percent are not unexpected. (A more complete discussion of the depth estimation procedure is given below.)

The conductive anomaly seen beneath stations 2 and 3 is of unknown origin. It appears at approximately the same depth as the resistive anomaly believed to be caused by the tunnel, and is of relatively small size. This suggests that it might be due to a man-made object, but it is unknown whether tunneling occurred at this level before the current 325 foot level tunnel was constructed in 1983.

The background resistivity estimated for the region beneath survey line 1 is 80-100 Ohm-meters. Although there are no measurements of this exact location for comparison, this is somewhat lower than the 200-300 Ohm-meters computed for the general area from earlier airborne loop-loop survey measurements at 9 kHz. Since both the airborne survey and this experiment measured resistivities in approximately the same depth range, better agreement between the two estimates would have been expected. The resolution of the airborne survey data were rather coarse, however, and it is difficult to determine whether local variations in conductivity that were not resolved by the airborne data are sufficiently large to account for this difference. Processing of the data from survey lines 2 and 3 should provide some additional information to address this question.

4.3.4. Depth Estimation

We will now describe the depth estimation procedure for the final resistivity image in more detail. It should be mentioned that depth estimation is often treated as a decoupled problem, *i.e.*, given a resistivity estimate, employ it directly to estimate the depth. In the general case, the two should be estimated simultaneously. This is especially true since, given its nature, one knows a priori that any depth estimate should be monotonic.

Direct employment of this constraint, even in a decoupled approach, is somewhat difficult since its description leads to nonlinearities in the design of a constraint objective. In general, the coupled depth-resistivity problem deserves and requires more attention, however, at present we employ a simplified approach that can be trusted, and has been

shown, to provide reasonable estimates in relatively simple geologies. As a compromise, our approach addresses the monotonicity aspect of the depth estimate in a manner that is coupled with a resistivity estimate, but avoids nonlinearities.

Put simply, the depth averaging algorithm begins by taking the average of the remote reference impedance at all measured frequencies using a very low coherence threshold. We used $\kappa=.1$ and in addition deleted all data for which the frequencies displayed near-field effects. This impedance average was then processed using the well-known Cagniard method which produces a stable resistivity estimate when the ground is close to one-dimensional. To address possible errors in the estimate due to this one-dimensional assumption, the Cagniard output is next processed to obtain a marginal using a classical median filter at each frequency. This one-dimensional marginal delivers what may be considered a “background” resistivity for the region in question.

Next, the resistivity marginal is subjected to an iterative smoothing process to enforce the monotonicity constraint. As an initial condition, the resistivity marginal is used to obtain a point-wise estimate of the skin depth using the Cagniard method. This initial estimate is not in general monotonic. Then, the resistivity marginal is successively filtered using a low-pass FIR filter having a relatively wide bandwidth, until the skin depth computed using the Cagniard method satisfies a monotonicity constraint to within a desired tolerance. The skin depth estimate which results is used to assign depths to the resistivities estimated above, resulting in the depth scale shown in the final image.

5. Conclusions and Future Plans

The results described in the preceding sections include several important accomplishments, including design and integration of the hardware and software needed for collecting field data, detailed electromagnetic simulations that confirm several important effects seen in experimental data, and a successful field experiment that resulted in imaging of the Golden Zone mine tunnel. Major areas of emphasis for the next year of this effort include:

(1) Elimination of the backlog of unprocessed experimental data. This backlog results from both the data transfer difficulties described in Section 4.1.2.5, and from the lack of a packaged inversion algorithm that could produce images without input from an operator. Both of these problems are in the process of being resolved, and it is expected that the backlog will be eliminated within the next three months.

(2) Improvement of the speed with which new data are processed. The same modifications implemented to remove the backlog of unprocessed data will also allow much faster processing of new data, so that the results of experiments are available within weeks after the completion of the experiment.

(3) More extensive use of simulation to study imaging performance. Current simulations are not exact replacements for experimental data, principally because they contain far fewer frequencies: typical simulations have data at tens or hundreds of frequencies, rather than the thousands in an experimental data set. Production of simulated data sets that match actual experiments in frequency resolution will allow simulated data to substitute for experimental results in imaging studies.

(4) Completion of detailed comparisons between simulated data and experimental data, and between APTI's inversion algorithm and conventional magnetotelluric algorithms. The availability of high frequency resolution simulations will also make these comparisons possible, allowing us to verify conclusions drawn from experimental data and examine the improvements in imaging performance possible using APTI's imaging techniques.

(5) Conduct field experiments on a wider variety of targets, including conductive targets. The experiments conducted to date have concentrated on simple two-dimensional resistive tunnels. Many other types of structures are also of military interest, and the other simple two-dimensional target, a conductive object, will also be examined in experiments and computations. Since the field perturbations at the surface due to this type of target are larger than those due to a resistive object, it is expected that better performance can be achieved on conductive targets.